

ผลเฉลยทางโพโรอิลาสติกสำหรับหลุมเจาะและทรงกระบอก



นาย วิชัยรัตน์ แก้วเจือ

ศูนย์วิทยทรัพยากร
จุฬาลงกรณ์มหาวิทยาลัย

วิทยานิพนธ์นี้เป็นส่วนหนึ่งของการศึกษาตามหลักสูตรปริญญาวิศวกรรมศาสตรดุษฎีบัณฑิต

สาขาวิชาวิศวกรรมโยธา ภาควิชาวิศวกรรมโยธา

คณะวิศวกรรมศาสตร์ จุฬาลงกรณ์มหาวิทยาลัย

ปีการศึกษา 2553

ลิขสิทธิ์ของจุฬาลงกรณ์มหาวิทยาลัย

POROELASTIC SOLUTIONS FOR BOREHOLE AND CYLINDER



Mr. Wichairat Kaewjuea

ศูนย์วิทยทรัพยากร
จุฬาลงกรณ์มหาวิทยาลัย

A Dissertation Submitted in Partial Fulfillment of the Requirements
for the Degree of Doctor of Philosophy Program in Civil Engineering

Departmental of Civil Engineering

Faculty of Engineering

Chulalongkorn University

Academic Year 2010

Copyright of Chulalongkorn University

วิทยุรัตน์ แก้วเจือ : ผลเฉลยทางโพโรอิลาสติกสำหรับหลุมเจาะและทรงกระบอก.
(POROELASTIC SOLUTIONS FOR BOREHOLE AND CYLINDER) อ. ที่ปรึกษา
วิทยานิพนธ์: ศ.ดร.ธีรพงศ์ เสนจันทร์ไพไชย, 85 หน้า

วิทยานิพนธ์ฉบับนี้นำเสนอผลตอบสนองทางโพโรอิลาสติกของทรงกระบอก และหลุมเจาะภายใต้แรงกระทำสมมาตรรอบแกน สำหรับปัญหาหลุมเจาะได้มีการพิจารณาผลกระทบจากบริเวณที่ถูกรบกวนรอบหลุมเจาะเนื่องจากการขุด ทำให้ค่าโมดูลัสของแรงเฉือนและค่าการซึมผ่านได้ของน้ำเปลี่ยนแปลงไปจากเดิมซึ่งยังไม่เคยมีการนำเสนอในการศึกษาในอดีต ในการศึกษานี้ได้พิจารณาปัญหาสามเรื่อง ได้แก่ ผลตอบสนองแบบกึ่งสถิตของทรงกระบอกและหลุมเจาะ และผลตอบสนองทางพลวัตของหลุมเจาะ ผลเฉลยทั่วไปที่นำเสนอในวิทยานิพนธ์ฉบับนี้สามารถนำไปใช้ประโยชน์ได้หลายด้านเช่นในการสร้างแบบจำลองทางทฤษฎีของการทดสอบในห้องปฏิบัติการและการทดสอบในสนามสำหรับงานด้านวิศวกรรมโยธา การวิเคราะห์ปัญหาในการศึกษาน้ำอภัยทฤษฎีทางโพโรอิลาสติกของ Biot และระเบียบวิธีการแปลงปริพันธ์ ผลเฉลยทั่วไปได้จากการแก้สมการของ Biot โดยใช้วิธีการแปลงลาปลาซเทียบกับเวลาสำหรับปัญหาที่กึ่งสถิตและการแปลงฟูเรียร์เทียบกับแกนแนวตั้งสำหรับปัญหาหลุมเจาะ ผลเฉลยในโดเมนเวลาถูกคำนวณโดยใช้ระเบียบวิธีเชิงตัวเลขสำหรับการผกผันลาปลาซและการผกผันฟูเรียร์ การตรวจสอบความถูกต้องของผลเฉลยได้รับการยืนยันโดยการเปรียบเทียบกับคำตอบจากงานวิจัยในอดีต การวิเคราะห์ปัญหาขอบเขตของทรงกระบอกและหลุมเจาะที่นำเสนอแสดงให้เห็นถึงประโยชน์ของผลเฉลยทั่วไปที่ได้จากวิทยานิพนธ์ฉบับนี้สำหรับการประยุกต์ใช้กับปัญหาด้านวิศวกรรมโยธา นอกจากนี้ยังได้แสดงถึงอิทธิพลของตัวแปรต่างๆต่อผลตอบสนองทางโพโรอิลาสติกของทรงกระบอก และหลุมเจาะ

ศูนย์วิทยุทรัพยากร
จุฬาลงกรณ์มหาวิทยาลัย

ภาควิชา.....วิศวกรรมโยธา.....

สาขาวิชา.....วิศวกรรมโยธา.....

ปีการศึกษา..... 2553.....

ลายมือชื่อนิสิต..... .....

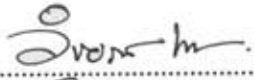
ลายมือชื่อ อ.ที่ปรึกษาวิทยานิพนธ์..... .....

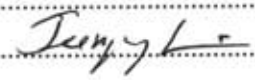
4871843221 : MAJOR CIVIL ENGINEERING

KEYWORDS: POROELASTICITY / STRESS ANALYSIS / CYLINDER / BOREHOLE / PORE PRESSURE / EXCAVATION DISTURBED ZONE / ROCK MECHANICS.

WICHAIRAT KAEWJUEA : POROELASTIC SOLUTIONS FOR BOREHOLE AND CYLINDER. THESIS ADVISOR : TEERAPONG SENJUNTICHAJ, Ph.D., 85 PP.

This dissertation presents a theoretical study of poromechanical responses of a finite cylinder, and an infinite borehole under axisymmetric loading. The disturbed zone due to borehole drilling process is taken into account in the analysis of borehole problems, in which shear modulus and permeability coefficient are changed from their original values. There are three problems presented in this study, i.e. quasi-static responses of a cylinder and a borehole, and dynamic response of a borehole. The solutions to these problems are useful for theoretical modeling of several laboratory and in-situ tests in civil engineering. A new set of analytical solutions to all problems are derived based on Biot's theory of poroelasticity by employing integral transform techniques. The general solutions to the coupled governing equations are obtained by applying the Laplace transform with respect to time for quasi-static problems, and applying the Fourier transform with respect to the vertical coordinate for the borehole problems. They are then numerically inverted by applying an accurate numerical scheme for the Laplace inversion, and applying an adaptive quadrature scheme for the Fourier inversion. Accuracy of numerical solutions is confirmed by comparing with independent existing solutions for the limiting cases. Several boundary-value problems are solved to demonstrate the applications of the general solutions to practical situations involving cylinders and boreholes. Selected numerical results are presented for displacements, stresses, pore pressure and fluid discharge to demonstrate the influence of poroelastic material properties and other governing parameters, and the salient features of the coupled poroelastic response.

Department : Civil Engineering Student's Signature : 

Field of Study : Civil Engineering Advisor's Signature : 

Academic Year : 2010

ACKNOWLEDGMENTS

This research work was supported by Commission on Higher Education (CHE) and Asean University Network/The Southeast Asia Engineering Education Development Network (AUN/SEED-Net), and the 90th Anniversary of Chulalongkorn University Fund (Ratchadaphiseksomphot Endowment Fund). Their supports are gratefully acknowledged.

The author wishes to express his sincere appreciation to his advisor, Professor Dr. Teerapong Senjuntichai for his kind guidance and long-term support throughout this work. He also wishes to express his gratitude to Professor Dr. Nimal Rajapakse at Simon Fraser University, Canada, for his kindness and invaluable advice on the research work and very warm welcome during the visits at University of British Columbia, CA in April 2008 – July 2009. Grateful acknowledgements are due to Professor Dr. Thaksin Thepchatri, Associate Professor Dr. Boonchai Ukritchon, Assistant Professor Dr. Jaron Rungamornrat and Assistant Professor Dr. Sasikorn Leungvichcharoen for their helpful comments and serving in the thesis committee.

Special thanks are also due to everyone who has helped directly and indirectly in the preparation of this thesis. Finally, the author would like to express his gratitude to his parents for their support and love.



ศูนย์วิทยทรัพยากร
จุฬาลงกรณ์มหาวิทยาลัย

CONTENTS

	Pages
Abstract (Thai).....	iv
Abstract (English).....	v
Acknowledgements.....	vi
Contents.....	vii
List of Figures.....	ix
List of Symbols.....	xii
Chapter I Introduction.....	1
1.1 General.....	1
1.2 Objectives and scopes of present study.....	2
Chapter II Literature Reviews.....	3
2.1 General.....	3
2.2 Cylinder problems.....	3
2.3 Borehole problems.....	4
Chapter III Poromechanical Response of Finite Cylinder.....	7
3.1 General.....	7
3.2 Basic equation and general solution.....	7
3.3 Finite poroelastic cylinder under axisymmetric loading.....	11
3.4 Numerical results and discussion.....	15
3.5 Conclusion.....	23
Chapter IV Quasi-Static Response of Borehole with Disturbed Zone.....	34
4.1 General.....	34
4.2 General solution.....	34
4.3 Borehole in excavation disturbed zone.....	37
4.4 Formulation of contact problems between a borehole and a rigid cylinder.....	40
4.5 Numerical results and discussion.....	42
4.6 Conclusion.....	47

	Pages
Chapter V Dynamic Response of Borehole with Disturbed Zone	58
5.1 General	58
5.2 Governing equations and general solutions.....	58
5.3 Numerical results and discussion	62
5.4 Conclusion.....	66
Chapter VI Conclusions.....	73
References	75
Appendices.....	78
Appendix A.....	79
Appendix B	81
Appendix C.....	83
Biography.....	85



ศูนย์วิทยทรัพยากร
 จุฬาลงกรณ์มหาวิทยาลัย

LIST OF FIGURES

	Pages
Figure 3.1 Finite poroelastic cylinder under axisymmetric loading	24
Figure 3.2 Comparison with existing solutions for elastic cylinders.....	25
Figure 3.3 Comparison with existing solutions for poroelastic cylinders under plane strain condition	25
Figure 3.4 Poroelastic cylinder ($B=0.90, \nu=0.20, \nu_u=0.40$) subjected to axisymmetric vertical loading for numerical results in Figs. 3.5-3.8.....	26
Figure 3.5 Time histories of (a) radial stress; (b) vertical stress; and (c) excess pore pressure at the center of cylinder for different values of h/a	27
Figure 3.6 Time histories of (a) radial displacement; (b) tangential stress; and (c) vertical stress at the boundary of the mid-plane of cylinder for different values of h/a	27
Figure 3.7 Profiles of (a) vertical displacement; (b) axial stress; (c) excess pore pressure; and (d) vertical discharge along the z -axis of cylinder for different ratios of h/a	28
Figure 3.8 Profiles of tangential stress (a) along the length of the cylinder ($r/a=1$) and (b) at the mid-height ($z/a=0$)	29
Figure 3.9 Poroelastic cylinder ($B=0.90, \nu=0.20, \nu_u=0.40$) capped with rigid plates subjected to (a) confining pressure and (b) vertical loading.	30
Figure 3.10 Profiles of excess pore pressure along the z -axis of cylinder [Fig. 3.9(a)] for different values of h/a	31
Figure 3.11 Time histories of (a) radial displacement, (b) tangential stress, (c) axial stress; and (d) excess pore pressure at the boundary of the mid-plane of cylinder [Fig. 3.9(b)] for different values of h/a	32
Figure 3.12 Profiles of (a) vertical displacement; (b) radial stress; (c) excess pore pressure; and (d) vertical discharge along the z -axis of cylinder [Fig. 3.9(b)] for different values of h/a	33
Figure 4.1 Infinite borehole in poroelastic medium with excavation disturbed zone.....	49

	Pages
Figure 4.2 (a) A rigid cylinder bonded to a borehole with an excavation disturbed zone. (b) Unit radial loading applied over a finite segment	49
Figure 4.3 Comparison with existing solutions for a borehole in a homogenous poroelastic medium with incompressible constituents	50
Figure 4.4 Comparison with existing solutions for a rigid cylinder bonded to a borehole in an elastic medium.....	50
Figure 4.5 Profiles of excess pore pressure along the r -axis due to applied radial traction for different values of (a) m_1 and (b) m_2	51
Figure 4.6 Profiles of fluid discharge along the r -axis due to applied radial traction for different values of (a) m_1 and (b) m_2	52
Figure 4.7 Profiles of (a) displacement and (b) tangential stress different shear modulus along the r -axis due to applied radial traction.....	53
Figure 4.8 Profiles of (a) displacement, (b) tangential stress, (c) excess pore pressure and (d) fluid discharge along the r -axis due to applied fluid pressure.....	54
Figure 4.9 Profile of (a) displacement, (b) tangential stress, (c) excess pore pressure and (d) fluid discharge along the r -axis due to applied fluid discharge.....	55
Figure 4.10 Profile of (a) average radial traction and (b) radial stress along the contact surface for radial misfit.....	56
Figure 4.11 Profile of (a) axial stiffness and (b) tangential stress along the contact surface for applied vertical loading	57
Figure 5.1 Comparison with existing solutions for a borehole in (a) elastic medium and (b) poroelastic medium.....	67
Figure 5.2 Radial displacement at center of loading due to radial traction on (a) permeable wall and (b) impermeable wall	67
Figure 5.3 Tangential stress at center of loading due to radial traction on (a) permeable wall and (b) impermeable wall	68
Figure 5.4 Radial discharge at the center of loading due to radial traction on permeable wall	68
Figure 5.5 Excess pore pressure at the center of loading due to radial traction on impermeable wall	69

Figure 5.6	Profiles of (a) radial displacement and (b) hoop stress along the r -axis due to radial traction on permeable wall	69
Figure 5.7	Profiles of (a) excess pore pressure and (b) radial discharge along the r -axis due to radial traction on permeable wall	70
Figure 5.8	Profiles of (a) radial displacement and (b) hoop stress along the r -axis due to applied fluid pressure on permeable wall	71
Figure 5.9	Profiles of (a) excess pore pressure and (b) radial discharge due to applied fluid pressure on permeable wall.....	72



ศูนย์วิทยทรัพยากร
จุฬาลงกรณ์มหาวิทยาลัย

LIST OF SYMBOLS

a	radius of a solids cylinder and a borehole;
b	parameter accounting for the internal friction of the medium;
B	Skempton's pore pressure coefficient
$f(r)$	externally applied loading;
$\mathbf{F}^{(n)}$	generalized force vector for the n th layer;
I_n	modified Bessel function of the first kind of the n th order.
J_n	Bessel function of the first kind of the n th order.
K_n	modified Bessel function of the second kind of the n th order.
$\mathbf{K}^{(n)}$	stiffness matrix of the n th layer;
M	Biot 's parameters accounting for compressibility of the medium;
m	density-like parameter;
m_1	gradient of shear modulus
m_2	gradient of permeability
p	excess pore pressure;
q_i	fluid discharge in the i -direction;
r	radial coordinate;
s	Laplace transform parameter
S	contact surface between rigid plug and borehole
t	time variable;
u_i	displacement of the solid matrix in the i direction;
$\mathbf{U}^{(n)}$	generalized displacement vector for the n th layer;
w_i	fluid displacement relative to the solid matrix in the i direction;
Y_n	Bessel function of the second kind of the n th order.
z	vertical coordinate;
α	Biot 's parameters accounting for compressibility of the medium;
δ	non-dimensional frequency;
δ_{ij}	Kronecker delta;
ε	dilatation of the solid matrix;
κ	coefficient of permeability
λ	Lame's constant of the bulk material;

μ	shear modulus of the bulk material;
ν	drained Poisson's ratio
ν_u	nu undrained Poisson's ratio
ρ	mass density of the bulk material;
ρ_f	mass density of the pore fluid;
σ_{ij}	total stress component of the bulk material;
ω	time frequency of motion
ξ	Hankel transform parameter;
ζ	variation of fluid volume per unit reference volume;



ศูนย์วิทยทรัพยากร
จุฬาลงกรณ์มหาวิทยาลัย

CHAPTER I

INTRODUCTION

1.1 General

An important class of problems encountered in mechanics is concerned with the study of mechanical response of cylindrical specimens since they are widely found in civil engineering laboratory and in-situ testing for concrete, soils and rocks. For example, solid circular cylinders are the most commonly used specimens in various standard tests in engineering applications, such as uni-axial compression tests, tri-axial compression tests, double-punch tests and point load strength tests, etc. Hollow cylindrical specimens are also widely used in rock engineering laboratory to estimate material properties for hydraulic fracturing, subsidence phenomena and breakout angle. In addition, a cylindrical borehole drilled in a soil/rock medium is commonly found in the petroleum industry. Stability of borehole is important because it is the one of major problems in oil and gas industries. The failure of the soil/rock around the borehole is a common problem, and it causes a variety of drilling delays and expenses running into hundreds of millions of dollars per year.

In the past, the classical theory of elasticity has been used extensively to analyze various elastostatic and elastodynamic problems involving cylinders and boreholes. Traditionally, field equations have been formulated on the assumption that the medium is a single-phase elastic solid. However, geological materials are normally two-phase materials consisting of a solid skeleton with voids filled with water. Such materials are commonly known as poroelastic materials and widely considered as much more realistic representation for natural soils and rocks than ideal elastic materials. Biot developed theories of poroelasticity for quasi-static (1941) and dynamic (1956) problems respectively to account for fluid stress and strain. Later, other poroelastic theories have also been developed by using the mixture theory concepts but in practice they do not offer any significant advantage over Biot's theory. Over the last five decades, Biot's theories have been employed for analysis of various practical problems encountered in geomechanics, geophysics, earthquake engineering and energy resource explorations. Nevertheless, several theoretical models involving poroelastic materials that could be useful for laboratory and in-situ tests in civil engineering have not been presented. For example, theoretical modeling of three-dimensional consolidation of a solid cylinder in the laboratory has never been reported in the literature. In addition, existing studies on stress analysis of a borehole have not included the excavation disturbed zone due to borehole drilling process.

The present study is concerned with the development of analytical solutions for cylinder and borehole based on Biot's theory of poroelasticity, which can be used for theoretical modeling of various geomechanics problems. The analytical solution for a solid poroelastic cylinder of finite length subjected to axisymmetric loading is presented in Chapter III. The quasi-static solutions of an infinite cylindrical borehole in a poroelastic medium subjected to surface loading, and contact problems between a rigid cylinder bonded to a borehole in poroelastic material are also presented in Chapter IV. The surrounding medium in the vicinity of the borehole is considered to be a disturbed zone due to the processes induced by excavation. The dynamic response of an infinite borehole in poroelastic medium with consideration of excavation disturbed zone is also presented in Chapter V. Objectives and scopes of this study are defined in the following section.

1.2 Objectives and Scopes of Present Study

The main objectives and scopes of the present study are given as follows

1. The general solutions corresponding to a finite solid poroelastic cylinder, and an infinite borehole in a poroelastic medium with consideration of excavation disturbed zone subjected to axisymmetric loading and fluid sources are derived. Both fully permeable and impermeable flow boundary conditions are considered. These solutions can be used in the analysis of a variety of boundary value problems encountered in civil engineering applications.
2. Numerical solutions for several boundary value problems relevant to cylinders and boreholes are presented to study the influence of poroelastic material properties and other governing parameters, and to demonstrate the key features of coupled poroelastic response.

ศูนย์วิทยทรัพยากร
จุฬาลงกรณ์มหาวิทยาลัย

CHAPTER II

LITERATURE REVIEWS

2.1 General

The theory of poroelasticity has its origin in the one-dimensional theory of soil consolidation proposed by Terzaghi (1923). Biot (1941) developed a general theory of three-dimensional consolidation by adopting Terzaghi's concepts. Biot's theory is based on the classical theory of elasticity and Darcy's laws, and it takes into account the coupling between the solid and fluid stresses and strains. Rice and Cleary (1976) reformulated Biot's theory (1941) in terms of Skempton's pore pressure coefficients (Skempton 1954) and the undrained Poisson's ratio of the bulk material. The first theory of wave propagation in porous elastic solid was also established by Biot (1956) by adding inertia terms to his original theory (Biot 1941). Thereafter, Biot's theory has widely been applied to a variety of consolidation and wave propagation problems in soil engineering, rock mechanics, biomedical engineering and energy resource explorations. The present study is concerned with the development of analytical solutions for cylinders and boreholes by employing Biot's theory of poroelasticity. In the following sections, a review of literature related to stress analysis of cylinders and boreholes is presented.

2.2 Cylinder Problems

Stress analysis of finite elastic cylinders has received considerable attention in the past due to its close relevance to geotechnical and rock testing methods such as uni-axial and tri-axial compression tests, double-punch tests and point load strength tests, etc. In addition, stress analysis of cylinders is also relevant to applications involving biomedical and mechanical engineering. Lekhnitskii (1963) and Vendhan and Archer (1978) presented the early analytical solutions for transversely isotropic elastic cylinders by using the methods of stress functions and displacement functions respectively. Later, Chau and Wei (2000) derived the general solution for an isotropic elastic solid cylinder of finite length subjected to arbitrary surface loading based on two displacement functions. Theoretical models of several engineering tests were also presented by Watanabe (1996), Wei et al. (1999) and Chau and Wei (2001) for isotropic cylinders, and by Wei and Chau (2002) for transversely isotropic materials.

In the context of poroelastic materials, Abousleiman et al. (1996) and Abousleiman and Cui (1998) presented plane strain poroelastic solutions for infinite cylinders subjected to

axial strain and confining pressure. Cui and Abousleiman (2001) developed a general solution based on the generalized plane strain conditions for a poroelastic cylinder under an axial load and confining pressure, and examined the poroelastic effects in rock samples under uni-axial and tri-axial testing conditions. Kanj et al. (2003) presented plane strain solutions for a fully saturated transversely isotropic hollow cylinder under various loading conditions relevant to laboratory testing. Recently, Jourine et al. (2004) proposed a general poroelastic solution for radially symmetric plane strain problems to model laboratory testing of thick-walled hollow cylinders with time-dependent boundary conditions. The above studies assumed plane strain conditions, which are valid for certain types of loading and boundary conditions. Most soil/rock testing involves cylindrical specimens subjected to axisymmetric loading and the stresses, pore pressure and fluid flow do not reflect plane strain behavior due to cylinder end effects and loading conditions. It is therefore important to examine the poroelastic field under practical test conditions using a 3-D model that allows better understanding of laboratory results and interpretation of material properties. However, a 3-D model for a finite poroelastic cylinder has not appeared in the literature.

2.3 Borehole Problems

Stress analysis of cylindrical boreholes in soils and rocks is of fundamental importance to several engineering applications such as in-situ testing of geological materials, energy and mineral resource explorations, waste disposal and groundwater discharge, etc. In the past, several studies investigated the response of a deep cylindrical borehole in an isotropic or a transversely isotropic elastic medium to static and dynamic loading applied to borehole surface. For example, Jordan (1962) solved a dynamic problem of suddenly applied pressure over finite interval of the borehole. The corresponding static solution of radially applied axisymmetric traction was also presented by Parnes (1982). Parnes (1983, 1986) later presented time-harmonic response of a borehole cylinder under axisymmetric torsional and ring loading. In addition, Rajapakse and Gross (1996) derived analytical solutions for axisymmetric displacements and stresses, and then solved boundary value problems involving an infinite borehole in a transversely isotropic medium subjected to axisymmetric traction and a rigid cylinder perfectly bonded to a borehole wall. Robinson (2002) subsequently considered the contact problem between a rigid cylinder and a borehole wall, and determined the singularity at the cylinder edges by using Neumann Bessel function series representations of the kernels of shear and radial stress integral expressions.

All studies mentioned in the foregoing paragraph considered the surrounding medium as single-phase elastic materials. A poroelastic solution for a borehole in a non-hydrostatic

stress field was presented by Detournay and Cheng (1988) by assuming and plane strain conditions. Analytical solutions based on the generalized plane strain concept for inclined boreholes in isotropic and transversely isotropic poroelastic media also exist in the literature (Cui et al. 1997 and Abousleiman and Cui 1998). Rajapakse (1993) considered axisymmetric stress analysis of a cylindrical borehole in an infinite poroelastic medium with incompressible constituents by using Laplace-Fourier integral transforms. Abousleiman et al. (1997) presented a pseudo-three dimensional solution for an inclined borehole problem. Their solution has found widespread industry applications in evaluating impacts of the poroelastic processes on borehole stability (Cui et al. 1998 and Cui et al. 1999). An analytical solution for an inclined borehole subjected to arbitrary time-dependent far-field stresses and pore fluid boundary condition at the borehole wall was also developed by Ekbote et al. (2004). Recently, Abousleiman and Chen (2010) presented stress analysis of a borehole subjected to fluid discharge over a finite segment of the surface coupled with the three-dimensional far-field in-situ stresses. The wave propagation problem related to an infinite borehole was also considered by Lu and Jeng (2006), who presented dynamic response of an infinite borehole in a poroelastic medium subjected to radial ring force at the borehole.

It is well known that borehole drilling process is a primary factor in causing changes of physical, mechanical, and hydraulic properties around the borehole, such as bulk modulus, shear modulus, desaturation, and strength. The rock/soil zone, where its properties are changed, is called an excavation disturbed zone (EDZ). The EDZ is one of the most important factors that affect the stability of borehole. Several researches have studied behaviors of the excavation disturbed zone in the past decade. For example, Sato et al. (2000) performed an excavation disturbance experiment in the Neogene sedimentary soft rock at Tono mine central Japan to observe the change of rock properties and the width of the EDZ during the drift excavation. Martino and Chandler (2004) studied the behavior of the EDZ at the Underground Research Laboratory (URL) located in Manitoba, Canada to understand the character and the extent of excavation damage. The EDZ investigation was conducted at the mine using seismic measurement techniques by Malmgren et al. (2007) to determine the mechanical properties of EDZ at Kiiranaavaara mine, Sweden. The influence of hydro-mechanical properties (desaturation and anisotropy) in the EDZ at the underground research laboratory in France was carried out by Shao et al. (2008). Recently, Kwon et al. (2009) used in-situ, laboratory tests, and computer simulations to investigate characteristics of the excavation damage zone developed during a Korean tunnel contracture.

Based on a survey of literature mentioned above, it is found that both quasi-static and dynamic responses of a cylindrical borehole in a poroelastic medium with an excavation

disturbed zone have never been considered in the past, although the EDZ has a significant influence on a change in rock/soil properties, which is directly related to displacement, stress, excess pore pressure, and fluid flow around the borehole. The consideration of the EDZ is then essential for an optimal design of the drilling process. In this study, the general solutions both quasi-static and dynamic responses of a borehole in a poroelastic medium are derived by considering the effect of the excavation disturbed zone.



ศูนย์วิทยทรัพยากร
จุฬาลงกรณ์มหาวิทยาลัย

CHAPTER III

POROMECHANICAL RESPONSE OF FINITE CYLINDER

3.1 General

Drained or undrained cylindrical specimens under axisymmetric loading are commonly used in laboratory testing of soils and rocks. Poroelastic cylindrical elements are also encountered in applications related to bioengineering and advanced materials. In this chapter, a new analytical solution for a solid poroelastic cylinder of finite length subjected to axisymmetric loading is presented. Both fully permeable (drained) and impermeable (undrained) flow boundary conditions are considered. The general solutions are derived by first applying the Laplace transform with respect to time and then solving the resulting governing equations in terms of Fourier-Bessel series, which involve trigonometric and hyperbolic functions with respect to the z -coordinate and Bessel functions with respect to the r -coordinate. Several time-dependent boundary-value problems are solved to demonstrate the application of the general solution to practical situations. Time domain solutions are obtained by using a numerical Laplace inversion scheme. Selected numerical results are presented for different axisymmetric loading, hydraulic boundary conditions, cylinder aspect ratios and material properties to understand the salient features of the poroelastic field of a cylinder and its relevance to laboratory testing.

3.2 Basic Equation and General Solution

Consider a solid poroelastic cylinder of radius a and height $2h$ subjected to axisymmetric loading as shown in Fig. 3.1. A cylindrical polar coordinate system (r, θ, z) is used with the z -axis parallel to the axis of the cylinder. The governing equations given by Rice and Cleary (1976) for a poroelastic material undergoing axisymmetric deformations are

$$\left(\frac{\partial^2}{\partial r^2} + \frac{1}{r} \frac{\partial}{\partial r} + \frac{\partial^2}{\partial z^2} \right) u_r + \frac{1}{(1-2\nu_u)} \frac{\partial \varepsilon}{\partial r} - \frac{u_r}{r^2} - \frac{2B(1+\nu_u)}{3(1-2\nu_u)} \frac{\partial \zeta}{\partial r} = 0 \quad (3.1)$$

$$\left(\frac{\partial^2}{\partial r^2} + \frac{1}{r} \frac{\partial}{\partial r} + \frac{\partial^2}{\partial z^2} \right) u_z + \frac{1}{(1-2\nu_u)} \frac{\partial \varepsilon}{\partial z} - \frac{2B(1+\nu_u)}{3(1-2\nu_u)} \frac{\partial \zeta}{\partial z} = 0 \quad (3.2)$$

$$\left(\frac{\partial^2}{\partial r^2} + \frac{1}{r} \frac{\partial}{\partial r} + \frac{\partial^2}{\partial z^2} \right) \zeta = \frac{1}{c} \frac{\partial \zeta}{\partial t} \quad (3.3)$$

where

$$c = \frac{2 \mu \kappa B^2 (1 - \nu)(1 + \nu_u)^2}{9 (1 - \nu_u)(\nu_u - \nu)} \quad (3.4)$$

In the above equations, u_i denotes the displacement of solid matrix in the i -direction ($i = r, z$); ε is the dilatation of the solid matrix; μ , ν , ν_u and κ denote the shear modulus, drained and undrained Poisson's ratios, and the coefficient of permeability of the cylinder respectively; B is the Skempton's pore pressure coefficient (Skempton 1954); ζ denotes the variation of fluid volume per unit reference volume, defined as $\zeta = -w_{i,i}$, in which w_i denotes the fluid displacement relative to the displacement of solid matrix in the i -direction ($i = r, z$).

The constitutive relations can be expressed as

$$\sigma_{rr} = 2\mu \left(\frac{\partial u_r}{\partial r} + \frac{\nu}{1-2\nu} \varepsilon \right) - \frac{3(\nu_u - \nu)}{B(1-2\nu)(1+\nu_u)} p \quad (3.5)$$

$$\sigma_{\theta\theta} = 2\mu \left(\frac{u_r}{r} + \frac{\nu}{1-2\nu} \varepsilon \right) - \frac{3(\nu_u - \nu)}{B(1-2\nu)(1+\nu_u)} p \quad (3.6)$$

$$\sigma_{zz} = 2\mu \left(\frac{\partial u_z}{\partial z} + \frac{\nu}{1-2\nu} \varepsilon \right) - \frac{3(\nu_u - \nu)}{B(1-2\nu)(1+\nu_u)} p \quad (3.7)$$

$$\sigma_{rz} = \mu \left(\frac{\partial u_r}{\partial z} + \frac{\partial u_z}{\partial r} \right) \quad (3.8)$$

where σ_{rr} , $\sigma_{\theta\theta}$, σ_{zz} and σ_{rz} denote the total stress components of the bulk material. Note that the tension positive sign convention for stresses and strains is adopted here. In addition, p is the excess pore fluid pressure (suction is considered negative), which can be expressed in terms of dilatation and variation of fluid volume as

$$\frac{p}{2\mu} = -\frac{B(1+\nu_u)}{3(1-2\nu_u)} \varepsilon + \frac{B^2(1-2\nu)(1+\nu_u)^2}{9(1-2\nu_u)(\nu_u - \nu)} \zeta \quad (3.9)$$

The fluid discharge in the i -direction ($i = r, z$) denoted by q_i is given by

$$q_i = -\kappa \frac{\partial p}{\partial i} \quad (3.10)$$

Note that q_i is also related to w_i such that $q_i = \partial w_i / \partial t$.

At this stage, it is convenient to nondimensionalize all quantities including the coordinates with respect to length and time by selecting the radius of the cylinder “ a ” as a

unit length and “ a^2 / c ” as a unit of time respectively. All variables are replaced by the corresponding nondimensional variables but the previous notations are used for convenience.

The Laplace transform of a function $\phi(r, z, t)$ with respect to time variable t and its inverse transform are given respectively by (Snedden 1951)

$$\bar{\phi}(r, z, s) = \int_0^{\infty} \phi(r, z, t) e^{-st} dt \quad (3.11)$$

$$\phi(r, z, t) = \frac{1}{2\pi i} \int_{\alpha-i\infty}^{\alpha+i\infty} \bar{\phi}(r, z, s) e^{st} ds \quad (3.12)$$

where s is the Laplace transform parameter, the line $\text{Re}(s) = \alpha$ is to the right of all singularities of $\bar{\phi}$ and $i = \sqrt{-1}$.

Application of the Laplace transform to Eq. (3.3) yields

$$\left(\frac{\partial^2}{\partial r^2} + \frac{1}{r} \frac{\partial}{\partial r} + \frac{\partial^2}{\partial z^2} \right) \bar{\zeta} = s \bar{\zeta} \quad (3.13)$$

The above equation can be solved directly by considering a function of the form $\bar{\zeta}(r, z, s) = \bar{R}(r, s) \bar{Z}(z, s)$. It can be shown that

$$\begin{aligned} \bar{\zeta} = & \sum_{m=0}^{\infty} [A_{1m} J_0(\lambda_m r) + A_{2m} Y_0(\lambda_m r)] [A_{3m} \cosh(\gamma_m z) + A_{4m} \sinh(\gamma_m z)] \\ & + \sum_{n=0}^{\infty} [B_{1n} I_0(\beta_n r) + B_{2n} K_0(\beta_n r)] [B_{3n} \cos(\chi_n z) + B_{4n} \sin(\chi_n z)] \end{aligned} \quad (3.14)$$

where $\gamma_m = \sqrt{\lambda_m^2 + s}$; $\beta_n = \sqrt{\chi_n^2 + s}$; λ_m is the m th root of $J_1(\lambda_m) = 0$; $\chi_n = n\pi / h$; and A_{im} and B_{in} ($i=1, 2, 3, 4$; $m, n=0, 1, 2, \dots, \infty$) are arbitrary functions. In addition, J_n and Y_n are Bessel functions of first and the second kinds respectively of the n th order; and I_n and K_n are modified Bessel functions of the first and second kinds respectively of the n th order (Watson 1944).

Since the stress field at the center of a solid cylinder must be bounded, all terms that related to $Y_0(\lambda_m r)$ and $K_0(\beta_n r)$ are inadmissible. In addition, the solution of the variation of fluid volume ($\bar{\zeta}$) should contain only even functions of z since the applied loading is

symmetric with respect to the mid-plane of the cylinder. Therefore, the admissible complete solution of the variation of fluid volume is obtained from Eq. (3.14) as,

$$\bar{\zeta} = \sum_{m=0}^{\infty} A_m J_0(\lambda_m r) \cosh(\gamma_m z) + \sum_{n=0}^{\infty} B_n I_0(\beta_n r) \cos(\chi_n z) \quad (3.15)$$

where A_m and B_n ($m, n=0, 1, 2, \dots, \infty$) are arbitrary functions to be determined.

Differentiation of Eqs. (3.1) and (3.2), and subsequent manipulations yields,

$$\left(\frac{\partial^2}{\partial r^2} + \frac{1}{r} \frac{\partial}{\partial r} + \frac{\partial^2}{\partial z^2} \right) \bar{\varepsilon} = \eta \left(\frac{\partial^2}{\partial r^2} + \frac{1}{r} \frac{\partial}{\partial r} + \frac{\partial^2}{\partial z^2} \right) \bar{\zeta} \quad (3.16)$$

where $\eta = B(1 + \nu_u) / 3(1 - \nu_u)$. Application of the Laplace transform to Eq. (3.16) and the substitution of Eq. (3.15) result in

$$\begin{aligned} \bar{\varepsilon} &= \sum_{m=0}^{\infty} [\eta A_m \cosh(\gamma_m z) + C_m \cosh(\lambda_m z)] J_0(\lambda_m r) \\ &+ \sum_{n=0}^{\infty} [\eta B_n I_0(\beta_n r) + D_n I_0(\chi_n r)] \cos(\chi_n z) \end{aligned} \quad (3.17)$$

where C_m and D_n ($m, n=0, 1, 2, \dots, \infty$) are arbitrary functions. Consequently, the radial and vertical displacements in the Laplace domain are obtained by substituting Eqs. (3.15) and (3.17) into Eqs. (3.1) and (3.2). The resulting solutions are

$$\bar{u}_r(r, z, s) = \bar{u}_{r0}(r, s) + \sum_{m=1}^{\infty} \bar{u}_{rm}(z, s) J_1(\lambda_m r) + \sum_{n=1}^{\infty} \bar{u}_{rn}(r, s) \cos(\xi_n z) \quad (3.18)$$

$$\bar{u}_z(r, z, s) = \bar{u}_{z0}(z, s) + \sum_{m=1}^{\infty} \bar{u}_{zm}(z, s) J_0(\lambda_m r) + \sum_{n=1}^{\infty} \bar{u}_{zn}(r, s) \sin(\xi_n z) \quad (3.19)$$

where

$$\bar{u}_{r0}(r, s) = \eta s^{-1/2} B_0 I_1(\beta_0 r) + D_0 r / 2 \quad (3.20)$$

$$\bar{u}_{rm}(z, s) = -\eta \lambda_m s^{-1} A_m \cosh(\gamma_m z) + [\lambda_m^{-1} \cosh(\lambda_m z) + a_1 z \sinh(\lambda_m z)] C_m - E_m \cosh(\lambda_m z) \quad (3.21)$$

$$\bar{u}_{rn}(r, s) = \eta \beta_n s^{-1} B_n I_1(\beta_n r) - [a_1 r I_0(\chi_n r) - 2a_2 \chi_n^{-1} I_1(\chi_n r)] D_n - F_n I_1(\chi_n r) \quad (3.22)$$

$$\bar{u}_{z0}(z, s) = \eta s^{-1/2} A_0 \sinh(\gamma_0 z) + C_0 z \quad (3.23)$$

$$\bar{u}_{zm}(z, s) = \eta\gamma_m s^{-1} A_m \sinh(\gamma_m z) + [a_1 \lambda_m^{-1} \sinh(\lambda_m z) - a_1 z \cosh(\lambda_m z)] C_m + E_m \sinh(\lambda_m z) \quad (3.24)$$

$$\bar{u}_{zn}(r, s) = -\eta\chi_n s^{-1} B_n I_0(\beta_n r) + a_1 r D_n I_1(\chi_n r) + F_n I_0(\chi_n r) \quad (3.25)$$

In addition, $a_1 = 1/2(1-2\nu_u)$; $a_2 = (1-\nu_u)/(1-2\nu_u)$; E_m and F_n ($m, n = 1, 2, 3, \dots, \infty$) are arbitrary functions.

In view of Eqs. (3.5)-(3.10), (3.15) and (3.17)-(3.19), the general solutions of stresses, pore fluid pressure and fluid discharge in the Laplace domain can be expressed as,

$$\begin{aligned} \frac{\bar{\sigma}_{rr}(r, z, s)}{2\mu} &= \bar{\sigma}_{rr0}(r, z, s) + \sum_{m=1}^{\infty} \bar{\sigma}_{rrm}^{(1)}(z, s) J_0(\lambda_m r) + \sum_{m=1}^{\infty} \bar{\sigma}_{rrm}^{(2)}(z, s) r^{-1} J_1(\lambda_m r) \\ &\quad + \sum_{n=1}^{\infty} \bar{\sigma}_{rrn}(r, s) \cos(\chi_n z) \end{aligned} \quad (3.26)$$

$$\frac{\bar{\sigma}_{zz}(r, z, s)}{2\mu} = \bar{\sigma}_{zz0}(r, z, s) + \sum_{m=1}^{\infty} \bar{\sigma}_{zzm}(z, s) J_0(\lambda_m r) + \sum_{n=1}^{\infty} \bar{\sigma}_{zzn}(r, s) \cos(\chi_n z) \quad (3.27)$$

$$\begin{aligned} \frac{\bar{\sigma}_{\theta\theta}(r, z, s)}{2\mu} &= \bar{\sigma}_{\theta\theta0}(r, z, s) + \sum_{m=1}^{\infty} \bar{\sigma}_{\theta\theta m}^{(1)}(z, s) J_0(\lambda_m r) + \sum_{m=1}^{\infty} \bar{\sigma}_{\theta\theta m}^{(2)}(z, s) r^{-1} J_1(\lambda_m r) \\ &\quad + \sum_{n=1}^{\infty} \bar{\sigma}_{\theta\theta n}(r, s) \cos(\chi_n z) \end{aligned} \quad (3.28)$$

$$\frac{\bar{\sigma}_{rz}(r, z, s)}{2\mu} = \sum_{m=1}^{\infty} \bar{\sigma}_{rzm}(z, s) J_1(\lambda_m r) + \sum_{n=1}^{\infty} \bar{\sigma}_{rzn}(r, s) \sin(\chi_n z) \quad (3.29)$$

$$\frac{\bar{p}(r, z, s)}{2\mu} = \bar{p}_0(r, z, s) + \sum_{m=1}^{\infty} \bar{p}_m(z, s) J_0(\lambda_m r) + \sum_{n=1}^{\infty} \bar{p}_n(r, s) \cos(\chi_n z) \quad (3.30)$$

$$\frac{\bar{q}_r(r, z, s)}{2\mu} = \bar{q}_{r0}(r, z, s) + \sum_{m=1}^{\infty} \bar{q}_{rm}(z, s) J_1(\lambda_m r) + \sum_{n=1}^{\infty} \bar{q}_{rn}(r, s) \cos(\chi_n z) \quad (3.31)$$

$$\frac{\bar{q}_z(r, z, s)}{2\mu} = \bar{q}_{z0}(r, z, s) + \sum_{m=1}^{\infty} \bar{q}_{zm}(z, s) J_0(\lambda_m r) + \sum_{n=1}^{\infty} \bar{q}_{zn}(r, s) \sin(\chi_n z) \quad (3.32)$$

where $\bar{\sigma}_{rr0}$, $\bar{\sigma}_{rrm}^{(1)}$, $\bar{\sigma}_{rrm}^{(2)}$, $\bar{\sigma}_{rrn}$, $\bar{\sigma}_{zz0}$, $\bar{\sigma}_{zzm}$, $\bar{\sigma}_{zzn}$, $\bar{\sigma}_{\theta\theta0}$, $\bar{\sigma}_{\theta\theta m}^{(1)}$, $\bar{\sigma}_{\theta\theta m}^{(2)}$, $\bar{\sigma}_{\theta\theta n}$, $\bar{\sigma}_{rz0}$, $\bar{\sigma}_{rzm}$, $\bar{\sigma}_{rzn}$, \bar{p}_0 , \bar{p}_m , \bar{p}_n , \bar{q}_{r0} , \bar{q}_{rm} , \bar{q}_{rn} , \bar{q}_{z0} , \bar{q}_{zm} and \bar{q}_{zn} are given in Appendix A.

3.3 Finite Poroelastic Cylinder under Axisymmetric Loading

Consider a solid cylinder subjected to axisymmetric radial traction $F_r(z, t)$ on the curved surface and axisymmetric vertical traction $F_z(r, t)$ at the end surfaces as shown in Fig.

3.1. A linear algebraic equation system can be established to determine the arbitrary functions appearing in Eqs. (3.18)-(3.32) by applying the appropriate boundary conditions on the

cylinder surfaces. There are three boundary conditions at the curved surface and three at each end surface. The stress boundary conditions at the curved surface can be expressed in the Laplace domain as

$$\bar{\sigma}_{rr}(1, z, s) = \bar{F}_r(z, s) \quad (3.33)$$

$$\bar{\sigma}_{rz}(1, z, s) = 0 \quad (3.34)$$

where $\bar{F}_r(z, s)$ is the Laplace transform of radial traction applied at the curved surface. In addition, the hydraulic boundary condition can be expressed either as

$$\bar{p}(1, z, s) = 0; \quad \text{for fully permeable surface} \quad (3.35)$$

$$\text{or } \bar{q}_r(1, z, s) = 0; \quad \text{for impermeable surface} \quad (3.36)$$

The remaining three boundary conditions at each end surface can be expressed as

$$\bar{\sigma}_{rz}(r, \pm h, s) = 0 \quad (3.37)$$

$$\bar{\sigma}_{zz}(r, \pm h, s) = \bar{F}_z(r, s) \quad (3.38)$$

where $\bar{F}_z(r, s)$ is the Laplace transform of vertical traction applied at the end surfaces. In addition,

$$\bar{p}(r, \pm h, s) = 0 \quad \text{for fully permeable surface} \quad (3.39)$$

$$\text{or } \bar{q}_z(r, \pm h, s) = 0 \quad \text{for impermeable surface} \quad (3.40)$$

The above boundary conditions given by Eqs. (3.33)-(3.40) are used to determine all arbitrary functions appearing in the general solutions. First, consider the boundary conditions on the curved surface, i.e., Eqs. (3.33) and (3.34). They can be expressed by using Eqs. (3.26) and (3.29) as,

$$\bar{\sigma}_{rr0}(1, z, s) + \sum_{m=1}^{\infty} \bar{\sigma}_{rrm}^{(1)}(z, s) J_0(\lambda_m) + \sum_{n=1}^{\infty} \bar{\sigma}_{rrn}(1, s) \cos(\chi_n z) = \bar{F}_r(z, s) \quad (3.41)$$

$$\sum_{n=1}^{\infty} \bar{\sigma}_{rzn}(1, s) \sin(\chi_n z) = 0 \quad (3.42)$$

The applied radial traction at the curved surface $\bar{F}_r(z, s)$ can be expanded in terms of Fourier cosine series as

$$\bar{F}_r(z, s) = \bar{F}_{r0}(s) + \sum_{n=1}^{\infty} \bar{F}_n(s) \cos(\xi_n z) \quad (3.43)$$

where

$$\bar{F}_{r0}(s) = \frac{1}{2h} \int_{-h}^h \bar{F}_r(z, s) dz; \quad \bar{F}_n(s) = \frac{1}{h} \int_{-h}^h \bar{F}_r(z, s) \cos(\xi_n z) dz \quad (3.44)$$

Next, expanding all functions of z appearing in the left hand side of Eq. (3.41) in terms of Fourier cosine series to match with the applied loading function expressed by Eq. (3.43). This results in,

$$-\eta A_0 Q_0(\sqrt{s}) / 2 - \eta s^{-1/2} B_0 I_1(\sqrt{s}) + a_3 C_0 + a_1 D_0 + \sum_{m=1}^{\infty} \frac{J_0(\lambda_m)}{2} \left[-\eta \gamma_m^2 s^{-1} Q_0(\gamma_m) A_m + [a_2 Q_0(\lambda_m) + a_1 \lambda_m R_0(\lambda_m)] C_m - \lambda_m Q_0(\lambda_m) E_m \right] = \bar{F}_{r0}(s) \quad (3.45)$$

$$\sum_{m=1}^{\infty} J_0(\lambda_m) \left[-\eta \gamma_m^2 s^{-1} Q_n(\gamma_m) A_m + [a_4 Q_n(\lambda_m) + a_1 \lambda_m R_n(\lambda_m)] C_m - \lambda_m Q_n(\lambda_m) E_m \right] + \left[\eta \xi_n^2 s^{-1} I_0(\beta_n) - \eta \beta_n s^{-1} I_1(\beta_n) \right] B_n + \left[(a_1 + a_4) I_0(\chi_n) - (a_1 \xi_n + 2a_4 \chi_n^{-1}) I_1(\chi_n) \right] D_n - \eta A_0 Q_n(\sqrt{s}) - [\chi_n I_0(\chi_n) - I_1(\chi_n)] F_n = \bar{F}_n(s) \quad (3.46)$$

where

$$Q_n(\alpha_m) = \frac{2(-1)^n \alpha_m \sinh(\alpha_m h)}{h(\alpha_m^2 + \chi_n^2)} \quad (3.47)$$

$$R_n(\alpha_m) = 2(-1)^n \left[\frac{\alpha_m \cosh(\alpha_m h)}{(\alpha_m^2 + \chi_n^2)} + \frac{(\chi_n^2 - \alpha_m^2) \sinh(\alpha_m h)}{h(\alpha_m^2 + \chi_n^2)^2} \right] \quad (3.48)$$

Similarly, the application of the boundary conditions for zero shear stress at the curved surface, i.e. Eq. (3.34), and at the cylinder ends, Eq. (3.37), respectively yields the following equations.

$$-\eta \chi_n \beta_n s^{-1} B_n I_1(\beta_n) + [a_1 \chi_n I_0(\xi_n) - a_2 I_1(\chi_n)] D_n + \chi_n F_n I_1(\chi_n) = 0 \quad (3.49)$$

$$-\eta \lambda_m \gamma_m s^{-1} A_m \sinh(\gamma_m h) + [\sinh(\lambda_m h) / 2 + a_1 \lambda_m h \cosh(\lambda_m h)] C_m - \lambda_m E_m \sinh(\lambda_m h) = 0 \quad (3.50)$$

Finally, in view of Eq. (3.27), the remaining stress boundary condition at both ends of the cylinder corresponding to the applied vertical traction, Eq. (3.38), can be rewritten as

$$\bar{\sigma}_{z0}(r, h, s) + \sum_{m=1}^{\infty} \bar{\sigma}_{zm}(h) J_0(\lambda_m r) + \sum_{n=1}^{\infty} \bar{\sigma}_{zn}(r) \cos(\chi_n h) = \bar{F}_z(r, s) \quad (3.51)$$

where

$$\bar{F}_z(r, s) = \bar{F}_{z0}(s) + \sum_{m=1}^{\infty} \bar{F}_{zm}(s) J_0(\lambda_m r) \quad (3.52)$$

and

$$\bar{F}_{z0}(s) = 2 \int_0^1 r \bar{F}_z(r, s) dr; \quad \bar{F}_{zm}(s) = \frac{2}{J_0^2(\lambda_m)} \int_0^1 \bar{F}_z(r, s) r J_0(\lambda_m r) dr \quad (3.53)$$

Substitution of Eq. (3.53) into Eq. (3.52) together with the expansion of all functions of r appearing in Eq. (3.51) in terms of Fourier-Bessel series of order zero yields,

$$a_2 A_0 - \eta B_0 S_0(\sqrt{s}) + a_3 D_0 + \sum_{n=1}^{\infty} (-1)^n \left[-\eta \beta_n^2 s^{-1} S_0(\beta_n) B_n + [a_3 S_0(\chi_n) + a_1 \chi_n T_0(\chi_n)] D_n + \xi_n S_0(\chi_n) F_n \right] = \bar{F}_{z0}(s) \quad (3.54)$$

$$-\eta B_0 S_m(\sqrt{s}) + \eta \lambda_m^2 s^{-1} A_m \cosh(\gamma_m h) + [a_3 \cosh(\lambda_m h) - a_1 \lambda_m h \sinh(\lambda_m h)] C_m + \lambda_m E_m \cosh(\lambda_m z) + \sum_{n=1}^{\infty} (-1)^n \left[-\eta \beta_n^2 s^{-1} S_m(\beta_n) B_n + [a_3 S_m(\chi_n) + a_1 \chi_n T_m(\chi_n)] D_n + \xi_n S_m(\chi_n) F_n \right] = \bar{F}_{zm}(s) \quad (3.55)$$

where

$$S_m(\zeta_n) = \frac{2\zeta_n I_1(\zeta_n)}{(\lambda_m^2 + \zeta_n^2) J_0(\lambda_m)} \quad (3.56)$$

$$T_m(\zeta_n) = \frac{2}{J_0(\lambda_m)} \left[\frac{\zeta_n I_0(\zeta_n)}{\lambda_m^2 + \zeta_n^2} - \frac{2\zeta_n^2 I_1(\zeta_n)}{(\lambda_m^2 + \zeta_n^2)^2} \right] \quad (3.57)$$

Thereafter, expanding all functions of r into Fourier-Bessel series of order zero and all functions of z into Fourier cosine series, the hydraulic boundary conditions for a permeable surface, i.e. Eqs. (3.35) and (3.39), can be expressed as,

$$a_4 \eta \left[A_0 Q_0(\sqrt{s}) / 2 + B_0 I_0(\sqrt{s}) \right] - a_2 \eta [C_0 + D_0] + \sum_{m=1}^{\infty} \frac{J_0(\lambda_m)}{2} [a_4 \eta Q_0(\gamma_m) A_m - a_2 \eta Q_0(\lambda_m) C_m] = 0 \quad (3.58)$$

$$a_4 \eta A_0 Q_n(\sqrt{s}) + \sum_{m=1}^{\infty} J_0(\lambda_m) [a_4 \eta Q_n(\gamma_m) A_m - a_2 \eta Q_n(\lambda_m) C_m] + a_4 \eta B_n I_0(\beta_n) - a_2 \eta D_n I_0(\chi_n) = 0 \quad (3.59)$$

$$a_4\eta\left[A_0 \cosh(\sqrt{s}h) + B_0 S_0(\sqrt{s})\right] - a_4\eta[C_0 + D_0] + \sum_{n=1}^{\infty} (-1)^n \eta [a_4 B_n S_0(\beta_n) - a_2 D_n S_0(\chi_n)] = 0 \quad (3.60)$$

$$a_4\eta B_0 S_m(\sqrt{s}) + a_4\eta A_m \cosh(\gamma_m h) - a_2\eta C_m \cosh(\lambda_m h) + \sum_{n=1}^{\infty} (-1)^n \eta [a_4 B_n S_n(\beta_n) - a_2 D_n S_n(\chi_n)] = 0 \quad (3.61)$$

Similarly, for an impermeable surface Eqs. (3.36) and (3.40), the hydraulic boundary conditions result in,

$$-\kappa a_4 \eta \sqrt{s} B_0 I_1(\sqrt{s}) = 0 \quad (3.62)$$

$$-\kappa \eta [a_4 \beta_n B_n I_1(\beta_n) - a_2 \chi_n D_n I_1(\chi_n)] = 0 \quad (3.63)$$

$$-\kappa a_4 \eta \sqrt{s} A_0 \sinh(\sqrt{s}h) = 0 \quad (3.64)$$

$$-\kappa \eta [a_4 \gamma_m A_m \sinh(\gamma_m h) - a_2 \lambda_m C_m \sinh(\lambda_m h)] = 0 \quad (3.65)$$

Equations (3.45), (3.46), (3.49), (3.50), (3.54) and (3.55), together with Eqs. (3.58)-(3.61) for permeable (drained) surfaces or Eqs. (3.62)-(3.65) for impermeable (undrained) surfaces, constitute a system of linear equations of order $(3M + 3N) + 4$, which M and N are the total number of terms used in the Bessel and Fourier series expansion respectively, to determine the arbitrary functions $A_0, B_0, C_0, D_0, A_m, B_n, C_m, D_n, E_m$ and F_n ($m=1, 2, \dots, M; n=1, 2, \dots, N$).

3.4 Numerical Results and Discussion

The solution procedure described in the previous section is implemented into a computer program to determine all arbitrary functions appearing in the general solution of a poroelastic cylinder in the Laplace transform domain. Piessens (1975) conducted a review of numerical Laplace inversion schemes and found that the scheme proposed by Stehfest (1970) is very accurate for time-dependent problems. In the past, Stehfest's scheme has been widely used in a variety of poroelastic problems. For example, the plane strain solution of poroelastic cylinders (Cui and Abousleiman, 2001), interaction between an elastic circular plate and a multi-layered poroelastic medium (Senjuntichai and Sapsathiarn, 2006) and cylindrical cavity in a thermoporoelastic medium (Bai and Le, 2009) were studied by using Stehfest's scheme. According to Stehfest (1970), the time domain solution is given by

$$\phi(t) \approx \frac{\log 2}{t} \sum_{n=1}^{NT} \alpha_n \tilde{\phi}\left(\frac{n \ln 2}{t}\right) \quad (3.66)$$

where

$$\alpha_n = (-1)^{n+NT/2} \sum_{m=\lceil (n+1)/2 \rceil}^{\min(n, NT/2)} \frac{m^{N/2} (2m)!}{\left(\frac{N}{2} - m\right)! (m-1)! (n-m)! (2m-n)! m!} \quad (3.67)$$

In the above equations, $\tilde{\phi}$ denotes the Laplace transform of $\phi(t)$ and NT is even. It is found that time domain solutions for axisymmetrically-loaded poroelastic cylinders can be obtained accurately with $NT \geq 6$. Similar behavior was also observed in previous poroelastic problems (e.g., Senjuntichai and Sapsathiam 2006, and Bai and Le 2009). The convergence and numerical stability of the present solution scheme were investigated with respect to the total number of terms (M and N) used in the Fourier-Bessel series expansion. The solutions are found to be stable and converged when both M and $N \geq 30$.

The accuracy of present solution scheme is verified by comparing with the existing solutions for both elastic and poroelastic solid cylinders. Wei and Chau (2000) presented the stress distribution within an isotropic elastic solid cylinder of diameter $2a$ and height $2h$ under a double-punch test, in which two rigid circular punches of diameter $2b$ are applied at the top and bottom surfaces of the cylinder. The boundary conditions for a solid cylinder subjected to a double-punch test are given by,

$$\sigma_{rr}(1, z) = 0; \quad \sigma_{rz}(1, z) = 0 \quad \sigma_{rz}(r, \pm h) = 0 \quad (3.68)$$

$$\sigma_{zz}(r, \pm h) = -\frac{P}{2\pi b \sqrt{b^2 - r^2}}; \quad r < b \text{ otherwise } \sigma_{zz}(r, \pm h) = 0; \quad (3.69)$$

where P is the magnitude of the applied point force.

Figure 3.2(a) shows a comparison of the final solutions of non-dimensional tangential and vertical stresses along the axis of the cylinder from the present study with those given by Wei and Chau (2000) for $h/a=1$ and $b/a=0.1$ for different Poisson's ratios. Comparisons of tangential and vertical stresses along the cylinder axis are also presented in Fig. 3.2(b) for different sizes of the punch, b/a , with $\nu=0.1$ and $h/a=1$. Excellent agreement between the two solutions is noted. Note that the final solution is obtained from the present scheme by setting $ct/a^2=10^5$.

Cui and Abousleiman (2001) presented the plane strain solution for a solid poroelastic cylinder capped by a pair of rigid plates at both ends. The cylinder is subjected to a constant axial compressive force, $F(t)=F_0H(t)$ where $H(t)$ is the Heaviside step function, with no confining pressure. Comparisons between the present solutions and solutions given

by Cui and Abousleiman (2001) are respectively shown in Fig. 3.3(a) for nondimensional radial stress and pore pressure at the center of the cylinder and in Fig. 3.3(b) for radial displacement, vertical and tangential stresses at the boundary of the mid-plane. The material properties of Mexico Gulf shale were used with $\mu=760$ MPa; $B=0.90$; $\nu =0.22$; $\nu_u =0.46$ and $\kappa =5.00 \times 10^{-17}$ m⁴/Ns. Note that the average vertical stress used in the normalization is defined as $\sigma_0 = F_0 / \pi a^2$. The plane strain solution can be obtained from the present scheme by setting h/a to a large value ($h/a > 5.0$). Comparisons in Figs. 3.3(a) and 3.3(b) indicate very close agreement. The accuracy of the present solution is thus confirmed through independent comparisons corresponding to two limiting cases (ideal elastic and plane strain poroelastic cases).

Time-dependent behavior of solid cylinders shown in Fig. 3.4 is investigated next. Figure 3.4 shows a poroelastic cylinder ($B=0.90$, $\nu =0.20$, $\nu_u =0.40$) subjected to constant vertical pressure at both ends [$F_z(r,t) = f_0 H(t)$ in Eq. (3.38)] with zero radial pressure on the curved surface and fully permeable hydraulic boundary conditions on all surfaces. Figures 3.5(a), 3.5(b) and 3.5(c) show time histories of non-dimensional radial stress, vertical stress and pore pressure respectively at the center of a cylinder ($r/a = 0$ and $z/a = 0$) for different aspect ratios ($h/a = 0.5, 1.0, 1.5, 2.0$ and 3.0) under the loading shown in Fig. 3.4. Initially ($ct/a^2 < 10^{-5}$), radial stress at the center of cylinder is nearly zero, then increases quite rapidly during the period $0.01 < ct/a^2 < 0.1$ to about 5-10% of the applied vertical pressure depending on the aspect ratio (h/a) and thereafter diminishes very rapidly becoming almost zero for $ct/a^2 > 10$. The maximum radial stress value decreases with increasing aspect ratio but becomes independent of it for $h/a > 2$. Numerical results shown in Fig. 3.5(b) indicate that the initial vertical stress is equal to the applied pressure f_0 irrespective of the aspect ratio (h/a). Thereafter, it increases with time reaching its maximum value near $ct/a^2 = 0.1$ before decreasing to f_0 when $ct/a^2 > 1$. Maximum vertical stress is about 10% more than f_0 for longer cylinders but less than 2% increase is observed for a short cylinder (e.g., $h/a = 0.5$). Pore pressure at the centre of cylinder shows [Fig. 3.5(c)] less dependence on h/a compared to radial and vertical stresses, and the Mandel-Cryer effect is observed in the pore pressure evolution. Initially ($ct/a^2 < 10^{-4}$), pore pressure at the center is about 30% of the applied vertical pressure irrespective of the aspect ratio and then slightly increases with time to about 32-35% of the applied pressure. Pore pressure dissipates very rapidly after reaching its peak value and complete dissipation is observed for $ct/a^2 > 2$.

Time-histories of non-dimensional radial displacement, tangential (hoop) stress and vertical stress at the boundary of the cylinder mid-plane ($r/a=1$ and $z/a=0$) are presented in Figs. 3.6(a), 3.6(b) and 3.6(c) respectively for different aspect ratios. Radial displacement solutions and comparison with the ideal elastic case show that the initial and final normalized displacements are mainly controlled by the magnitude of undrained and drained Poisson's ratios respectively. Similar behavior was observed earlier by Rajapakse and Senjuntichai (1993) for a surface-loaded poroelastic half space. The initial value of the radial displacement is essentially independent of the aspect ratio and is equal to $\nu_u / 2(1 + \nu_u)$ whereas the final displacement is given by the same expression with ν_u being replaced by ν . In all results shown in Fig. 3.6, the final solutions are reached when $ct/a^2 > 2$. The influence of aspect ratio on the radial displacement is negligible if $h/a > 1.5$. Time histories of tangential stress [Fig. 3.6(b)] and vertical stress [Fig. 3.6(c)] also follow a trend that is qualitatively similar to the radial displacement. A notable feature in Fig. 3.6(b) is that tensile hoop stress is developed at the boundary of the mid-plane of a cylinder. Tensile hoop stresses may cause fracture and opening of pores, which could initiate cracks and failure. Most geomaterials have relatively small ultimate stress in tension and tensile tangential stresses could therefore initiate failure. The solution for tangential stress of a long cylinder can be obtained from the plane strain case given by Cui and Abousleiman (2001). It can be shown that tangential stress at the outer boundary ($r/a=1$) of a long cylinder can be expressed in the Laplace domain as

$$\frac{\bar{\sigma}_{\theta\theta}(1,0,s)}{f_0} = \frac{(\nu_u - \nu) \left[2s^{-1/2} I_1(\sqrt{s}) - I_0(\sqrt{s}) \right]}{s \left[(1 - \nu)(1 + \nu_u) I_0(\sqrt{s}) - 4s^{-1/2} (\nu_u - \nu) I_1(\sqrt{s}) \right]} \quad (3.70)$$

Tangential stress solutions shown in Fig. 3.6(b) indicate very close agreement with the plane strain solution given by Eq. (3.70) when $h/a > 2$. Initially, the maximum tensile stress is about 17% of f_0 and it is independent of the aspect ratio. Non-zero tangential stress is primarily due to the poroelastic effect as can be seen from Eq. (3.70) because it vanishes when ν_u is equal to ν . The final solution (as well as the ideal elastic solution) for tangential stress is zero when $ct/a^2 > 2$ for all aspect ratios. Vertical stress shown in Fig. 3.6(c) is compressive throughout its evolution. Initially ($ct/a^2 < 10^{-5}$), vertical stress at the boundary of the cylinder mid-plane is approximately 82% of the applied pressure f_0 irrespective of the aspect ratio. The final value is equal to f_0 and is attained when $ct/a^2 > 2$ for the aspect ratios considered in this study. It is also noted that vertical stress approaches the plain strain solution given by Cui and Abousleiman (2001) when $h/a > 2$.

Figures 3.7(a) and 3.7(b) show profiles of non-dimensional vertical displacement and vertical stress along the z -axis respectively. Vertical displacement is obviously zero at the center of the cylinder due to symmetry consideration, and increases almost linearly along the length reaching its maximum value at the cylinder ends. Average vertical strain is almost independent of the aspect ratio and this makes the displacement profiles along the length of each cylinder nearly coinciding with each other in Fig. 3.7(a). A slight increase of displacement ($\sim 10\%$) with time is noted. As expected, non-dimensional vertical stress shown in Fig. 3.7(b) is compressive at all times and the maximum vertical stress is noted at the center of the cylinder. The maximum stress shown in Fig. 3.7(b) is about 10% higher than the corresponding elastic solution for cylinders with $h/a = 1.5$ and 3.0, whereas for a short cylinder ($h/a = 0.5$), it is about 2% higher than the elastic solution. The steady-state is reached when $ct/a^2 > 10$ except for a cylinder with $h/a = 0.5$, in which the final solution is attained relatively quickly ($ct/a^2 > 1$).

The profiles of non-dimensional pore pressure and fluid discharge in the vertical direction along the cylinder axis are presented in Figs. 3.7(c) and 3.7(d) respectively. Initially ($ct/a^2 < 10^{-2}$), the excess pore pressure along the cylinder axis is about 32% of the applied vertical pressure except at the end surfaces where it is zero due to the drained boundary condition. At $ct/a^2 = 0.1$, the pore pressure in a short cylinder ($h/a = 0.5$) decreases from the initial value, whereas for long cylinders ($h/a = 1.5$ and 3.0), pore pressure experiences a very small increase from the initial values except near the cylinder ends due to the boundary condition. Pore pressure is completely dissipated in all cases when $ct/a^2 > 10$. Numerical results of the fluid discharge profiles in Fig. 3.7(d) indicate that initially ($ct/a^2 = 10^{-2}$) the discharge is observed only near the end surface due to the pore pressure gradient created at the ends [Fig. 3.7c]. As the pore pressure gradient propagates inward into the cylinder more discharge occurs along the length but the maximum discharge always occurs at the top and bottom ends. Fluid discharge along the length becomes negligible when $ct/a^2 > 10$.

Profiles of non-dimensional tangential stress on the outer surface along the length ($r/a = 1$) and at the mid-height along the radial direction ($z/a = 0$) are shown in Figs. 3.8(a) and 3.8(b) respectively for different times and aspect ratios. Numerical results in Fig. 3.8(a) indicate that tangential stress remains tensile along the cylinder wall. Initially, it is nearly constant within the middle of the cylinder except for short cylinders but shows a drop near the cylinder ends in all cases. Its magnitude decreases as time progresses and poroelastic effects dissipate. As expected, tangential stress at the mid-plane approaches the plane strain solution of Cui and Abousleiman (2001) in the case of long cylinders. The final solution is attained

when $ct/a^2 > 10$ for all cylinders. Figure 3.8(b) shows that tangential stress varies significantly in the radial direction at the mid-plane. It is generally compressive at early times ($ct/a^2 = 0.005$) except in the vicinity of the cylinder wall. The tensile stress region gradually expands with time and tangential stress at all points becomes negligible when $ct/a^2 > 10$.

Uni-axial and tri-axial compression tests are commonly employed to determine the strength and stress-strain relationship of soils and rocks. Unlike a uni-axial test, cylindrical specimens subjected to tri-axial tests have lateral confining pressure in addition to the vertical end load. Consider a poroelastic cylinder ($B=0.90$, $\nu=0.20$ and $\nu_u=0.40$) capped with rigid plates at its both ends subjected to confining pressure (p_0) at the initial state and vertical loading applied to the ends after pore pressure due to confining pressure is totally dissipated. This problem can be considered as a theoretical model of a tri-axial compression test under stroke control of a jacketed cylindrical specimen, which is covered by a rubber membrane along the cylindrical surface, and the fluid is drained at its both ends. The vertical loading is applied such that the vertical displacements at both cylinder ends are controlled at a constant rate u_0 , i.e. $u_z(r, \pm h, t) = u_0 t$. The surface hydraulic boundary conditions are permeable at the horizontal end surfaces and impermeable along the curved surface. The test condition can be separated into two states: the initial state from a pure confining pressure and the final state of applied vertical loading. The total solution for the poroelastic field can be obtained by superposition of the solutions for pure confining pressure and pure applied vertical loading.

Figures 3.9(a) and 3.9(b) show the geometry of problems considered in the initial and final states respectively. The boundary conditions for a cylinder subjected to pure confining pressure in the initial state [Fig. 3.9(a)] can be expressed as,

$$\bar{\sigma}_{rr}(1, z, s) = -\frac{p_0}{s}; \quad \bar{\sigma}_{rz}(1, z, s) = 0 \quad \bar{q}_r(1, z, s) = 0 \quad (3.71)$$

at the curved surface and

$$\int_0^1 2\pi \bar{\sigma}_{zz}(r, \pm h, s) dr = -\frac{\pi p_0}{s} \quad \bar{\sigma}_{rz}(r, \pm h, s) = 0 \quad \bar{p}(r, \pm h, s) = 0 \quad (3.72)$$

at the end surfaces.

The boundary conditions for the final state of a cylinder subjected to vertical loading under zero confining pressure [Fig. 3.9(b)] can be expressed as,

$$\bar{\sigma}_{rr}(1, z, s) = 0; \quad \bar{\sigma}_{rz}(1, z, s) = 0 \quad \bar{q}_r(1, z, s) = 0 \quad (3.73)$$

at the curved surface and

$$\bar{u}_z(r, \pm h, s) = -\frac{u_0}{s^2} \quad \bar{\sigma}_{rz}(r, \pm h, s) = 0 \quad \bar{p}(r, \pm h, s) = 0 \quad (3.74)$$

at the end surfaces.

The profiles of non-dimensional excess pore pressure along the vertical axis of the cylinder due to confining pressure are presented in Fig. 3.10 for different times and aspect ratios. Excess pore pressure is zero at the top surface due to the boundary condition and nearly constant at the mid-plane of the cylinder for $h/a > 1.5$. It is non-uniform for shorter cylinders with the maximum value observed at the mid-plane of the cylinder. Initial excess pore pressure in the middle of the cylinder is approximately 90% of the applied confining pressure for most cases. Note that the 1-D solution for the excess pore pressure in the initial state can be obtained by solving Eqs. (3.2) and (3.3) and it is also shown in Fig. 3.10. The 1-D solution can be expressed in the Laplace domain as,

$$\frac{\tilde{p}(z, s)}{p_0} = -\frac{1}{s} \left[\frac{B(1-\nu)(1+\nu_u)s^{1/2}h [\cosh(\sqrt{s}z) - \cosh(\sqrt{s}h)]}{2(\nu_u - \nu)\sinh(\sqrt{s}h) + (1-\nu)(1+\nu_u)s^{1/2}h \cosh(\sqrt{s}h)} \right] \quad (3.75)$$

Comparison between the finite cylinder solution and the 1-D solution indicates that both solutions show similar trends with time and vertical distance but the 1-D solution generally has lower pore pressure. The difference between the two solutions reduces with increasing h/a but shorter cylinders show substantial differences at intermediate times.

Figures 3.11(a), 3.11(b), 3.11(c) and 3.11(d) show time histories of non-dimensional radial displacement, tangential stress, vertical stress and excess pore pressure at the boundary of the mid-plane ($r/a=1$ and $z/a=0$) respectively for the loading case defined by Eqs. (3.73) and (3.74). All solutions are negligible when $ct/a^2 < 0.01$ due to the nature of applied loading. Radial displacement rapidly increases with time but no asymptotic solution is expected due to the fact that the applied vertical displacement at the ends linearly increases with time. Radial displacement is higher for shorter cylinders as the radial strain is larger. Numerical results for tangential stress in Fig. 3.11(b) indicate that it gradually increases as time progresses until the final value is reached when $ct/a^2 > 10$. Tensile tangential stress is noted at the boundary except in the case of short cylinder ($h/a=0.5$) where only compressive

tangential stress is observed at all time instants. This is due to the fact that the tangential stress depends on radial displacement, dilatation (ε) and pore pressure [see Eq. (3.6)]. Under the stroke-control loading [Eq. (3.74)], it is found that the volume reduction in a short cylinder ($h/a < 1$) is higher than its lateral displacement resulting in compressive tangential stress being observed. For cylinders with $h/a > 1$, the tensile tangential stress at the boundary gradually increases as the cylinder becomes longer before approaching the 1-D solution, which is equal to zero, when $h/a > 2$. Note that the tangential stress under this loading case is very small compared to vertical stress and pore pressure, and it can be neglected for all practical purposes. Numerical results presented in Fig. 3.11(c) show that the general trend of vertical stress histories is similar to that observed for the radial displacement histories in Fig. 3.11(a). Vertical stress rapidly increases with time when $ct/a^2 > 1.0$, and no final asymptotic solution exists as the vertical displacement continuously increases with time. It is obviously compressive at all times and its magnitude decreases with the aspect ratio. Time histories of pore pressure indicate that pore pressure has a steady-state value in this case as the ends are fully drained although the cylindrical boundary is impermeable and applied displacement continues to increase. The steady-state for pore pressure is reached quicker with decreasing the aspect ratio as the fluid has lesser distance to reach the drained ends.

Figures 3.12(a), 3.12(b), 3.12(c) and 3.12(d) show the distribution of non-dimensional vertical displacement, radial stress, pore pressure and vertical discharge respectively along the z -axis for different times and aspect ratios. All field variables are zero at $t = 0$ due to the nature of the displacement controlled loading. The vertical displacement profiles in Fig. 3.12(a) show linear variation along the vertical axis from zero at $z/a = 0$ to the maximum value at the cylinder ends which can be expressed as $u_z(0, z, t) = u_0 tz / h$. This behavior is a consequence of the displacement-controlled loading. Radial stress in Fig. 3.12(b) shows considerable time dependency and variation along the length in its evolution with both compressive and tensile stresses existing along the length. In most cases, radial stress near the ends is tensile but becomes compressive in the interior region. Compressive radial stress increases with decreasing aspect ratio whereas the opposite is true for maximum tensile radial stress. Pore pressure profiles shown in Fig. 3.12(c) indicate that it increases with increasing time and aspect ratio. Maximum pore pressure is observed at the centre of the cylinder for all aspect ratios. Fluid discharge in the vertical direction is always highest at the ends as shown in Fig 3.12(d) and is zero at the centre due to symmetry consideration. The steady-state solution of the fluid discharge shows a linear variation along the vertical axis. It should be noted that vertical stress along the z -axis is constant and can be expressed explicitly as a linear function of time of the form, $\sigma_{zz}(0, z, t) = 2\mu(1 + \nu)tu_0 / h$.

3.5 Conclusion

It is shown in this chapter that coupled poroelastic governing equations for axisymmetric deformations of a finite solid cylinder can be solved analytically by employing Laplace transforms with respect to time and Fourier-Bessel series expansions in the vertical and radial directions respectively. Applicability of the general solution is demonstrated by solving two boundary-value problems. Convergence and stability of the series solution and the numerical Laplace transform is confirmed by excellent agreement between the present solution and those in the literature for the limiting cases of an ideal elastic finite cylinder and plane strain poroelastic cylinder. Selected numerical results show complex 3-D behavior and end effects are significant for cylinders with aspect ratio greater than three. The material dependence of the initial and final solutions is primarily controlled by the undrained and drained Poisson's ratios respectively. Mandel-Cryer effect is also observed for the present class of problems. Solutions for stroke-control tests show that asymptotic solutions for tangential and radial stresses, and pore pressure exist.



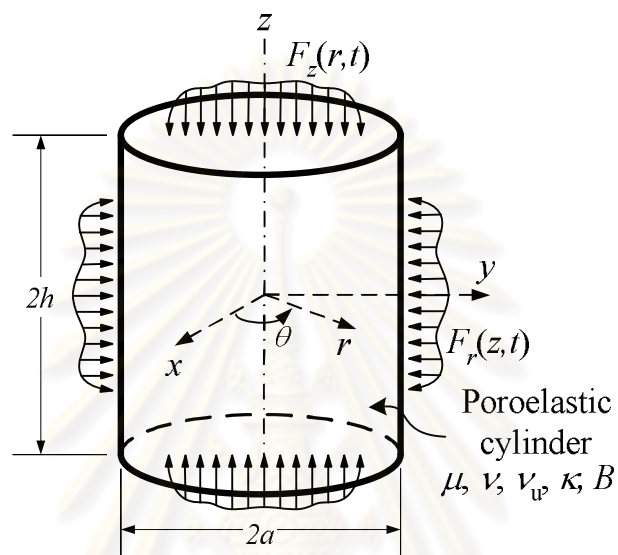


Figure 3.1 Finite poroelastic cylinder under axisymmetric loading.

ศูนย์วิทยทรัพยากร
จุฬาลงกรณ์มหาวิทยาลัย

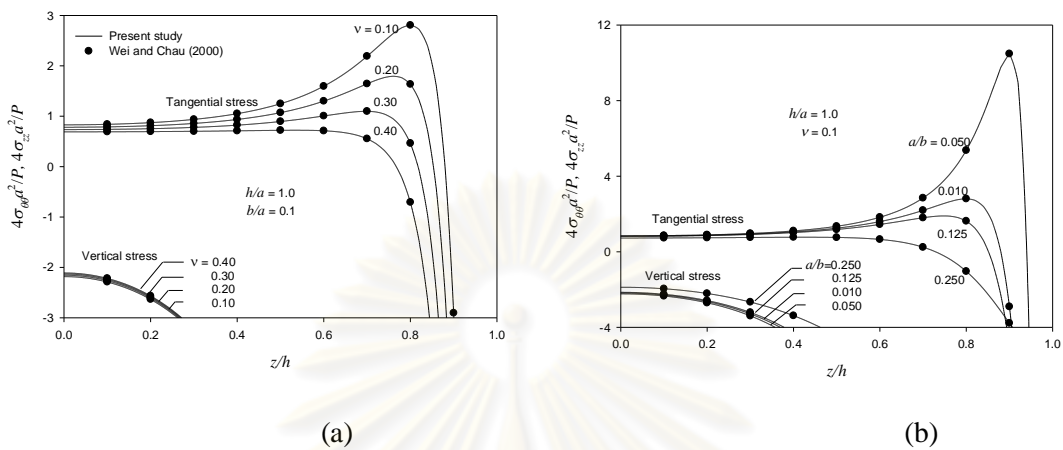


Figure 3.2 Comparison with existing solutions for elastic cylinders.

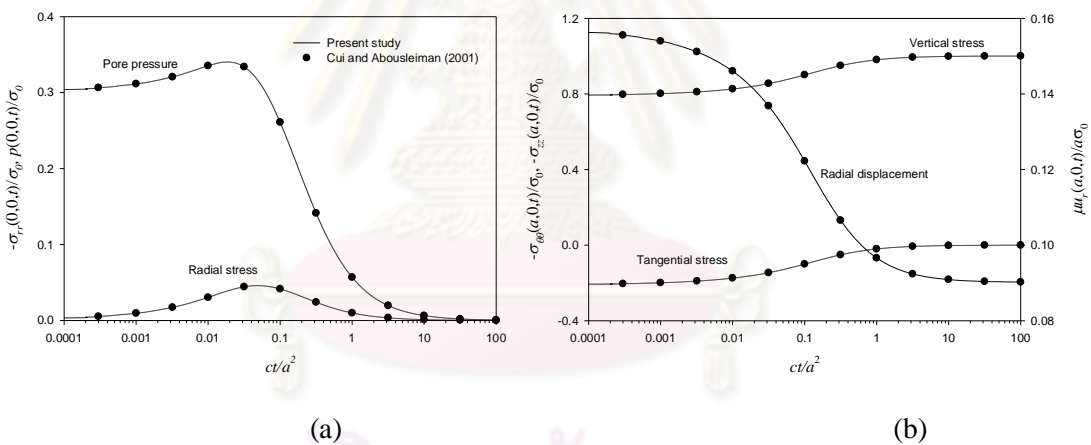


Figure 3.3 Comparison with existing solutions for poroelastic cylinders under plane strain condition.

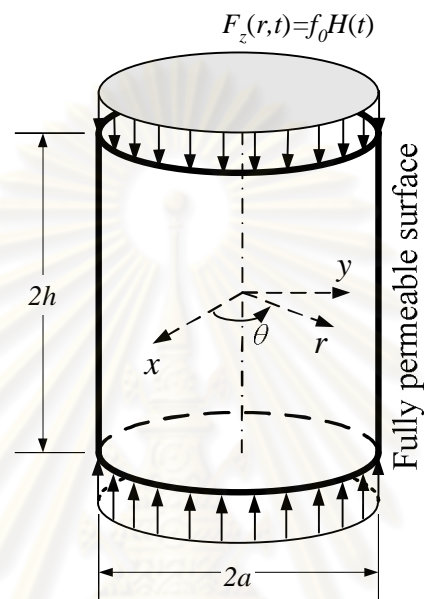
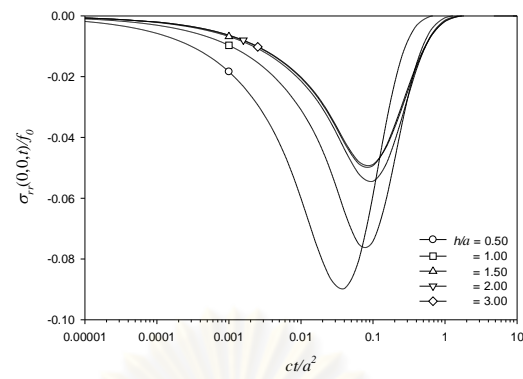
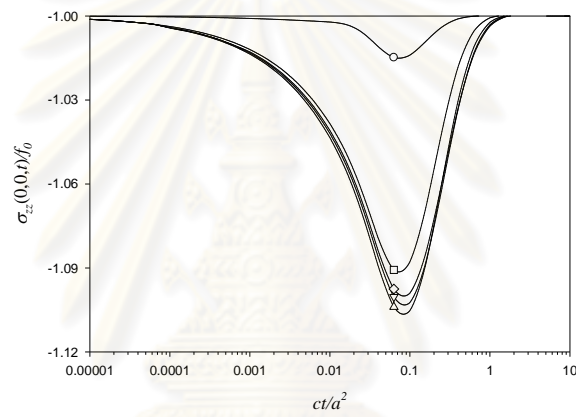


Figure 3.4 Poroelastic cylinder ($B = 0.90, \nu = 0.20, \nu_u = 0.40$) subjected to axisymmetric vertical loading for numerical results in Figs. 3.5-3.8.

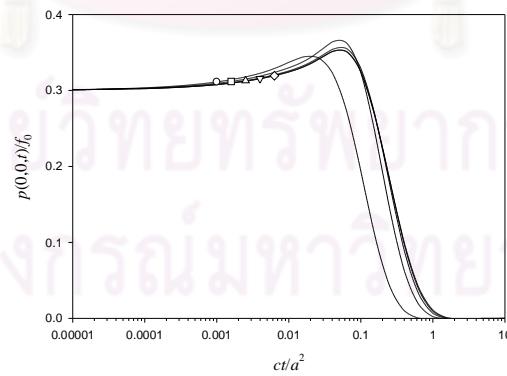
ศูนย์วิทยทรัพยากร
จุฬาลงกรณ์มหาวิทยาลัย



(a)

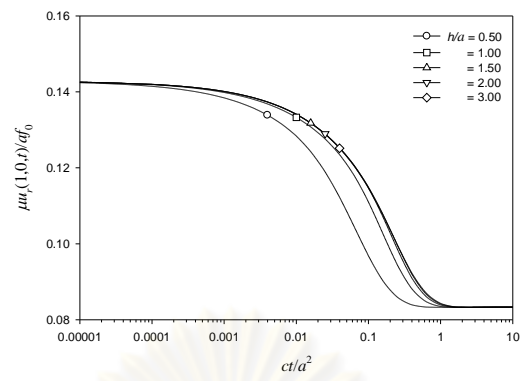


(b)

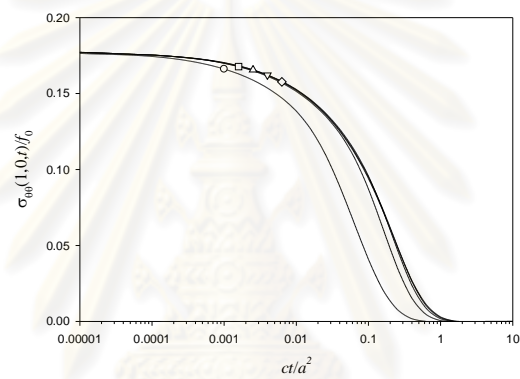


(c)

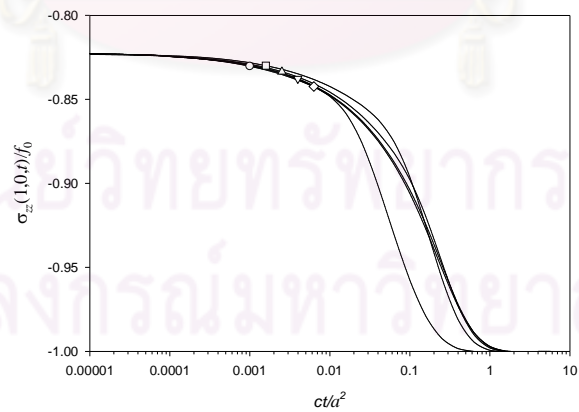
Figure 3.5 Time histories of (a) radial stress; (b) vertical stress and (c) excess pore pressure at the center of cylinder for different values of h/a .



(a)



(b)



(c)

Figure 3.6 Time histories of (a) radial displacement; (b) tangential stress; and (c) vertical stress at the boundary of the mid-plane of cylinder for different values of h/a .

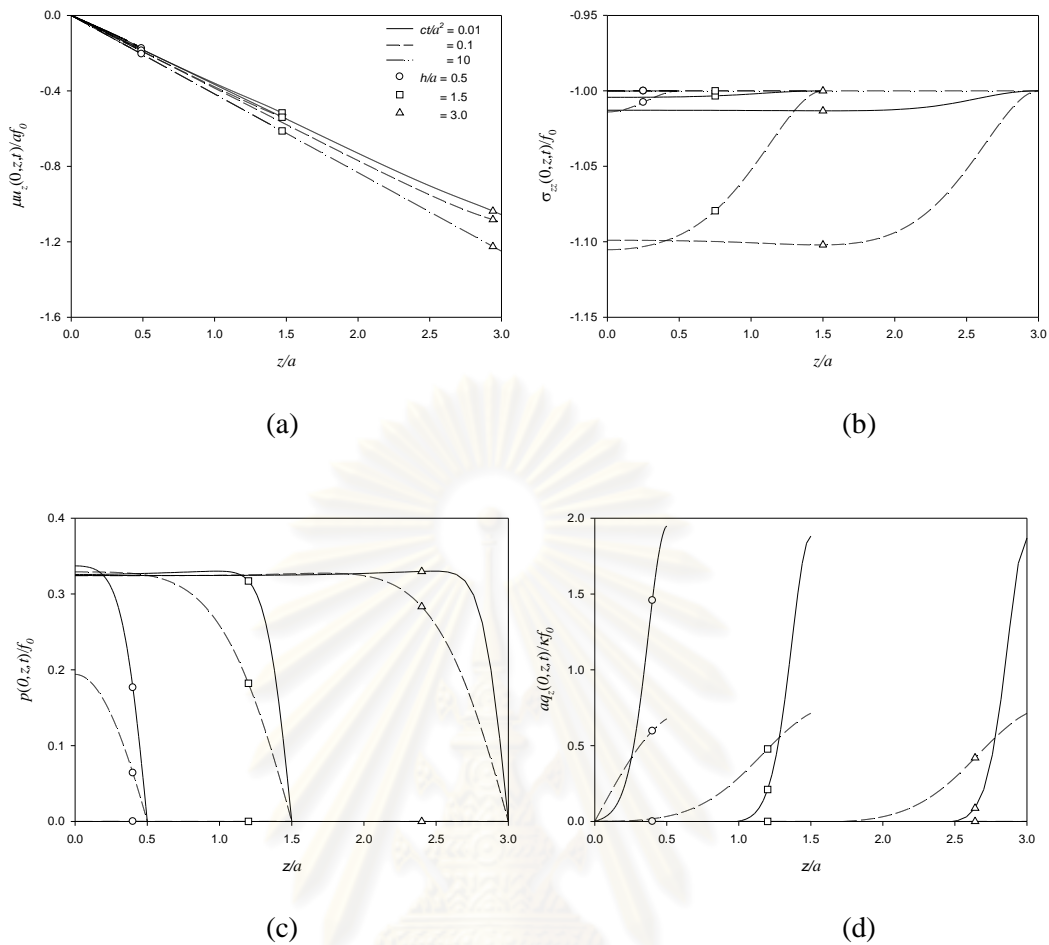


Figure 3.7 Profiles of (a) vertical displacement; (b) axial stress; (c) excess pore pressure; and (d) vertical discharge along the z -axis of cylinder for different ratios of h/a .

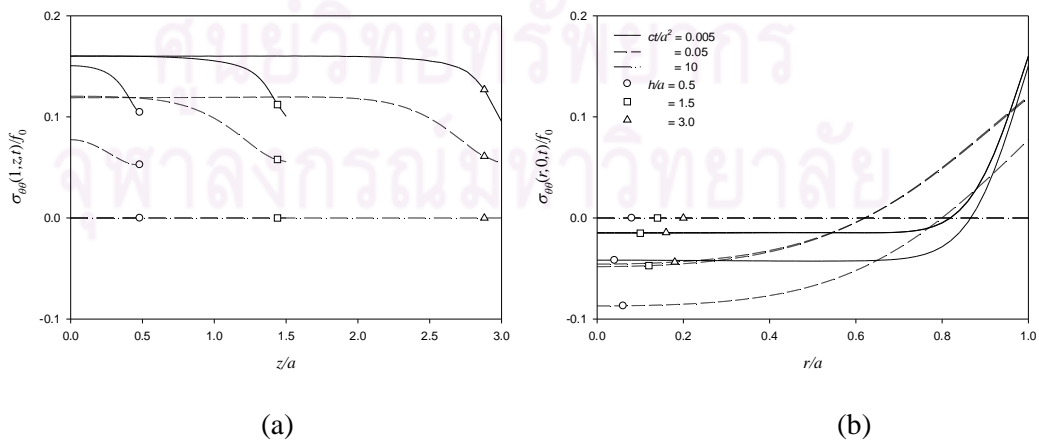


Figure 3.8 Profiles of tangential stress (a) along the length of the cylinder ($r/a=1$) and (b) at the mid-height ($z/a=0$)

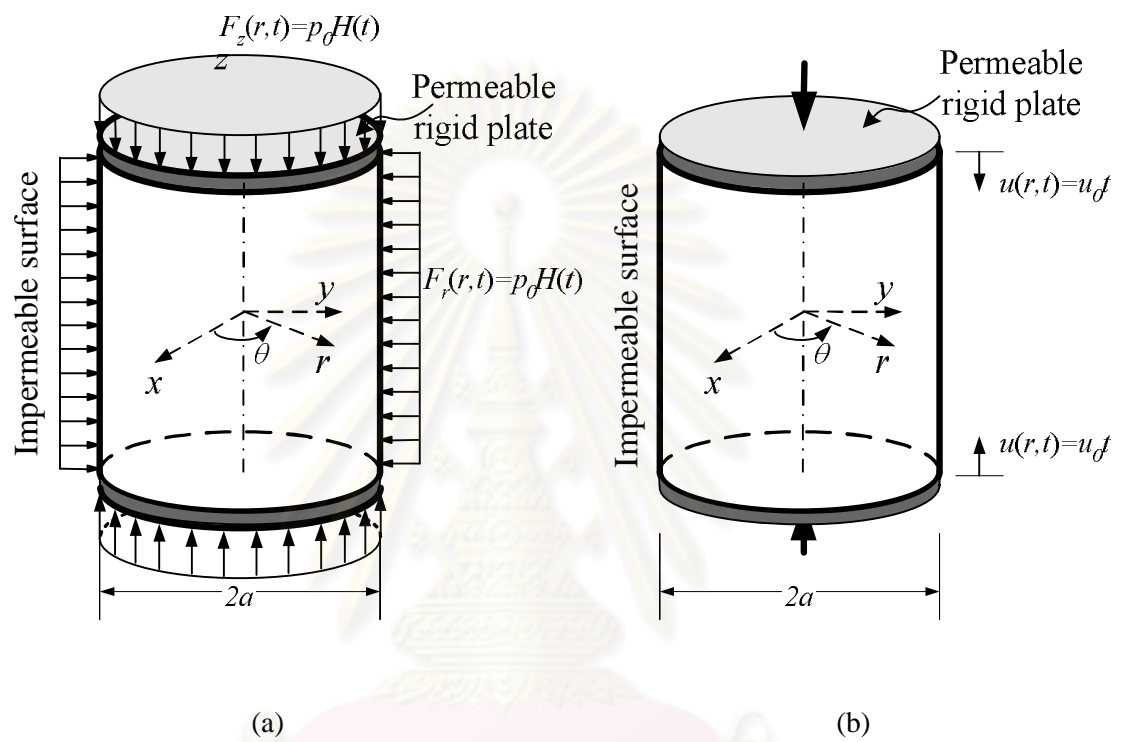


Figure 3.9 Poroelastic cylinder ($B = 0.90, \nu = 0.20, \nu_u = 0.40$) capped with rigid plates subjected to (a) confining pressure and (b) vertical loading.

ศูนย์วิทยทรัพยากร
จุฬาลงกรณ์มหาวิทยาลัย

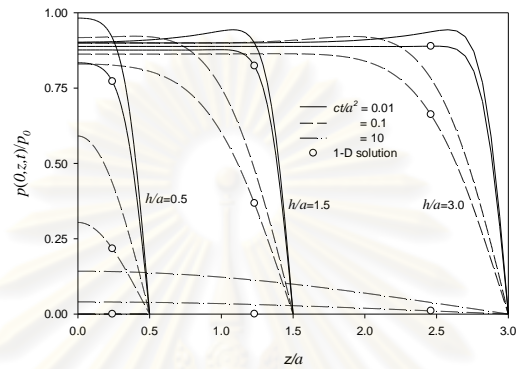


Figure 3.10 Profiles of excess pore pressure along the z -axis of cylinder [Fig. 3.9(a)] for different values of h/a .

ศูนย์วิทยทรัพยากร
จุฬาลงกรณ์มหาวิทยาลัย

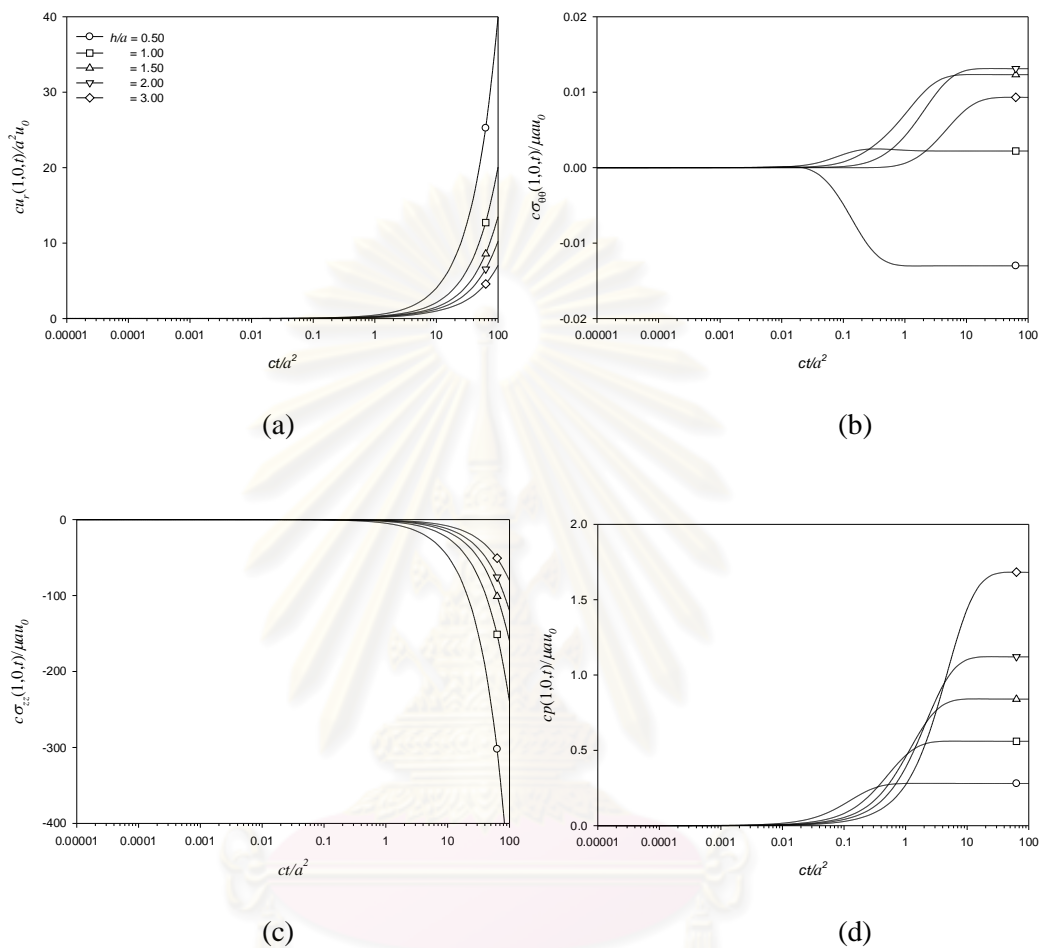


Figure 3.11 Time histories of (a) radial displacement, (b) tangential stress, (c) axial stress; and (d) excess pore pressure at the boundary of the mid-plane of cylinder [Fig. 3.9(b)] for different values of h/a .

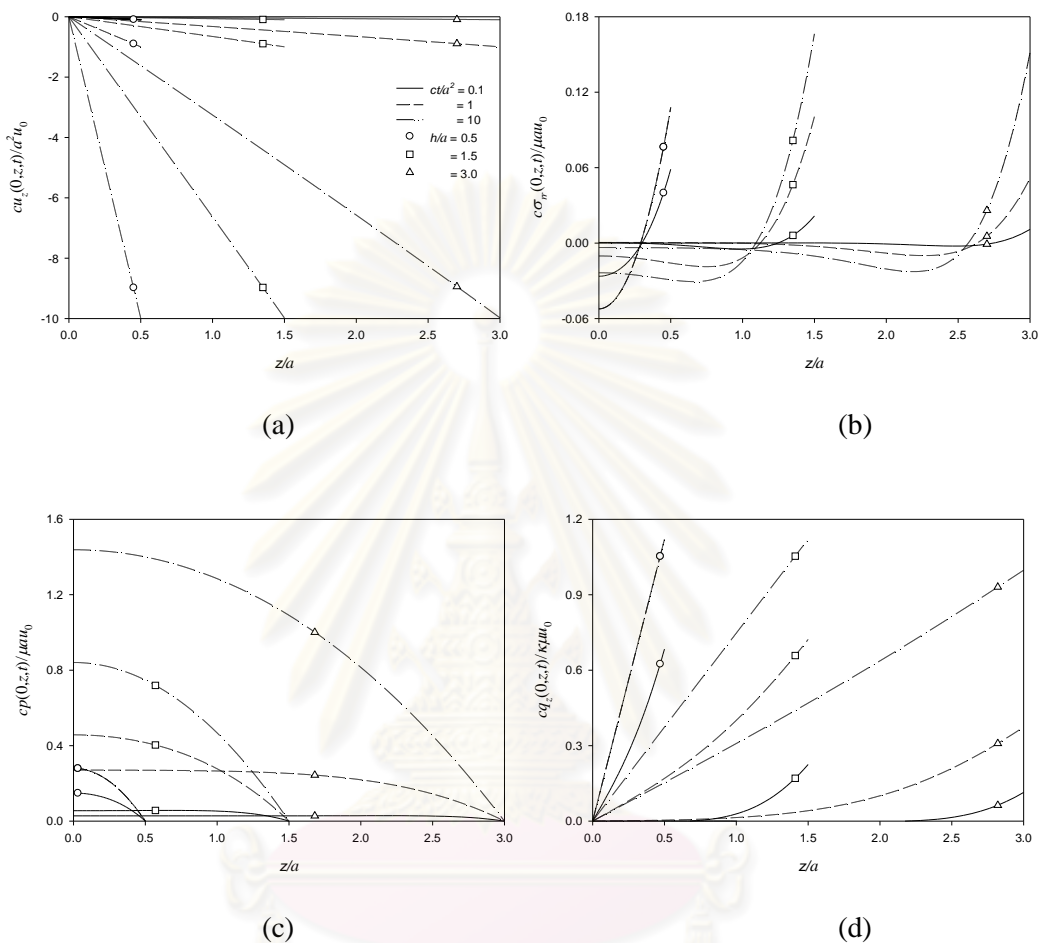


Figure 3.12 Profiles of (a) vertical displacement; (b) radial stress; (c) excess pore pressure; and (d) vertical discharge along the z -axis of cylinder [Fig. 3.9(b)] for different values of h/a .

CHAPTER IV

QUASI-STATIC RESPONSE OF BOREHOLE WITH DISTURBED ZONE

4.1 General

In this chapter, time-dependent response of a cylindrical borehole in a poroelastic medium with consideration of excavation disturbed zone is considered. The general solutions for axisymmetric deformations are derived by employing Laplace and Fourier transforms with respect to time and the vertical coordinate respectively. Shear modulus and permeability coefficient are assumed to be non-homogenous in the disturbed zone. The general solutions are employed to formulate boundary value problems corresponding to a borehole subjected to axisymmetric loading applied at its surface, and contact problems involving a borehole containing a rigid cylinder. Selected numerical results are presented for displacement, stress, pore pressure and fluid discharge to portray the influence of poroelastic effects and the excavation disturbed zone on the borehole response.

4.2 General Solution

Consider an infinite cylindrical borehole of radius a in a poroelastic medium with an excavation disturbed zone of length d subjected to axisymmetric loading as shown in Fig. 4.1. The governing equations in the previous chapter for a poroelastic material undergoing axisymmetric deformation in Eqs. (3.1)-(3.3) can also be employed for this problem. The general solutions are derived by applying Laplace and Fourier transforms with respect to time and the vertical coordinate respectively. The Laplace transform and its inverse transform are given by Eqs. (3.11) and (3.12). In addition, the Fourier transform of a function $\bar{f}(r, z, s)$ with respect to the vertical coordinate and the inverse relationship are given by (Sneddon 1951)

$$\tilde{f}(r, \xi, s) = \frac{1}{2\pi} \int_{-\infty}^{\infty} \bar{f}(r, z, s) e^{i\xi z} dz \quad (4.1)$$

$$\bar{f}(r, z, s) = \int_{-\infty}^{\infty} \tilde{f}(r, \xi, s) e^{-i\xi z} d\xi \quad (4.2)$$

where ξ is the Fourier transform parameter.

In all subsequent manipulations, a superposed bar ($\bar{\quad}$) denotes the Laplace transform of a function with respect to time coordinate and a tilde ($\tilde{\quad}$) denotes the Fourier transform with respect to the vertical coordinate of the Laplace transform of that function. It is convenient to nondimensionalize all quantities including the coordinates with respect to the length and time by selecting the radius of the borehole “ a ” as a unit length, and “ a^2 / c ” as a unit of time respectively. All variables will be replaced by appropriate nondimensional variables, but the previous notations will be used for convenience.

Equation (3.3) in the previous chapter can be solved directly by applying Laplace and Fourier transforms with respect to time and the vertical coordinate respectively. The resulting solution can be expressed as,

$$\tilde{\xi} = AI_0(\beta r) + BK_0(\beta r) \quad (4.3)$$

where A and B are arbitrary functions, and

$$\beta = \sqrt{(\xi^2 + s)} \quad (4.4)$$

In addition, I_n and K_n are modified Bessel functions of the first and second kinds respectively of the n th order (Watson 1944).

By applying Laplace and Fourier transforms to Eq. (3.16) together with the substituting Eq. (4.3), the following solution can be obtained,

$$\tilde{\varepsilon} = 2|\xi|(1 - 2\nu_u) [CI_0(|\xi|r) + DK_0(|\xi|r)] + \eta [AI_0(\beta r) + BK_0(\beta r)] \quad (4.5)$$

where C and D are arbitrary functions.

Next, the application of Laplace and Fourier transforms in Eq. (3.2) and the substitution of Eqs. (4.3) and (4.5) result in the following general solution for the vertical displacement.

$$\begin{aligned} \tilde{u}_z = & i\xi\lambda s^{-1} [AI_0(\beta r) + BK_0(\beta r)] - i\xi r [CI_1(|\xi|r) - DK_1(|\xi|r)] \\ & + |\xi| [EI_0(|\xi|r) + FK_0(|\xi|r)] \end{aligned} \quad (4.6)$$

where E and F are arbitrary functions.

Thereafter, the following general solutions for radial displacement, stresses and pore pressure in the Laplace-Fourier domain can be obtained by using Eqs. (3.1), (3.5)-(3.9) together with Eqs. (4.3), (4.5) and (4.6) as follows

$$\begin{aligned}\tilde{u}_r &= \eta\beta s^{-1}[AI_1(\beta r) - BK_1(\beta r)] + 2(1 - 2\nu_u)[CI_1(|\xi|r) - DK_1(|\xi|r)] \\ &\quad - |\xi|r[CI_2(|\xi|r) + DK_2(|\xi|r)] - i\xi[GI_1(|\xi|r) - HK_1(|\xi|r)]\end{aligned}\quad (4.7)$$

$$\begin{aligned}\frac{\tilde{\sigma}_{rr}}{2\mu} &= A\eta[\xi^2 s^{-1}I_0(\beta r) - \beta(sr)^{-1}I_1(\beta r)] + B\lambda[\xi^2 s^{-1}K_0(\beta r) + \beta(sr)^{-1}K_1(\beta r)] \\ &\quad + C\{2(1 - \nu_u)|\xi|I_0(|\xi|r) - 2(1 - 2\nu_u)r^{-1}I_1(|\xi|r) + |\xi|I_2(|\xi|r) - \xi^2 rI_1(|\xi|r)\} \\ &\quad + D\{2(1 - \nu_u)|\xi|K_0(|\xi|r) + 2(1 - 2\nu_u)r^{-1}K_1(|\xi|r) + |\xi|K_2(|\xi|r) + \xi^2 rK_1(|\xi|r)\} \\ &\quad - i\xi G[|\xi|I_0(|\xi|r) - r^{-1}I_1(|\xi|r)] - i\xi H[|\xi|K_0(|\xi|r) + r^{-1}K_1(|\xi|r)]\end{aligned}\quad (4.8)$$

$$\begin{aligned}\frac{\tilde{\sigma}_{zz}}{2\mu} &= -\eta\beta^2 s^{-1}[AI_0(\beta r) + BK_0(\beta r)] + i\xi|\xi|[GI_0(|\xi|r) + HK_0(|\xi|r)] \\ &\quad + C|\xi|[2\nu_u I_0(|\xi|r) + |\xi|rI_1(|\xi|r)] + D|\xi|[2\nu_u K_0(|\xi|r) - |\xi|rI_1(|\xi|r)]\end{aligned}\quad (4.9)$$

$$\begin{aligned}\frac{\tilde{\sigma}_{\theta\theta}}{2\mu} &= \eta A[\beta(sr)^{-1}I_1(\beta r) - I_0(\beta r)] - \eta B[\beta(sr)^{-1}K_1(\beta r) + K_0(\beta r)] \\ &\quad + C[2(1 - 2\nu_u)r^{-1}I_1(|\xi|r) - |\xi|I_2(|\xi|r) + 2\nu_u|\xi|I_0(|\xi|r)] \\ &\quad + D[-2(1 - 2\nu_u)r^{-1}K_1(|\xi|r) - |\xi|K_2(|\xi|r) + 2\nu_u|\xi|K_0(|\xi|r)] \\ &\quad - i\xi r^{-1}[GI_1(|\xi|r) - HK_1(|\xi|r)]\end{aligned}\quad (4.10)$$

$$\begin{aligned}\frac{\tilde{\sigma}_{rz}}{2\mu} &= i\xi\eta\beta s^{-1}[AI_1(\beta r) - BK_1(\beta r)] + \xi^2[GI_1(|\xi|r) - HK_1(|\xi|r)] \\ &\quad - i\xi C[2\nu_u I_1(|\xi|r) + |\xi|rI_2(|\xi|r)] + i\xi D[2\nu_u K_1(|\xi|r) - |\xi|rK_2(|\xi|r)]\end{aligned}\quad (4.11)$$

$$\begin{aligned}\frac{\tilde{p}}{2\mu} &= \frac{B^2(1 + \nu_u)^2(1 - \nu)}{9(1 - \nu_u)(\nu_u - \nu)}[AI_0(\beta r) + BK_0(\beta r)] \\ &\quad - \frac{2B|\xi|(1 + \nu_u)}{3}[CI_0(|\xi|r) + DK_0(|\xi|r)]\end{aligned}\quad (4.12)$$

It can be shown that the general solutions for axisymmetric deformations of a poroelastic medium in the Laplace-Fourier transform domain as shown in Eqs. (4.6)-(4.12) can be expressed in the following matrix form.

$$\mathbf{u}(r, \xi, s) = \mathbf{R}(r, \xi, s)\mathbf{C}(\xi, s) \quad (4.13)$$

$$\mathbf{f}(r, \xi, s) = \mathbf{S}(r, \xi, s)\mathbf{C}(\xi, s) \quad (4.14)$$

where

$$\mathbf{u}(r, \xi, s) = [\tilde{u}_r \quad \tilde{u}_z \quad \tilde{p}]^T; \quad (4.15)$$

$$\mathbf{f}(r, \xi, s) = [\tilde{\sigma}_{rr} \quad \tilde{\sigma}_{rz} \quad \tilde{w}_r]^T \quad (4.16)$$

$$\text{and } \mathbf{C}(\xi, s) = [A \quad B \quad C \quad D \quad E \quad F]^T \quad (4.17)$$

The matrices \mathbf{R} and \mathbf{S} are defined in Appendix B. The arbitrary functions, $A(\xi, s)$ to $F(\xi, s)$ in $\mathbf{C}(\xi, s)$ are to be determined by employing appropriate boundary and/or continuity conditions. In the ensuing section, the above general solutions are employed to establish a stiffness matrix scheme to study time-dependent response of a borehole in a poroelastic medium with an excavation disturbed zone.

4.3 Borehole in Excavation Disturbed Zone

Naturally, a primary factor affecting the soil/rock properties around a borehole is an excavation process. The soil/rock zone where the properties and conditions have been changed is known as an excavation disturbed zone (EDZ). The mechanical properties of the EDZ can be adjusted based on laboratory and in situ tests. The shear modulus of the EDZ is normally reduced from its original value before excavation. On the contrary, the inflow in the EDZ is larger than that of the undisturbed zone (Lai et al. 2006 and Kwon et al. 2009). This is implied that the permeability coefficient then increases from the original value in the EDZ. Consider a cylindrical borehole with the EDZ of a length d as shown in Fig. 4.1. It is assumed that the shear modulus and permeability coefficient in the EDZ linearly vary with the radial distance r in the following manners.

$$\mu(r) = \mu_0 [m_1(r - a - d) + 1] \quad (4.18)$$

$$\text{and } \kappa(r) = \kappa_0 [m_2(a + d - r) + 1] \quad (4.19)$$

where μ_0 and κ_0 denote the original values of the shear modulus and the permeability coefficient respectively before excavation. m_1 and m_2 are non-negative constants representing the degree of disturbance due to the drilling process in shear modulus and permeability coefficient respectively. The poroelastic medium in Fig. 4.1 is then separated into two zones, i.e. the disturbed zone ($a \leq r < d$) and the undisturbed zone ($r > d$). To incorporate the influence of excavation disturbed zone, the EDZ is discretized into a total of N_a infinitely long tubular layers with small thickness. Each discretized layer is homogeneous and governed by Biot's theory of poroelasticity. The following relationship can be established by using Eqs. (4.13) and (4.14) for the n^{th} layer.

$$\mathbf{F}^{(n)} = \mathbf{K}^{(n)} \mathbf{U}^{(n)} \quad (4.20)$$

where $\mathbf{K}^{(n)}$ is an exact stiffness matrix in the Laplace-Fourier transform space describing the relationship between the generalized displacement vector $\mathbf{U}^{(n)}$ and the force vector $\mathbf{F}^{(n)}$ for the n^{th} layer, in which

$$\mathbf{U}^{(n)} = \left[\mathbf{u}^{(n)}(r_n, \xi, s) \quad \mathbf{u}^{(n)}(r_{n+1}, \xi, s) \right]^T \quad (4.21)$$

$$\mathbf{F}^{(n)} = \left[-\mathbf{f}^{(n)}(r_n, \xi, s) \quad \mathbf{f}^{(n)}(r_{n+1}, \xi, s) \right]^T \quad (4.22)$$

In Eqs. (4.21) and (4.22), $\mathbf{U}^{(n)}$ is a column vector of generalized displacements of the n^{th} layer whose elements are related to the Laplace-Fourier transform of displacements and pore pressure of the inner ($r = r_n$) and outer ($r = r_{n+1}$) surfaces of the n^{th} layer; $\mathbf{F}^{(n)}$ is a column vector of generalized forces whose elements are related to the Laplace-Fourier transform of traction and fluid displacement of the inner and outer surfaces of the n^{th} layer. In addition, the matrices $\mathbf{u}^{(n)}$ and $\mathbf{f}^{(n)}$ are identical to \mathbf{u} and \mathbf{f} given by Eqs. (4.15) and (4.16) respectively, except that the material properties of the n^{th} layer and employed with $r = r_n$ or $r = r_{n+1}$.

Similarly, the stiffness matrix $\mathbf{K}^{(N+1)}$ for the undisturbed zone ($r > d$ in Fig. 4.1) can be obtained by establishing a relationship between the generalized displacement vector $\mathbf{U}^{(N+1)}$ and the force vector $\mathbf{F}^{(N+1)}$ as

$$\mathbf{K}^{(N+1)} = \mathbf{S}^{(N+1)} \left(\mathbf{R}^{(N+1)} \right)^{-1} \quad (4.23)$$

where the elements of matrices $\mathbf{R}^{(N+1)}$ and $\mathbf{S}^{(N+1)}$ are given in Appendix B.

The global stiffness matrix of the EDZ can be assembled by using the continuity conditions of traction and fluid flow at the layer interfaces. The final equation system can be expressed as

$$\mathbf{F}^* = \mathbf{K}^* \mathbf{U}^* \quad (4.24)$$

where \mathbf{K}^* is a global stiffness matrix, which is a symmetric matrix with a bandwidth of 6. In addition, \mathbf{U}^* and \mathbf{F}^* are the global vectors of generalized displacements and generalized forces defined as

$$\mathbf{U}^* = [\mathbf{u}^{(1)} \quad \mathbf{u}^{(2)} \quad \dots \quad \mathbf{u}^{(n)} \quad \dots \quad \mathbf{u}^{(N)} \quad \mathbf{u}^{(N+1)}]^T \quad (4.25)$$

$$\mathbf{F}^* = [\mathbf{f}^{(1)} \quad \mathbf{f}^{(2)} \quad \dots \quad \mathbf{f}^{(n)} \quad \dots \quad \mathbf{f}^{(N)} \quad \mathbf{f}^{(N+1)}]^T \quad (4.26)$$

Consider an infinite cylindrical borehole of radius a in a poroelastic medium with the excavation disturbed zone subjected to axisymmetric loading applied at its surface as shown in Fig. 4.1. The boundary conditions in the Laplace-Fourier transform space for the borehole under applied radial traction $F_r(z,t)$ and $F_z(z,t)$ at its surface can be expressed as

$$\tilde{\sigma}_{rr}(1, \xi, s) = \tilde{F}_r(\xi, s) \quad (4.27)$$

$$\tilde{\sigma}_{rz}(1, \xi, s) = \tilde{F}_z(\xi, s) \quad (4.28)$$

$$\text{and } \tilde{p}(1, \xi, s) = 0 \quad \text{for fully permeable surface} \quad (4.29)$$

$$\text{or } \tilde{q}_r(1, \xi, s) = 0 \quad \text{for impermeable surface} \quad (4.30)$$

Let consider the case of a borehole subjected to applied fluid pressure $P(z,t)$ at a fully permeable surface. The boundary conditions in the Laplace-Fourier transform space are given by

$$\tilde{\sigma}_{rr}(1, \xi, s) = -\frac{3(\nu_u - \nu)}{B(1-2\nu)(1+\nu_u)} \tilde{P}(\xi, s) \quad (4.31)$$

$$\tilde{\sigma}_{rz}(1, \xi, s) = 0 \quad (4.32)$$

$$\text{and } \tilde{p}(1, \xi, s) = \tilde{P}(\xi, s) \quad (4.33)$$

The boundary conditions in the Laplace-Fourier transform space when a borehole subjected to applied fluid discharge $Q(z,t)$ at an impermeable surface can be expressed as

$$\tilde{\sigma}_{rr}(1, \xi, s) = -\frac{3(\nu_u - \nu)}{B(1 - 2\nu)(1 + \nu_u)} \tilde{p}(1, \xi, s) \quad (4.34)$$

$$\tilde{\sigma}_{rz}(1, \xi, s) = 0 \quad (4.35)$$

$$\text{and } q_r(1, \xi, s) = \tilde{Q}(\xi, s) \quad (4.36)$$

The global equation system, Eq. (4.24), for each problem is assembled by considering the appropriate boundary conditions given by Eqs. (4.27)-(4.36). The solutions in the Laplace-Fourier transform space are then determined by solving the global equation for discrete values of ξ and s . Time domain solutions can be obtained by applying accurate numerical schemes to Eq. (4.2). The solutions presented in this section are the required influence functions to establish the flexibility equation in the derivation of traction and pore pressure jump at the contact surface for the contact problems between a borehole and a rigid cylindrical plug outlined in the next section.

4.4 Formulation of Contact Problems between a Borehole and a Rigid Cylinder

In this section, contact problems of a rigid cylindrical plug of radius a and height h bonded to a borehole in a poroelastic medium with excavation disturbed zone are considered as shown in Fig. 4.2(a). This is a mixed boundary value problem with radial and shear stresses being zero outside the plug-borehole contact surface and displacements being prescribed along the contact surface. Two contact problems are considered, namely radial misfit case and axial loading case. The first problem is concerned with the rigid plug with the radial misfit of $\Delta_r H(t)$, in which $H(t)$ is Heaviside step function, placed in the borehole. This problem is useful in the development of in situ testing devices such as a pressuremeter for the measurement of geological material properties. Such misfit exists due to the fact that the pressuremeter is tightly fitted with the borehole surface. It is also useful in the study of interface stresses due to a radial misfit between a fiber and a matrix material. The misfit occurs in the composites during the high temperature processing due to difference in magnitude of the thermal expansion coefficient of the fiber and the matrix material. The other contact problem involves the rigid plug pulled by a vertical load of $P_0 H(t)$. The plug is just fitted with the borehole (i.e., no radial displacement). This problem of this nature is useful in the modeling of several problems such as fiber pull-out tests and load diffusion, etc.

In this study, two limiting cases of hydraulic boundary conditions at the contact surface S ($-h/2 \leq z \leq h/2$) between a rigid plug and a borehole surface are assumed, i.e. fully permeable (zero pore pressure) or impermeable (zero radial discharge) surface. Note that the borehole surface is assumed to be fully permeable. For an impermeable plug, contact

traction (both radial and tangential directions) and pore pressure are generated at the surface S . To determine radial and tangential traction, and pore pressure jump denoted by $\tilde{T}_r(\xi, s)$, $\tilde{T}_z(\xi, s)$, and $\tilde{T}_p(\xi, s)$ respectively, the contact surface S is discretized into a total of N_e ring elements as shown in Fig 4.2(b). The displacement compatibility condition is then imposed at the contact surface S . This is done by imposing the resulting displacement variation on the nodal locations at the contact surface S by applying radial traction $\tilde{T}_r(\xi, s)$, tangential traction $\tilde{T}_z(\xi, s)$, and pore pressure jump $\tilde{T}_p(\xi, s)$ on S . It is assumed that the applied radial and tangential traction, and pore pressure jump are constant within each ring element. The relationship between the unknown contact traction, pore pressure jump and the displacements at the surface S can be expressed in the following form

$$\begin{bmatrix} \tilde{\mathbf{G}}^{rr} & \tilde{\mathbf{G}}^{rz} & \tilde{\mathbf{G}}^{rp} \\ \tilde{\mathbf{G}}^{zr} & \tilde{\mathbf{G}}^{zz} & \tilde{\mathbf{G}}^{zp} \\ \tilde{\mathbf{G}}^{pr} & \tilde{\mathbf{G}}^{pz} & \tilde{\mathbf{G}}^{pp} \end{bmatrix} \begin{Bmatrix} \tilde{\mathbf{T}}_r \\ \tilde{\mathbf{T}}_z \\ \tilde{\mathbf{T}}_p \end{Bmatrix} = \begin{Bmatrix} \tilde{\mathbf{u}}_r \\ \tilde{\mathbf{u}}_z \\ \tilde{\mathbf{u}}_p \end{Bmatrix} \quad (4.37)$$

In Eq. (4.37), the element \tilde{G}_{kl}^{ij} , where $k, l = 1, 2, 3, \dots, N_e$, of $\tilde{\mathbf{G}}^{ij}$ denotes the influence functions, which are radial displacement ($i = r$), vertical displacement ($i = z$), and radial fluid displacement ($i = p$) at the center of the k^{th} ring element due to an instantaneous radial ring load ($j = r$), a vertical ring load ($j = z$), and a ring fluid pressure ($j = p$) respectively applied over the l^{th} ring element. The vectors $\tilde{\mathbf{T}}_i$ and $\tilde{\mathbf{u}}_i$ ($i = r, z, p$) can be expressed as

$$\tilde{\mathbf{T}}_r = [\tilde{T}_r(z_1, s) \quad \tilde{T}_r(z_2, s) \quad \dots \quad \tilde{T}_r(z_{N_e}, s)]^T; \quad (4.38)$$

$$\tilde{\mathbf{T}}_z = [\tilde{T}_z(z_1, s) \quad \tilde{T}_z(z_2, s) \quad \dots \quad \tilde{T}_z(z_{N_e}, s)]^T; \quad (4.39)$$

$$\tilde{\mathbf{T}}_p = [\tilde{T}_p(z_1, s) \quad \tilde{T}_p(z_2, s) \quad \dots \quad \tilde{T}_p(z_{N_e}, s)]^T; \quad (4.40)$$

$$\tilde{\mathbf{u}}_p = [0 \quad 0 \quad \dots \quad 0]^T; \quad (4.41)$$

In addition,

$$\tilde{\mathbf{u}}_r = [\Delta_r / s \quad \Delta_r / s \quad \dots \quad \Delta_r / s]^T; \quad (4.42)$$

$$\tilde{\mathbf{u}}_z = [0 \quad 0 \quad \dots \quad 0]^T; \quad (4.43)$$

for the case of radial misfit, and

$$\tilde{\mathbf{u}}_r = [0 \quad 0 \quad \dots \quad 0]^T; \quad (4.44)$$

$$\tilde{\mathbf{u}}_z = [\Delta_z / s \quad \Delta_z / s \quad \cdots \quad \Delta_z / s]^T; \quad (4.45)$$

for the applied vertical loading case. Note that z_i ($i=1, 2, \dots, N_e$) denotes the vertical coordinate of the nodal location of the i^{th} ring element.

For a fully permeable rigid plug, there is no pore pressure generated on the entire borehole surface and $\tilde{\mathbf{T}}_p$ is a null vector. Equation (4.37) then reduces to

$$\begin{bmatrix} \tilde{\mathbf{G}}_{rr} & \tilde{\mathbf{G}}_{rz} \\ \tilde{\mathbf{G}}_{zr} & \tilde{\mathbf{G}}_{zz} \end{bmatrix} \begin{Bmatrix} \tilde{\mathbf{T}}_r \\ \tilde{\mathbf{T}}_z \end{Bmatrix} = \begin{Bmatrix} \tilde{\mathbf{u}}_r \\ \tilde{\mathbf{u}}_z \end{Bmatrix} \quad (4.46)$$

Eqs. (4.37) and (4.46) yield nodal solutions for contact traction and pore pressure jump. Time domain solutions can be expressed in the next section by employing an accurate numerical Laplace-Fourier inversion scheme.

The average radial contact stress T_0 over S for the radial misfit case can be determined from

$$T_0 = \frac{a\mu}{h} \int_{-h/2}^{h/2} T_r(1, z) dz \quad (4.47)$$

and the equilibrium of a plug under the vertical load P_0 is given by

$$P_0 = 2\pi a^2 \mu \int_{-h/2}^{h/2} T_z(1, z) dz \quad (4.48)$$

4.5 Numerical Results and Discussion

The solution procedure described in the previous sections is implemented into a computer program to investigate time-dependent response of a borehole in a poroelastic medium with an excavation disturbed zone. The main computational effort is involved in the evaluation of influence functions G_{ij}^{kl} . The explicit analytical solutions for G_{ij}^{kl} are given in terms of an infinite integral with respect to the Fourier transform parameter ξ , which can be converted into a semi-infinite integral since the integrand is either an even or odd function of ξ . The semi-infinite integrals of G_{ij}^{kl} are then computed by using a numerical quadrature scheme that subdivides the interval of integration and employs a 21-point Gauss-Kronrod rule to estimate the integral over each subinterval. Time-domain solutions are obtained by using

an accurate Laplace inversion scheme reported in the literature. Piessens (1975) conducted a review of numerical Laplace inversion schemes and found that the scheme proposed by Stehfest (1970) is very accurate for time-dependent problems. In the past, Stehfest's scheme has been widely used in a variety of poroelastic problems (Rajapakse 1993, Abousleiman et al. 1997, Cheng 1997, and Senjuntichai and Sapsathiam 2006). According to Stehfest's (1970) time domain solution is given by Eq. (3.66) in the previous chapter.

. The accuracy of present solution was verified by comparison with the existing solutions given by Rajapakse (1993) for a borehole in a poroelastic medium with incompressible constituents ($\nu = 0.3$, $\nu_u = 0.5$ and $B = 1.0$) subjected to axisymmetric radial traction of uniform intensity f_0 over a segment of length $2h$. The boundary conditions for this problem are given in Eqs. (4.27)-(4.33) with $\tilde{F}_r(\xi, s) = f_0 \sin(\xi b) / \xi s$ and $\tilde{F}_z(\xi, s) = 0$. Figures 4.3(a) and 4.3(b) show comparisons of nondimensional profiles of pore pressure and fluid discharge respectively in the radial direction ($z=0$) for $b/a = 0.25$ and 1.0 at nondimensional time, $ct/a^2 = 0.01$ and 0.10 . Excellent agreement between both solutions is noted in both figures. Comparisons of numerical solutions corresponding to contact problems shown in Fig. 4.2(a) are presented next. Fig. 4.4 shows comparisons of average radial traction ($-T_0 a / \mu \Delta_r$) and an axial stiffness ($P_0 / \mu a \Delta_z$) given by Eq. (4.46) and (4.47) respectively with those presented by Rajapakse and Gross (1996) and Robinson (2002) for a borehole in an isotropic medium ($\nu = 0.3$) containing a rigid cylindrical plug. It is noted that the present solutions agree very closely with both existing solutions at all length-radius ratios of rigid plug. The accuracy of the present solution scheme is thus confirmed through these independent comparisons.

Numerical results for displacement, stresses, excess pore pressure and radial discharge corresponding to uniform traction or fluid source applied at the borehole wall over a segment of length $2b$ are presented next. In this paper, the disturbed zone during drift excavation is assumed to be two diameter of the borehole (Sato et al. 2000) (i.e. $d/a = 4$). The variations of shear modulus and permeability coefficient in the EDZ are given by Eqs. (4.18) and (4.19) respectively with $0 \leq m_1 \leq 0.25$ and $m_2 \geq 0$. In addition, a poroelastic material with compressible constituents ($\nu = 0.3$, $\nu_u = 0.4$, $B = 0.9$) is employed in the numerical study. Note that the poroelastic solution without the EDZ can be obtained from the present solution with $m_1 = m_2 = 0$. In addition, two limiting cases of hydraulic boundary conditions are considered at the borehole wall, i.e. a fully permeable surface (zero pore pressure) and an impermeable surface (zero fluid discharge).

The first set of numerical results corresponding to the case where a borehole subjected to axisymmetric radial traction of intensity f_0 is presented in Figs. 4.5-4.7 with $b/a=1$. Figure 4.5 presents radial variations of non-dimensional excess pore pressure at the mid-plane ($z/a=0$) for both permeable and impermeable borehole surfaces. The effect of the EDZ on shear modulus is considered in Fig. 4.5(a) with $m_1=0, 0.1, \text{ and } 0.2$, and $m_2=0$, whereas the case of $m_1=0$ with $m_2=0, 0.2, \text{ and } 0.4$ is considered in Fig. 4.5(b) to study the effect of permeability change in the EDZ. Numerical results presented in Fig. 4.5 indicate that the disturbed zone has a significant influence on excess pore pressure near the borehole wall. It is found that pore pressure is zero at $r=a$ for a fully permeable wall before increasing rapidly with the radial distance reaching its peak near the borehole wall ($r/a < 1.5$). For an impermeable wall, the maximum value of pore pressure is observed at the wall ($r/a=1$) before decreasing rapidly with the radial distance. Pore pressure increases with increasing the shear modulus coefficient m_1 regardless of the hydraulic boundary condition at the borehole wall. On the contrary, pore pressure decreases with increasing the permeability coefficient m_2 as shown in Fig. 4.5(b). It is also noted that the pore pressure is virtually negligible when $r/a > 4$ irrespective of the hydraulic boundary condition at the borehole wall.

Variations of non-dimensional fluid discharge in the radial direction ($z/a=0$) due to uniform radial traction are presented in Figs. 4.6(a) and 4.6(b) respectively for different values of m_1 and m_2 . In the case of fully permeable wall, radial discharge is very high near the wall and then decreases rapidly with the radial distance. At early times ($ct/a^2 \leq 0.01$), the fluid flow is inward (negative value) near the borehole wall ($r/a < 1.2$), and becomes outward (positive value) with increasing the radial distance. As time progresses ($ct/a^2 > 1$), the discharge is inward at all points in the medium. Radial fluid discharge corresponding to an impermeable borehole wall is completely different from the fully permeable case. Radial fluid discharge in the case of impermeable borehole is zero at the borehole wall due to the boundary condition at all time instants. It then increases gradually with the radial distance near the borehole wall ($r/a < 1.5$) before decreasing with the radial distance. It is also found that the fluid discharge for the impermeable wall in Fig. 4.6(a) increases with increasing m_1 similar to what observed for the pore pressure in Fig. 4.5(a). However, the discharge profiles in Fig. 4.6(b) show somewhat different behavior from the pore pressure profiles in Fig. 4.5(b) that they increase with increasing m_2 . This is consistent with the fact that the larger values of m_2 indicate more permeable medium, which results in more flow and lower pore pressure in the vicinity of the borehole.

Figures 4.7(a) and 4.7 (b) show radial variations of non-dimensional radial displacement and tangential stress ($z/a=0$) for different values of m_1 with $m_2=0$. Radial displacement in Fig. 4.7(a) has a maximum value at the borehole wall, and decays rapidly with the radial distance regardless of the hydraulic boundary condition. The influence of m_1 on the displacement is observed only in the vicinity of the borehole wall and the displacement once again increases with increasing m_1 similar to what observed for pore pressure and fluid discharge respectively in Figs. 4.5(a) and 4.6(a). It should be noted that the difference between displacements at early time ($ct/a^2 < 0.01$) and larger time ($ct/a^2 > 10$) is less than 5% at all points for both fully permeable and impermeable walls. Radial profiles of non-dimensional tangential stress in Fig. 4.7(b) show a similar behavior to the radial displacement profiles in Fig. 4.7(a). The peak stresses are observed at the wall and decays along the radial distance but the tangential stress decays more rapidly when compared to the radial displacement profiles in Fig. 4.7(a). In contrast to other quantities, the tangential stress decreases with increasing m_1 . It is implied that the influence of the EDZ results in reduction of stress and increase of displacement around the borehole. Solutions for radial displacement and tangential stress profiles were also plotted for different values of m_2 . It was found that their solutions for different values of m_2 are virtually identical indicating that the variation of permeability in the EDZ has negligible influence on displacement and stress around the borehole under applied radial traction.

Numerical results corresponding to a borehole wall subjected to specified fluid pressure of uniform intensity p_0 [$\tilde{P}(\xi, s) = p_0 \sin(\xi b) / \xi s$] and radial discharge of uniform intensity q_0 [$\tilde{Q}(\xi, s) = q_0 \sin(\xi b) / \xi s$] over a length of $b/a=1$ are presented in Figs. 4.8 and 4.9 respectively. Profiles of non-dimensional radial displacement, tangential stress, excess pore pressure, and radial discharge along the radial distance ($z/a=0$) with a fully permeable borehole wall are shown in Figs. 4.8(a)-4.8(d) respectively for different values of m_1 and m_2 . Under applied fluid pressure, the maximum negative value of radial displacement is observed at the center of applied loading, and radial displacement decreases rapidly along the radial distance approaching negligible level when $r/a > 4$ for all values of m_1 and m_2 . It can be seen from Fig. 4.8(b) that the maximum tangential stress is about 20% more than the specified fluid pressure at the borehole wall. Tangential stress decreases rapidly with the radial distance especially at the early time, and it is compressive at all points along the r -axis. Excess pore pressure profiles in Fig. 4.8(c) show a similar trend to what observed from the tangential stress profiles in Fig. 4.8(b). The maximum pore pressure is equal to $-p_0$ at the borehole wall due to the imposed boundary condition, and it decreases rapidly with the radial distance. At

the early time ($ct/a^2 < 0.1$), pore pressure in all EDZs decreases rapidly near the borehole wall and becomes suction (positive value) with increasing radial distance. For $ct/a^2 > 0.1$, pore pressure increases gradually with time before diminishing to negligible level when $r/a > 4$. Both tangential stress and excess pore pressure profiles decrease with increasing m_1 but increase with decreasing m_2 . Initially, radial discharge illustrated in Fig 4.8(d) is very high near the borehole wall and decreases along the radial direction. Radial discharge increases with increasing the value of m_2 . Fluid discharge can be negligible when $r/a > 4$ at all time instants.

Figures 4.9(a)-4.9(d) show profiles of non-dimensional radial displacement, tangential stress, excess pore pressure, and radial discharge respectively due to specified fluid discharge at an impermeable borehole wall. Radial displacement and tangential stress profiles in Fig. 4.9(a) and 4.9(b) respectively show similar trends to those in Fig. 4.8(a) and 4.8(b) under applied fluid pressure. The maximum value of displacement is observed at the borehole wall, and the displacement decreases along the radial direction diminishing to zero when $r/a > 4$. It is found from Fig. 4.9(b) that the largest value of tangential stress always occurs at borehole walls ($r/a = 1$) for all values of m_1 , m_2 before decreasing rapidly with the radial distance especially at early time. Tangential stress decreases with increasing m_1 and m_2 . Numerical results for excess pore pressure profiles in Fig. 4.9(c) indicate that no suction is developed in the medium at all time instants for applied fluid discharge. Initially ($ct/a^2 = 0.01$), the excess pore pressure is observed only near the borehole wall, and gradually developed in the medium as time progresses. The influence of the EDZ on excess pore pressure is similar to that of tangential stress shown in Fig. 4.9(b). Naturally, the normalized discharge at $r/a = 1$ shown in Fig. 4.9(d) is equal to one at all time instants irrespective of m_1 and m_2 due to the specified boundary condition. Radial discharge decreases with increasing m_1 , but increases with increasing m_2 . It should also be noted that final solutions of all results presented in Fig. 4.9 are reached when $ct/a^2 > 100$.

The final set of numerical results corresponds to contact problems involving a rigid cylindrical plug bonded to an infinite borehole with a fully permeable wall and the EDZ [see Fig. 4.2(a)]. Figure 4.10(a) shows non-dimensional average value of radial stress ($T_0 a / \mu \Delta_r$), given by Eq. (4.47), for a rigid cylindrical plug with a radial misfit of Δ_r for different gradients of shear modulus in the EDZ ($m_1 = 0.1, 0.2$ and 0.3) and different times ($ct/a^2 = 0.01, 0.1$ and 1). Solutions are presented with different length-radius ratios of a rigid cylindrical plug (h/a) varying from 0.1 to 10.0. Both fully permeable and impermeable

plugs are considered. Very large compressive radial stress is developed at the contact surface for small values of h/a , and it decreases with increasing h/a . The change in shear modulus has a significant influence on the radial stress, i.e. an average radial stress decreases with increasing the change in shear modulus (larger value of m_1). The change in permeability is found to be less influence on the radial stress. The solutions approach an asymptotic value when $h/a > 10$, which is the plane-strain solution. The numerical solutions for $T_0 a / \mu \Delta_r$ under a fully permeable plug are within five percent different from those of an impermeable one. Non-dimensional radial stress profiles $[\sigma_{rr}(a, z)a / \mu \Delta_r]$ along the contact surface of rigid cylinder ($h/a = 2.0$) as shown in Fig. 4.2(a) with radial misfit are shown in Fig. 4.10(b). The radial contact stress is symmetric about the $z=0$ plane and compressive throughout the contact surface. Radial stress is singular at the edge of the cylinder, and it is nearly constant over the central part of the plug. The degree of stress singularity is found to be in a square root order, which agrees with the case of a cylindrical plug in a borehole in an isotropic elastic medium (Robinson 2002). In addition, radial stress in the central part of the plug decreases with increasing m_1 .

The numerical results for the applied vertical loading are presented next. Non-dimensional axial stiffness ($P_0 / \mu a \Delta_z$) of a rigid cylinder bonded to a borehole surface is presented in Fig 4.11(a). The variation of axial stiffness with respect to h/a is almost linear, and its slope decreases with increasing the value of m_1 . Numerical results presented in Fig. 4.11(a) indicate that the axial stiffness of the plug depends significantly on the change in shear modulus in the EDZ. Figure 4.11(b) presents non-dimensional shear stress $[\sigma_{rz}(a, z)a / \mu \Delta_z]$ along the contact surface of an axially loaded rigid plug. Shear stress profiles are symmetric about $z=0$ plane, and have a singularity at the two edges, similar to what observed in radial stress profiles shown in Fig 4.10(b). It is also constant over the central part of contact surface, and decreases with increasing the values of m_1 . In addition, the influence of hydraulic boundary condition along the plug surface is negligible under the vertical loading case.

4.6 Conclusion

In this chapter, the general solutions of a cylindrical borehole in a poroelastic medium with an excavation disturbed zone subjected to axisymmetric loading are based on Biot's theory of poroelasticity by applying Laplace and Fourier integral transforms. The general solutions in the Laplace-Fourier domains are expressed in terms of modified Bessel functions of the first and second kinds. These solutions are used to formulate boundary value problems

corresponding to a borehole subjected to axisymmetric loading applied at its surface, and contact problems involving a borehole containing a rigid cylinder. Numerical results indicate that changes in shear modulus and permeability coefficient in the excavation disturbed zone have a significant influence on the solutions especially in the vicinity of the borehole wall. The shear modulus is reduced due to the excavation process, and it results in more displacement, excess pore pressure, and fluid discharge, but less tangential stress. The drilling process leads to larger permeability coefficient in the EDZ, which causes a decrease in pore pressure but an increase in fluid discharge. The influence from the excavation disturbed zone is however less significant in the contact problems between a borehole and a rigid plug. The plane strain solutions are attained when $h/a > 10$ for both cases of the radial misfit and the vertical loading. The solutions presented in this chapter can be employed to examine several practical problems in geomechanics related to pressuremeter devices, ground-water wells, natural resource explorations and waste disposal, etc.



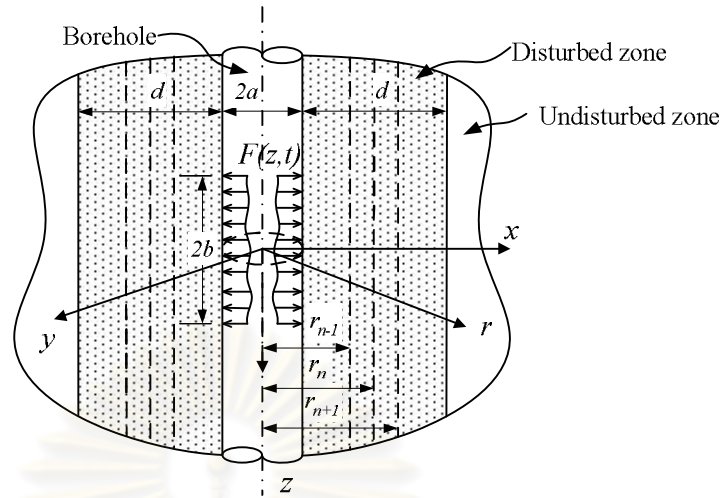


Figure 4.1 Infinite borehole in poroelastic medium with excavation disturbed zone.

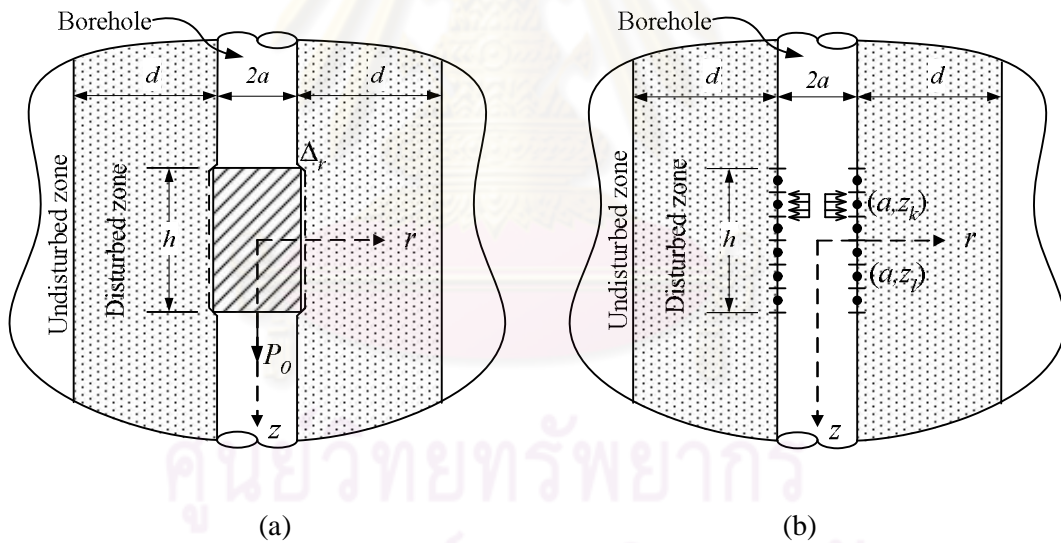


Figure 4.2 (a) A rigid cylinder bonded to a borehole with an excavation disturbed zone. (b) Unit radial loading applied over a finite segment.

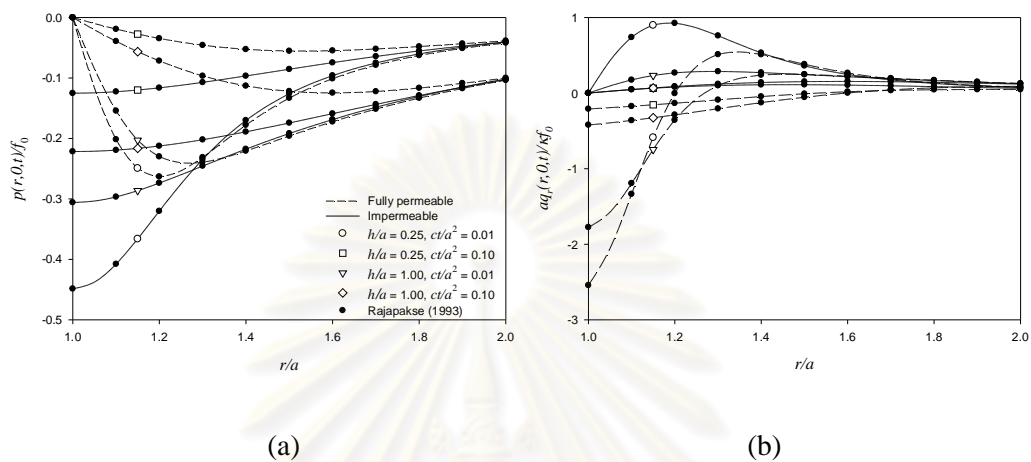


Figure 4.3 Comparison with existing solutions for a borehole in a homogeneous proelastic medium with incompressible constituents.

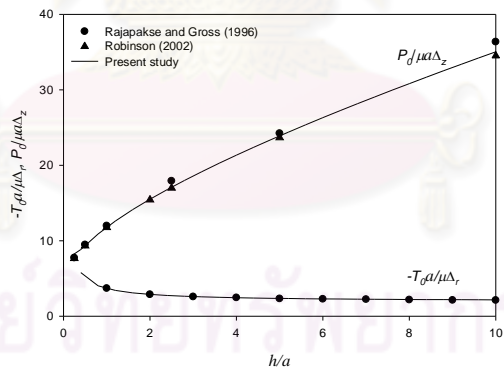
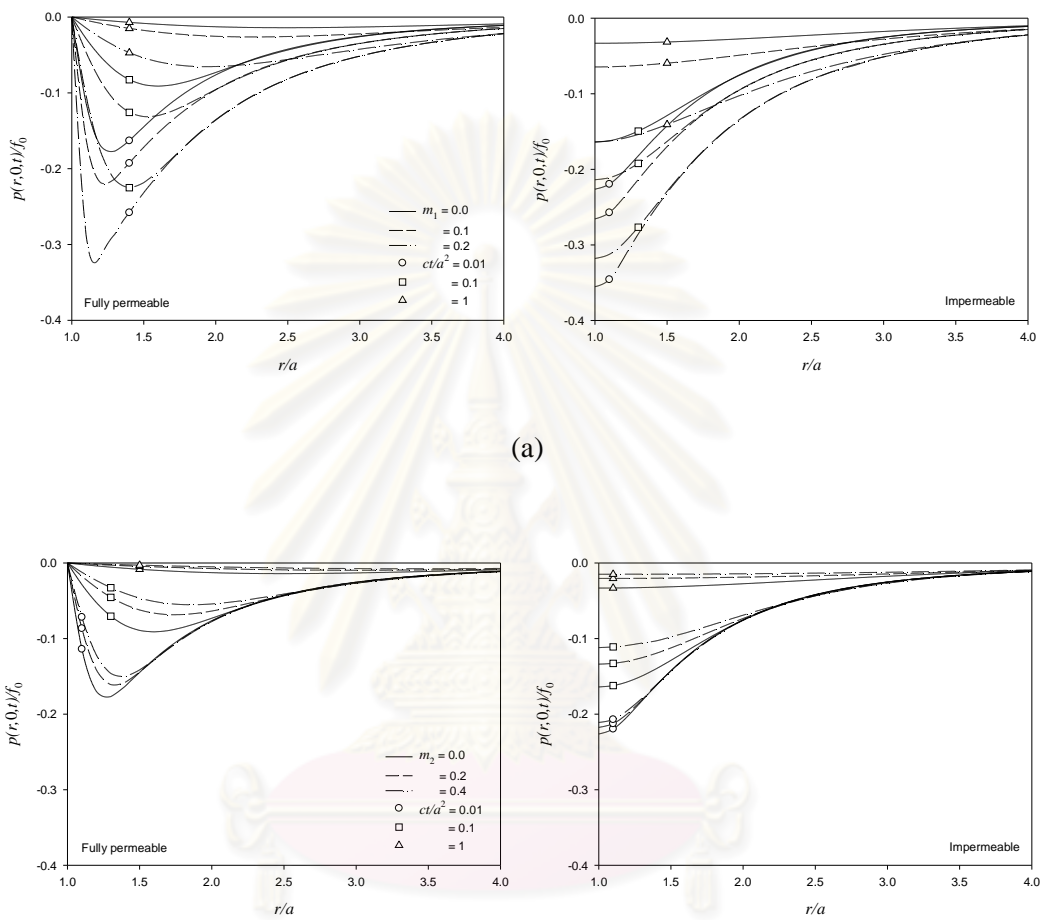


Figure 4.4 Comparison with existing solutions for a rigid cylinder bonded to a borehole in an elastic medium.



(a)

(b)

Figure 4.5 Profiles of excess pore pressure along the r -axis due to applied radial traction for different values of (a) m_1 and (b) m_2 .

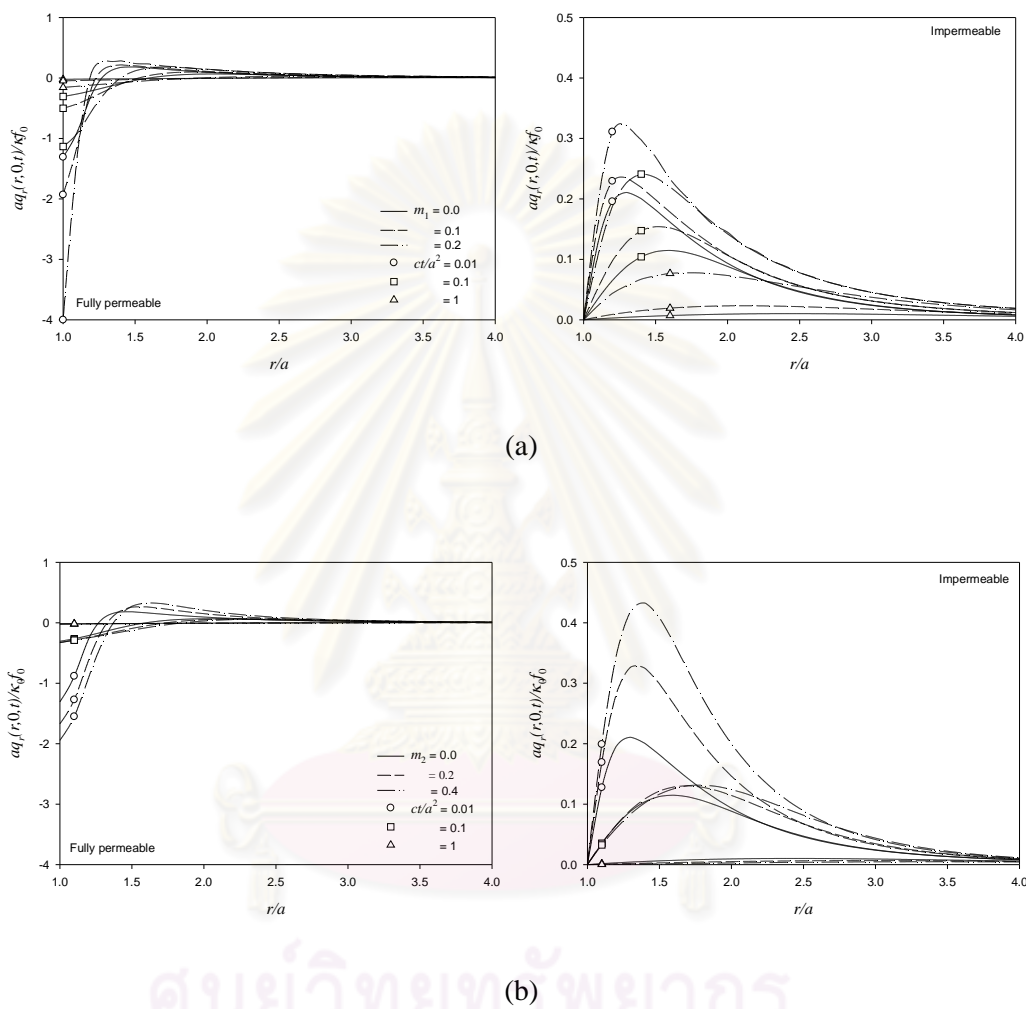


Figure 4.6 Profiles of fluid discharge along the r -axis due to applied radial traction for different values of (a) m_1 and (b) m_2 .

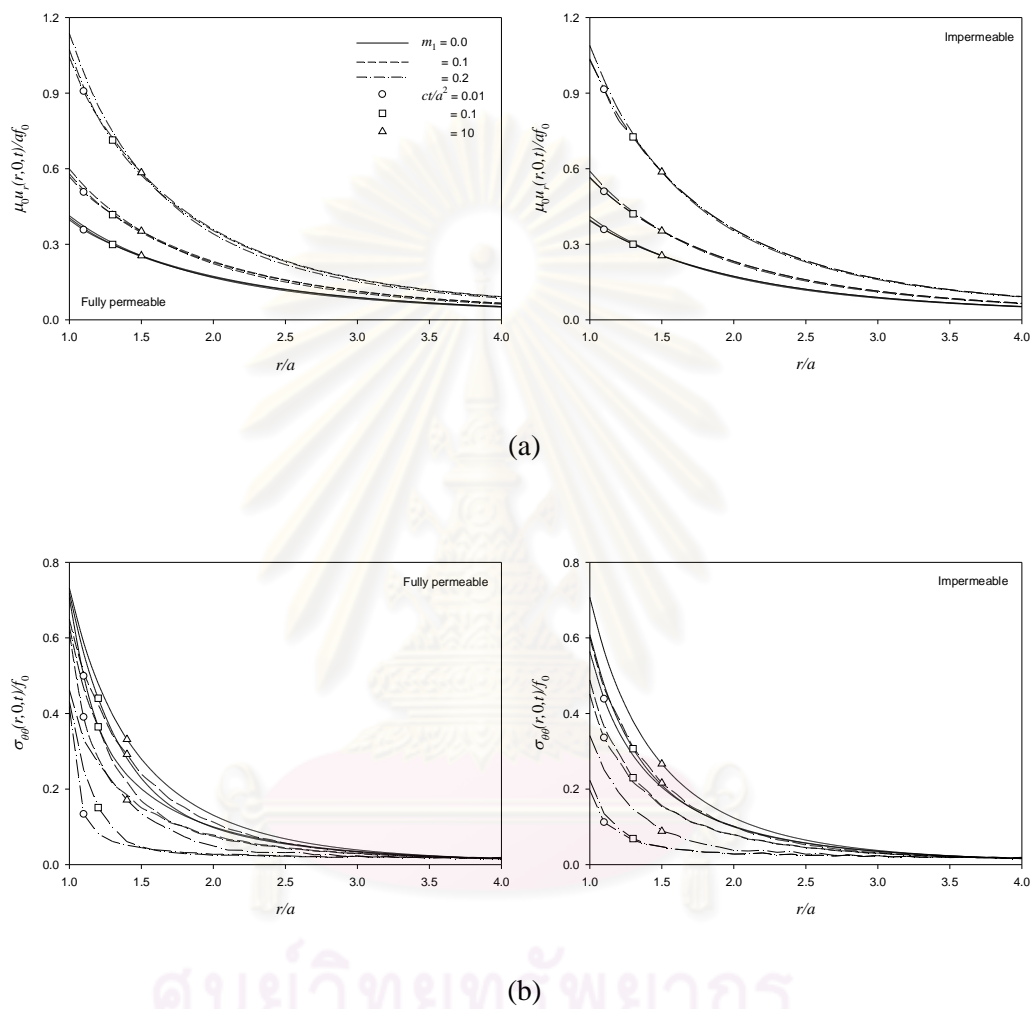


Figure 4.7 Profiles of (a) displacement and (b) tangential stress different shear modulus along the r -axis due to applied radial traction.

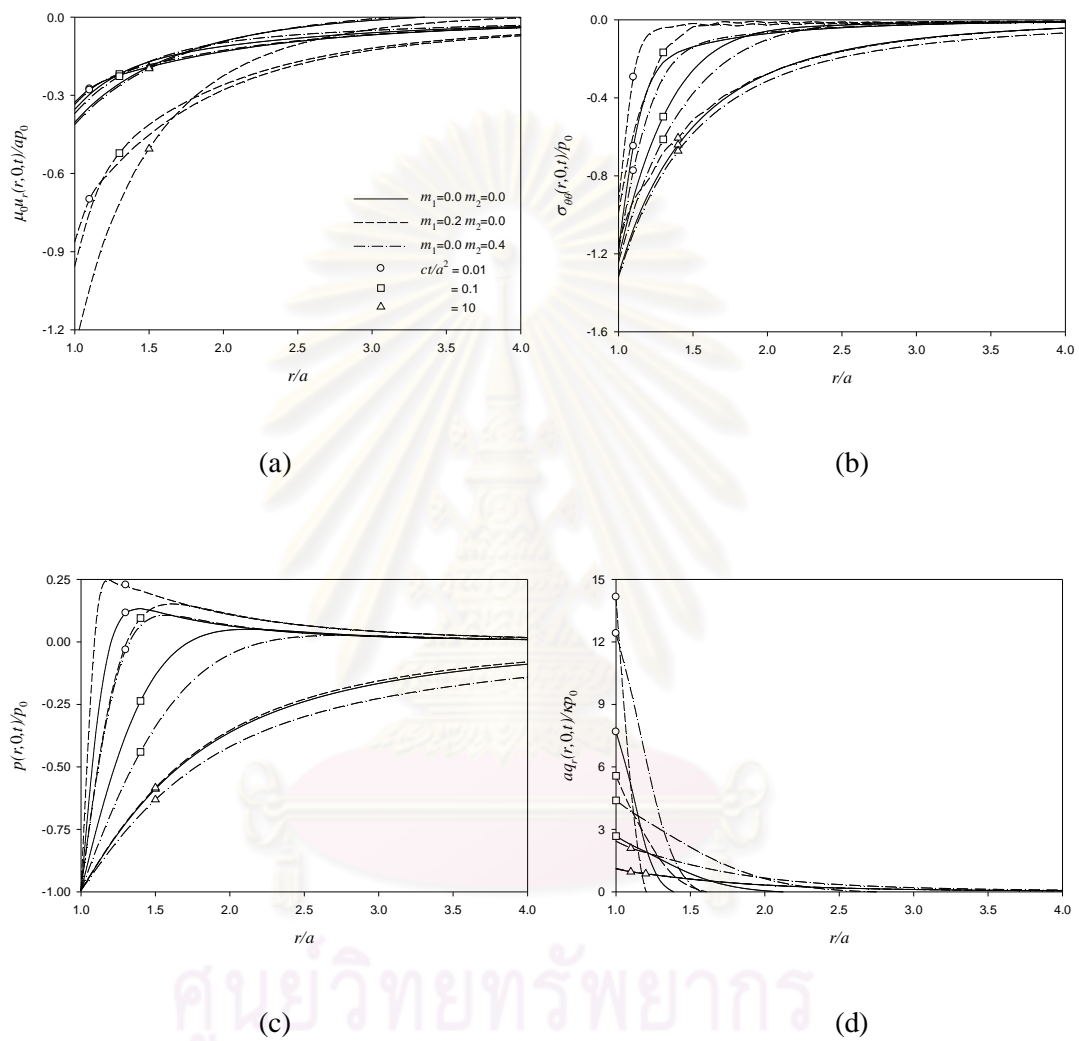


Figure 4.8 Profiles of (a) displacement, (b) tangential stress, (c) excess pore pressure and (d) fluid discharge along the r -axis due to applied fluid pressure.

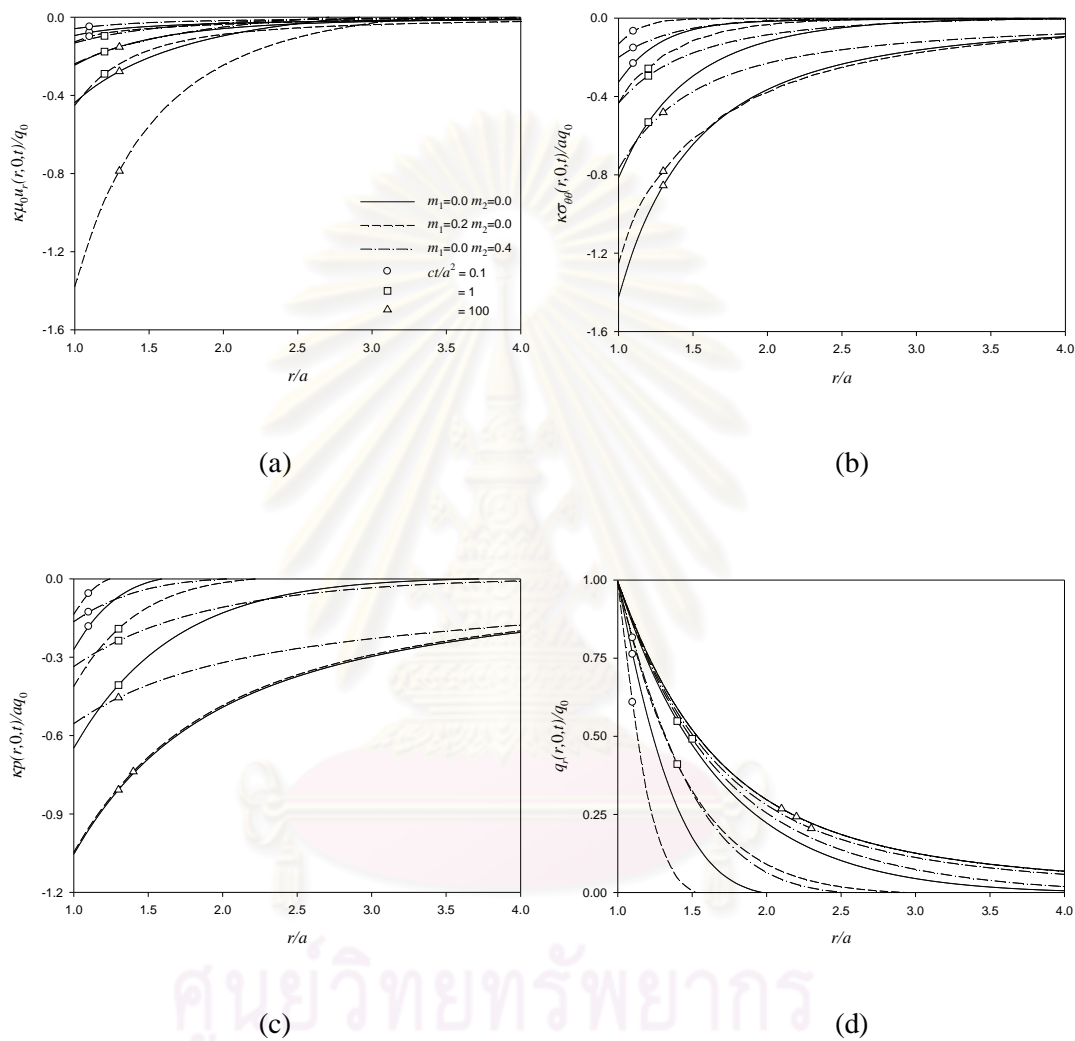


Figure 4.9 Profile of (a) displacement, (b) tangential stress, (c) excess pore pressure and (d) fluid discharge along the r -axis due to applied fluid discharge.

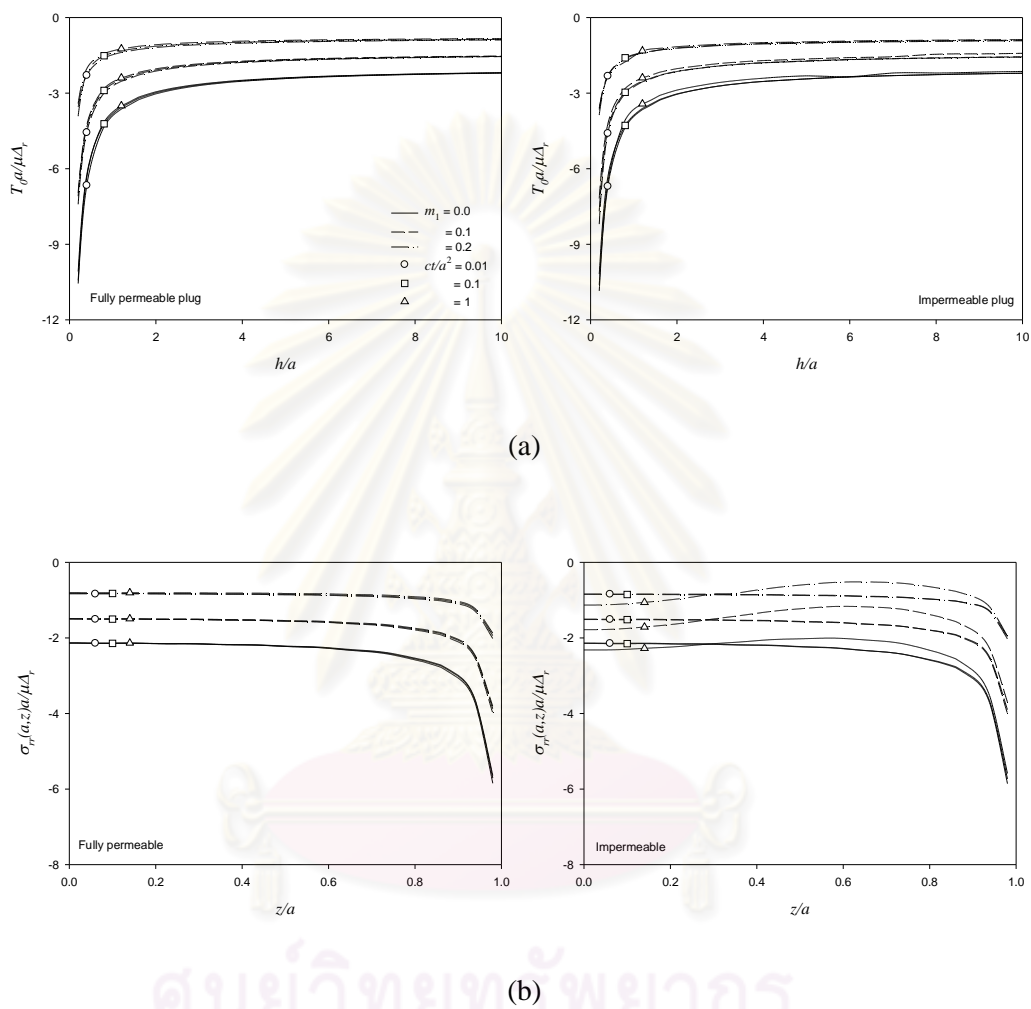


Figure 4.10 Profile of (a) average radial traction and (b) radial stress along the contact surface for radial misfit.

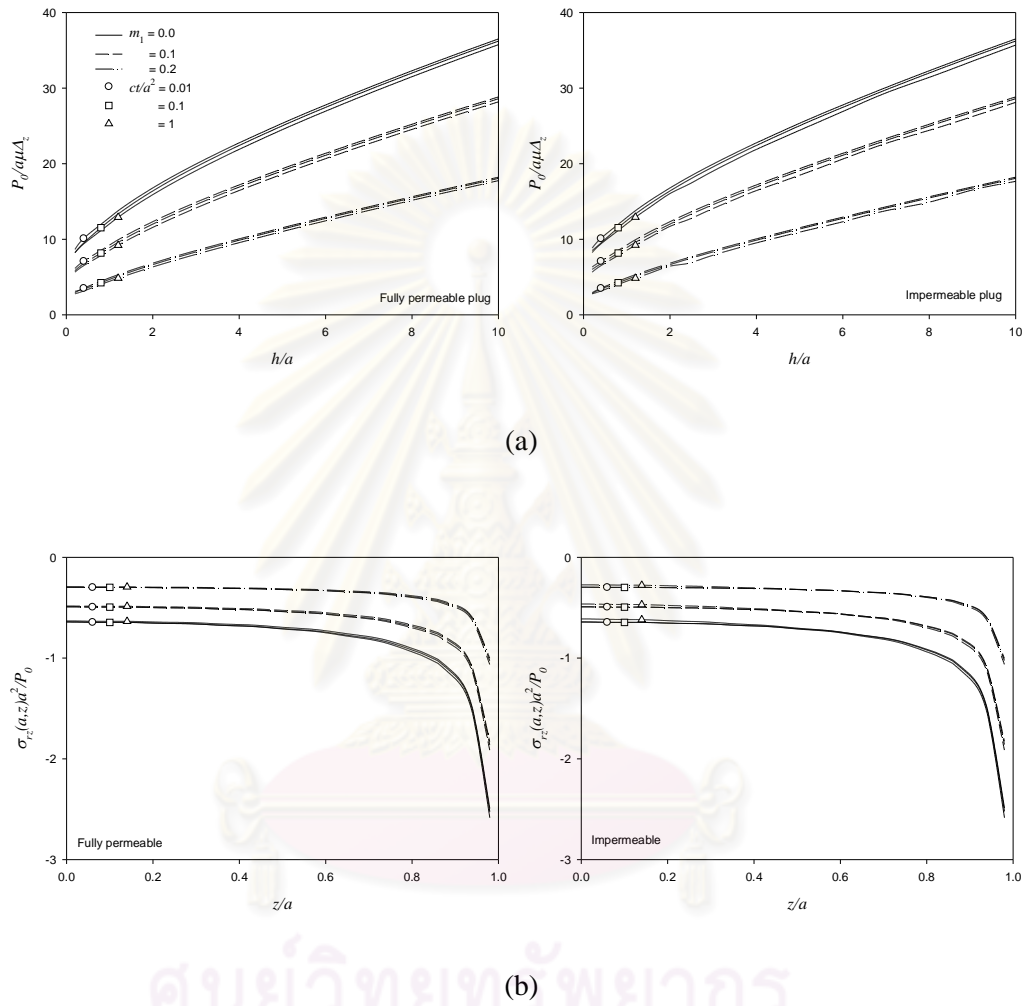


Figure 4.11 Profile of (a) axial stiffness and (b) tangential stress along the contact surface for applied vertical loading.

CHAPTER V

DYNAMIC RESPONSE OF BOREHOLE WITH DISTURBED ZONE

5.1 General

The dynamic response of a cylindrical borehole in an elastic medium is of fundamental importance in various fields, such as geotechnical engineering, mining engineering, and geophysical exploration. For example, analysis of gas explosion inside a mine on the surrounding rock is important for evaluating the damage caused by gas explosions. This chapter presents dynamic response of an infinite cylindrical borehole in a poroelastic medium with excavation disturbed zone. The borehole is subjected to axisymmetric time-harmonic ring loading. The governing equations of Biot's poroelastodynamics theory are uncoupled by using two scalar and two vector potentials. The general solutions of displacements, stresses and pore pressure in the frequency domain are derived through the application of Fourier integral transform with respect to the vertical coordinate. The accuracy of the present solutions is confirmed through comparisons with existing solutions for boreholes in elastic and poroelastic media.

5.2 Governing Equations and General Solutions

Consider axisymmetric deformations of homogenous poroelastic medium with an infinite cylindrical borehole. A cylindrical coordinate system (r, θ, z) is defined as shown in Fig. 4.1 with the z -axis along the center of the borehole. The constitutive relations for a homogeneous poroelastic material are given in Eqs. (3.5)-(3.8). The governing equations for axisymmetric motions of a poroelastic medium, in the absence of body forces (solid and fluid) and a fluid source, can be expressed according to Biot (1962) as

$$\mu \nabla^2 u_r + (\lambda + \alpha^2 M + \mu) \frac{\partial \varepsilon}{\partial r} - \mu \frac{u_r}{r^2} - \alpha M \frac{\partial \zeta}{\partial r} = \rho \ddot{u}_r + \rho_f \ddot{w}_r \quad (5.1)$$

$$\mu \nabla^2 u_z + (\lambda + \alpha^2 M + \mu) \frac{\partial \varepsilon}{\partial z} - \alpha M \frac{\partial \zeta}{\partial z} = \rho \ddot{u}_z + \rho_f \ddot{w}_z \quad (5.2)$$

$$\alpha M \frac{\partial \varepsilon}{\partial r} - M \frac{\partial \zeta}{\partial r} = \rho_f \ddot{u}_r + m \ddot{w}_r + b \dot{w}_r \quad (5.3)$$

$$\alpha M \frac{\partial \varepsilon}{\partial z} - M \frac{\partial \zeta}{\partial z} = \rho_f \ddot{u}_z + m \ddot{w}_z + b \dot{w}_z \quad (5.4)$$

where the superscript dot denotes the derivative of field variables with respect to the time parameter t ; ρ and ρ_f denote the mass densities of the bulk material and the pore fluid respectively; m is a density-like parameter defined as $m = \rho_f / \beta$, in which β is porosity; b is a parameter accounting for the internal friction due to the relative motion between the solid matrix and the pore fluid. If internal friction is neglected then $b = 0$. In addition, the parameters α ($0 \leq \alpha \leq 1$) and M ($0 \leq M < \infty$) can be defined as

$$\alpha = \frac{3(v_u - \nu)}{B(1 - 2\nu)(1 + \nu_u)} \quad (5.5)$$

$$M = \frac{2\mu B^2(1 - 2\nu)(1 + \nu_u)^2}{9(v_u - \nu)(1 - 2\nu_u)} \quad (5.6)$$

For a completely dry material, $\alpha = 0$ and $M = 0$, whereas for a material with incompressible constituents $\alpha = 0$ and $M \rightarrow \infty$. In addition, ∇^2 is the Laplace operator defined by

$$\nabla^2 = \frac{\partial^2}{\partial r^2} + \frac{1}{r} \frac{\partial}{\partial r} + \frac{\partial^2}{\partial z^2} \quad (5.7)$$

The governing partial differential equations, Eqs. (5.1)-(5.3) can be solved by using the following Helmholtz representation for axisymmetric vector fields

$$u_r(r, z, t) = \frac{\partial \phi_1}{\partial r} + \frac{\partial^2 \varphi_1}{\partial r \partial z} \quad (5.8)$$

$$u_z(r, z, t) = \frac{\partial \phi_1}{\partial z} - \frac{1}{r} \frac{\partial}{\partial r} \left(r \frac{\partial \varphi_1}{\partial r} \right) \quad (5.9)$$

$$w_r(r, z, t) = \frac{\partial \phi_2}{\partial r} + \frac{\partial^2 \varphi_2}{\partial r \partial z} \quad (5.10)$$

$$w_z(r, z, t) = \frac{\partial \phi_2}{\partial z} - \frac{1}{r} \frac{\partial}{\partial r} \left(r \frac{\partial \varphi_2}{\partial r} \right) \quad (5.11)$$

where ϕ_i ($i = 1, 2$) and φ_i ($i = 1, 2$) are scalar and vector fields respectively.

Substituting Eqs. (5.8)-(5.11) into Eqs. (5.1)-(5.4) together with the assumption that the motion is time-harmonic with a factor $e^{i\omega t}$, where ω is the frequency of excitation, yields two sets of partial differential equations for scalar field ϕ_1 , ϕ_2 and vector fields φ_1 , φ_2 as follows

$$\left[(\lambda + \alpha M + 2\mu) \nabla^2 + \rho \delta^2 \right] \phi_1 = -(\alpha M \nabla^2 + \rho_f \delta^2) \phi_2 \quad (5.12)$$

$$(\alpha M \nabla^2 + \rho_f \delta^2) \phi_1 = -(M \nabla^2 + m \delta^2 - ib \delta) \phi_2 \quad (5.13)$$

and

$$(\mu \nabla^2 + \rho \delta^2) \phi_1 = -\delta^2 \rho_f \phi_2 \quad (5.14)$$

$$\delta^2 \rho_f \phi_1 = -\delta^2 m \phi_2 + i \delta b \phi_2 \quad (5.15)$$

Note that the term $e^{i\omega t}$ is suppressed from all expressions for brevity. The above partial differential equations are reduced to ordinary differential equations by performing appropriate Fourier transform with respect to the z -coordinate given by Eq. (4.1), in which its inverse relationship is given by Eq. (4.2). After lengthy manipulations, it can be shown that the general solutions of Fourier transforms of ϕ_i ($i=1, 2$) and φ_i ($i=1, 2$) can be expressed as

$$\tilde{\phi}_1(r, \xi) = AI_0(\gamma_1 r) + BK_0(\gamma_1 r) + CI_0(\gamma_2 r) + DK_0(\gamma_2 r) \quad (5.16)$$

$$\tilde{\phi}_2(r, \xi) = \chi_1 [AI_0(\gamma_1 r) + BK_0(\gamma_1 r)] + \chi_2 [CI_0(\gamma_2 r) + DK_0(\gamma_2 r)] \quad (5.17)$$

$$\tilde{\varphi}_1(r, \xi) = EI_0(\gamma_3 r) + FK_0(\gamma_3 r) \quad (5.18)$$

$$\tilde{\varphi}_2(r, \xi) = \chi_3 [EI_0(\gamma_3 r) + FK_0(\gamma_3 r)] \quad (5.19)$$

where $A(\xi)$, $B(\xi)$, $C(\xi)$, $D(\xi)$, $E(\xi)$, and $F(\xi)$ are arbitrary functions to be determined by using appropriate boundary and/or continuity conditions relevant to a given problem. γ_i ($i=1, 2, 3$) and χ_i ($i=1, 2, 3$) are given in Appendix C. A tilde ($\tilde{}$) denotes the Fourier transform of a function. In addition, I_n and K_n are modified Bessel functions of the first and second kinds respectively of the n th order (Watson 1944). Thereafter, the general solutions for displacements, excess pore pressure and stresses can be obtained in terms of the arbitrary functions, $A(\xi)$ to $F(\xi)$, by using Eqs. (3.5)-(3.10), (5.8)-(5.11) and (5.16)-(5.19) as follows

$$\tilde{u}_r = \gamma_1 [AI_1(\gamma_1 r) - BK_1(\gamma_1 r)] + \gamma_2 [CI_1(\gamma_2 r) - DK_1(\gamma_2 r)] + i\xi \gamma_3 [EI_1(\gamma_3 r) - FK_1(\gamma_3 r)] \quad (5.20)$$

$$\tilde{u}_z = i\xi [AI_0(\gamma_1 r) + BK_0(\gamma_1 r) + CI_0(\gamma_2 r) + DK_0(\gamma_2 r)] - \gamma_3^2 [EI_0(\gamma_3 r) + FK_0(\gamma_3 r)] \quad (5.21)$$

$$\tilde{w}_r = \gamma_1 \chi_1 [AI_1(\gamma_1 r) - BK_1(\gamma_1 r)] + \gamma_2 \chi_2 [CI_1(\gamma_2 r) - DK_1(\gamma_2 r)] + i\xi \gamma_3 \chi_3 [EI_1(\gamma_3 r) - FK_1(\gamma_3 r)] \quad (5.22)$$

$$\tilde{w}_z = i\xi \{ \chi_1 [AI_0(\gamma_1 r) + BK_0(\gamma_1 r)] + \chi_2 [CI_0(\gamma_2 r) + DK_0(\gamma_2 r)] \} - \gamma_3^2 \chi_3 [EI_0(\gamma_3 r) + FK_0(\gamma_3 r)] \quad (5.23)$$

$$\tilde{p} = \eta_1 [AI_0(\gamma_1 r) + BK_0(\gamma_1 r)] + \eta_2 [CI_0(\gamma_2 r) + DK_0(\gamma_2 r)] \quad (5.24)$$

$$\begin{aligned}
\tilde{\sigma}_{rr} = & \beta_1 [AI_0(\gamma_1 r) + BK_0(\gamma_1 r)] - 2\mu\gamma_1 r^{-1} [AI_1(\gamma_1 r) - BK_1(\gamma_1 r)] \\
& + \beta_2 [CI_0(\gamma_2 r) + DK_0(\gamma_2 r)] - 2\mu\gamma_2 r^{-1} [CI_1(\gamma_2 r) - DK_1(\gamma_2 r)] \\
& + i\xi\gamma_3^2 [EI_0(\gamma_3 r) + FK_0(\gamma_3 r)] - i\xi\gamma_3 r^{-1} [EI_1(\gamma_3 r) - FK_1(\gamma_3 r)]
\end{aligned} \tag{5.25}$$

$$\begin{aligned}
\tilde{\sigma}_{\theta\theta} = & -(\lambda L_1^2 + \alpha\eta_1) [AI_0(\gamma_1 r) + BK_0(\gamma_1 r)] + 2\mu\gamma_1 r^{-1} [AI_1(\gamma_1 r) - BK_1(\gamma_1 r)] \\
& -(\lambda L_2^2 + \alpha\eta_2) [CI_0(\gamma_2 r) + DK_0(\gamma_2 r)] + 2\mu\gamma_2 r^{-1} [CI_1(\gamma_2 r) - DK_1(\gamma_2 r)] \\
& + 2\mu i\xi\gamma_3 r^{-1} [EI_1(\gamma_3 r) - FK_1(\gamma_3 r)]
\end{aligned} \tag{5.26}$$

$$\begin{aligned}
\tilde{\sigma}_{zz} = & -(2\mu\xi^2 + \lambda L_1^2 + \alpha\eta_1) [AI_0(\gamma_1 r) + BK_0(\gamma_1 r)] - (2\mu\xi^2 + \lambda L_2^2 + \alpha\eta_2) [CI_0(\gamma_2 r) + DK_0(\gamma_2 r)] \\
& - 2\mu i\xi\gamma_3^2 [EI_0(\gamma_3 r) + FK_0(\gamma_3 r)]
\end{aligned} \tag{5.27}$$

$$\begin{aligned}
\tilde{\sigma}_{rz} = & 2\mu i\xi\gamma_1 [AI_1(\gamma_1 r) - BK_1(\gamma_1 r)] + 2\mu i\xi\gamma_2 [CI_1(\gamma_2 r) - DK_1(\gamma_2 r)] \\
& - \mu\gamma_3 (\xi^2 + \gamma_3^2) [EI_1(\gamma_3 r) - FK_1(\gamma_3 r)]
\end{aligned} \tag{5.28}$$

where η_i , β_i , L_i ($i=1, 2$) are given in Appendix C.

It can be shown that the general solutions for axisymmetric deformations of a poroelastic medium in the Fourier transform domain given by Eqs. (5.20)-(5.28) can be expressed in the following matrix form

$$\mathbf{u}(r, \xi) = \mathbf{R}(r, \xi)\mathbf{C}(\xi) \tag{5.29}$$

$$\mathbf{f}(r, \xi) = \mathbf{S}(r, \xi)\mathbf{C}(\xi) \tag{5.30}$$

where

$$\mathbf{u}(r, \xi) = [\tilde{u}_r \quad \tilde{u}_z \quad \tilde{p}]^T; \tag{5.31}$$

$$\mathbf{f}(r, \xi) = [\tilde{\sigma}_{rr} \quad \tilde{\sigma}_{rz} \quad \tilde{w}_r]^T \tag{5.32}$$

$$\text{and } \mathbf{C}(\xi) = [A \quad B \quad C \quad D \quad E \quad F]^T \tag{5.33}$$

The elements of matrices \mathbf{R} and \mathbf{S} in the above equations are given in Appendix C.

Similar to quasi-static problem presented in Chapter IV, the disturbed zone is discretized into infinitely long tubular layers with small thickness. The relationship between the generalized displacement vector $\mathbf{U}^{(n)}$ and the force vector $\mathbf{F}^{(n)}$ can be established for the n^{th} layer as

$$\mathbf{F}^{(n)} = \mathbf{K}^{(n)}\mathbf{U}^{(n)} \quad (5.34)$$

where $\mathbf{K}^{(n)}$ is an exact stiffness matrix of the n^{th} layer in the Fourier transform space. The elements of vectors $\mathbf{U}^{(n)}$ and $\mathbf{F}^{(n)}$ are defined similar to those in Eq. (4.21)-(4.22) respectively in the previous chapter with their elements being functions of r and ξ . In addition, the stiffness matrix for the undisturbed zone is given by Eq. (4.23). The elements of matrices $\mathbf{R}^{(N+1)}$ and $\mathbf{S}^{(N+1)}$ are given in Appendix C. The global stiffness matrix \mathbf{K}^* for this problem can be assembled by using the continuity conditions of traction and fluid flow at each interface, in which

$$\mathbf{F}^* = \mathbf{K}^*\mathbf{U}^* \quad (5.35)$$

where \mathbf{U}^* and \mathbf{F}^* are the global vectors of generalized displacements and generalized forces respectively. The elements of matrices \mathbf{U}^* and \mathbf{F}^* are given by Eqs. (4.25) and (4.26) respectively.

Consider a borehole in poroelastic medium with the EDZ subjected to radial traction $F_r(z)$, tangential traction $F_z(z)$, and either pore pressure $P(z)$ or fluid source $Q(z)$ applied at its surface. The boundary conditions can be expressed as

$$\tilde{\sigma}_{rr}(1, \xi) = \tilde{F}_r(\xi) - \alpha \tilde{p}(1, \xi) \quad (5.36)$$

$$\tilde{\sigma}_{rz}(1, \xi) = \tilde{F}_z(\xi) \quad (5.37)$$

$$\tilde{p}(1, \xi) = \tilde{P}(\xi) \quad \text{for fully permeable surface} \quad (5.38)$$

$$\text{or} \quad \tilde{q}_r(1, \xi) = \tilde{Q}(\xi) \quad \text{for impermeable surface} \quad (5.39)$$

5.3 Numerical Results and Discussion

Numerical results for dynamic response of an infinite borehole in a poroelastic medium by considering the excavation disturbed zone are presented in the section. In the first step, the system of liner simultaneous equations given by Eq. (4.24) is solved by using appropriate boundary and continuity conditions. Since Eq. (4.24) is established in the Fourier transform space, it has to be solved for discrete values of ξ . The solutions are then determined by using the numerical quadrature employing in Chapter IV to evaluate the semi-infinite integral scheme given by Eq. (4.2). The accuracy of the present solution scheme is verified by comparing with the existing solutions for a borehole in both elastic and poroelastic media. Parnes (1986) presented the dynamic response due to axisymmetric traction applied at

a cylindrical borehole surface. Fig. 5.1(a) shows comparisons of nondimensional radial displacement and tangential stress along the radial direction ($z/a=0$) due to a uniform line load (P) along a circle at $z/a=0$ of a borehole in an elastic medium. Poisson's ratio equal to 0.25 and a nondimensional frequency $\delta=2.0$, defined as $\delta = \omega a \sqrt{\rho_0 / \mu_0}$, are used where ρ_0 and μ_0 are mass density and shear modulus of the undisturbed zone respectively. Fig. 5.1(b) shows comparisons of vertical variations of the amplitudes of radial displacement, tangential and vertical stresses at $r/a=1.5$ due to a normal concentrated ring load with magnitude P applied at the level $z/a=0$ of the borehole wall. The present solutions are compared with those given by Lu and Jeng (2006). The following material parameters are used: $\lambda / \mu_0 = 0.333$; $M / \mu_0 = 0.667$; $\rho_f / \rho_0 = 0.488$; $\alpha = 0.95$; $m / \rho_0 = 2.333$; and $b^* = ab / \sqrt{\rho_0 \mu_0} = 577.40$. The diameter of the borehole is equal to $2a$ and its surface is assumed to be fully permeable. Two nondimensional frequencies of $\delta=5.73$ and 11.45 are presented. It is found that the comparisons in Figs. 5.1(a) and 5.1(b) show very close agreement between the present solutions and the existing solutions. Therefore, the accuracy of the present solution scheme is confirmed through these independent comparisons.

The numerical results are presented hereafter correspond to the cases where uniformly distributed radial traction of magnitude f_0 and uniform fluid pressure of magnitude p_0 applied over a finite segment of $h/a=1$ at the borehole surface (see Fig. 4.1). The following nondimensional parameters are considered for the surrounding poroelastic medium: $\lambda / \mu_0 = 0.333$; $M / \mu_0 = 0.667$; $\rho_f / \rho_0 = 0.5$; $\alpha = 0.95$ and $m / \rho_0 = 2.333$. The variation of shear modulus is assumed to be linearly varied with the radial direction given by Eq. (4.18). Two extreme cases of the hydraulic boundary conditions at the borehole surface i.e. fully permeable and impermeable, are considered.

Nondimensional radial displacement at the center of loading ($r/a=0, z/a=0$) are presented in Fig. 5.2 for various shear modulus profiles ($m_1=0, 0.1$ and 0.2) in the disturbed zone. Solutions are presented for the frequency range $0 < \delta \leq 10$. Numerical results in Fig. 5.2 indicate that the disturbed zone has a significant influence on the radial displacement. Radial variations of both real and imaginary parts of radial displacement with δ for the same value of m_1 are virtually similar for fully permeable and impermeable borehole walls. Both real and imaginary parts of the radial displacement for the undisturbed borehole ($m_1=0$) show more oscillatory variation with δ when compared to those being disturbed ($m_1 > 0$). The influence of internal friction between the solid and fluid phases (b) on the radial displacement is also

presented with $b^* = 1$ and 1000 in Fig. 5.2. The difference between the two solutions is less than 5% for both real and imaginary parts. It is also noted that the effect of b^* has little influence on the radial displacement regardless of the hydraulic boundary condition at borehole wall.

Tangential stress is useful in the study of borehole stability and fracturing. Nondimensional tangential stress with respect to the frequency of excitation is presented for both fully permeable and impermeable borehole walls in Figs. 5.3(a) and 5.3(b) respectively. For a fully permeable borehole wall, both real and imaginary parts of tangential stress show minor dependence on the internal friction as previously noted for the radial displacement in Fig. 5.2, whereas the internal friction has more influence for the impermeable borehole wall. Tangential stress decreases with increasing m_1 similarly to what observed for the radial displacement in Fig. 5.2 when $\delta < 2$. At higher frequencies ($\delta \geq 2$), real and imaginary parts of tangential stress show more complicated variations with m_1 .

Figure 5.4 presents nondimensional radial fluid discharge at the center of loading segment ($r/a = 1$ and $z/a = 0$) to investigate the flow rate at the borehole wall due to the radial traction applied on a fully permeable wall. As expected, both real and imaginary parts of fluid discharge are zero when $\delta = 0$. It is also found that radial discharge corresponding to $b^* = 1$ is larger than that of $b^* = 1000$ since b^* is inversely proportional to permeability. The effect of EDZ on the discharge at the borehole wall can be negligible for $b^* = 1000$ for the frequency range of $\delta < 10$.

Nondimensional excess pore pressure at the center of loading segment due to uniformly distributed load applied on an impermeable borehole wall is presented in Fig. 5.5. These results indicate that excess pore pressure depends very significantly on the internal friction b^* and m_1 . It can be seen that excess pore pressure corresponding to $b^* = 1$ shows more oscillation with δ when compared to that of $b^* = 1000$. This is similar to what observed from the fluid discharge results in Fig. 5.4. Excess pore pressure increases with increasing m_1 for the case of the internal friction $b^* = 1000$ whereas it shows complicated variation with $b^* = 1$.

Next, variations of nondimensional radial displacement, tangential stress, excess pore pressure, and fluid discharge in the radial direction ($z/a = 0$) due to uniform radial traction are illustrated in Figs. 5.6-5.7. Solutions are presented for $b^* = 1$ with $m_1 = 0, 0.1$ and 0.2 ; and $\delta = 0.5$ and 2.0 . It can be seen from the figures that both radial displacement and tangential

stress depend significantly on both m_1 and δ . The maximum values of both real and imaginary parts of radial displacement for $\delta=0.5$ occur at the borehole wall before decaying with the radial distance. For higher frequency ($\delta=2.0$), the displacement profiles show more oscillation, but the maximum value is still found at the borehole wall. The displacement decreases with increasing the value of m_1 near the borehole wall ($r/a < 3$), whereas it shows complicated variation away from the wall ($r/a > 3$). Radial profiles of nondimensional tangential stress in Fig. 5.6(b) show similar behavior to the displacement profiles in Fig 5.6(a). The maximum stresses are observed at the wall, and the stresses then decay along the radial distance. The tangential stress decreases with increasing m_1 . On the contrary, the profiles of tangential stress for $\delta=2$ show more oscillatory variation than those of the radial stress. It is implied from Fig. 5.6 that the imaginary parts of displacement and tangential stress become negligible when $\delta \rightarrow 0$ approaching their static counterparts.

Figs. 5.7(a) and 5.7(b) present variation of nondimensional excess pore pressure and fluid discharge respectively along the radial direction at the mid plane ($z/a=0$) for fully permeable borehole surface. Numerical results indicate that the excavation disturbed zone has a significant influence on both excess pore pressure and fluid discharge for $\delta=2.0$, whereas the solutions for the lower frequency ($\delta=0.5$) are independent of m_1 . Both real and imaginary parts of the solutions for $\delta=2.0$ show oscillatory variation along the radial direction. The peak values of fluid discharge are observed at the borehole surface, which are the same as the radial displacement and tangential stress presented in Fig 5.6. This is consistent with the fact that the maximum solutions should be at the point of applied loading. Excess pore pressure is equal to zero at the wall due to the specified boundary condition. In addition, both excess pore pressure and fluid discharge diminish to negligible level when $r/a \rightarrow \infty$.

The final set of numerical results corresponding to time-harmonic fluid pressure of magnitude P_0 applied over segment of length $h/a=1$ on an impermeable borehole wall. Figs. 5.8(a) and 5.8(b) show radial variations of nondimensional radial displacement and tangential stress respectively along the mid plane ($z/a=0$). It can be seen that profiles of radial displacement and tangential stress for $\delta=0.5$ are quite smooth along the radial direction, whereas the solutions for $\delta=2.0$ show more oscillatory variation with r/a before diminishing to zero when $r/a \rightarrow \infty$. Numerical results of radial displacement and tangential stress in Fig. 5.8 in the vicinity of the borehole wall present more fluctuation than those at a point away from the wall. It should be noted that the displacement and tangential stress due to the applied fluid pressure can be neglected when $r/a > 10$.

Figures 5.9(a) and 5.9(b) present profiles of nondimensional excess pore pressure and fluid discharge along the radial distance at $z/a=0$ due to time-harmonic fluid pressure applied at the borehole surface. It is found that both real and imaginary parts of the solutions have a smooth variation with r/a for the case of $\delta=0.5$ and they become oscillated for $\delta=2.0$ similar to the radial displacement and tangential stress demonstrated in Fig. 5.8. Both pore pressure and fluid discharge are maximal at the borehole surface and decrease along the radial distance before reaching zero value when $r/a>7$. The effect of excavation disturbed zone also shows significant influence on the excess pore pressure and fluid discharged. It is found that a solution with higher value of m_1 , shows more oscillatory variation than that with lower m_1 . This implies that higher gradient of shear modulus (more disturbed properties due to excavation) results in more fluctuations in the solution.

5.3 Conclusion

The analytical solutions for a cylindrical borehole in an excavation disturbed zone due to time-harmonic loading at the borehole wall are presented in this chapter. A set of general solutions to the equations of motion from Biot's poroelastodynamics theory is derived by using Helmholtz representation for axisymmetric vector fields and the Fourier integral transforms. The numerical results presented for dynamic response of the borehole with excavation disturbed zone show that it depends on many factors such as material properties, excavation damage, hydraulic boundary conditions along the borehole surface and the loading types. It is found that radial displacement, tangential stress, pore pressure and fluid discharge depend significantly on the change in shear modulus. The influence of internal friction due to relative motion between solid and fluid becomes less influence on radial displacement and tangential stress, but it has a significant influence on excess pore pressure and fluid discharge. The solutions along the radial direction show more fluctuations when the frequency excitation and the gradient of shear modulus increase. The solutions presented in this chapter are useful to study several problems related a cylindrical borehole in a poroelastic medium. For example, these solutions can be employed to study wave propagation problems corresponding to the empty and liquid-filled cylindrical borehole in fluid-saturated porous medium. In addition, the present analytical solutions can also be extended for stress analysis of a borehole under transient loading by employing an appropriate technique such as the fast Fourier transform.

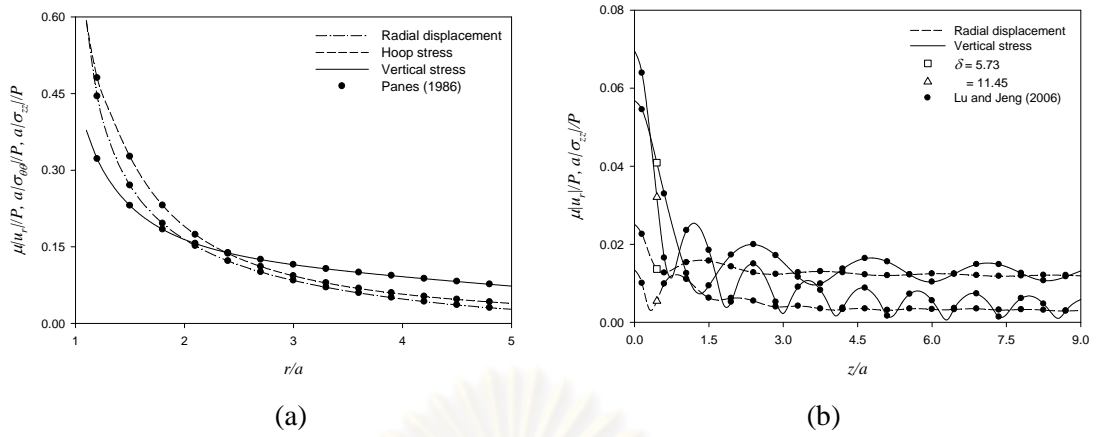


Figure 5.1 Comparison with existing solutions for a borehole in (a) elastic medium and (b) poroelastic medium.

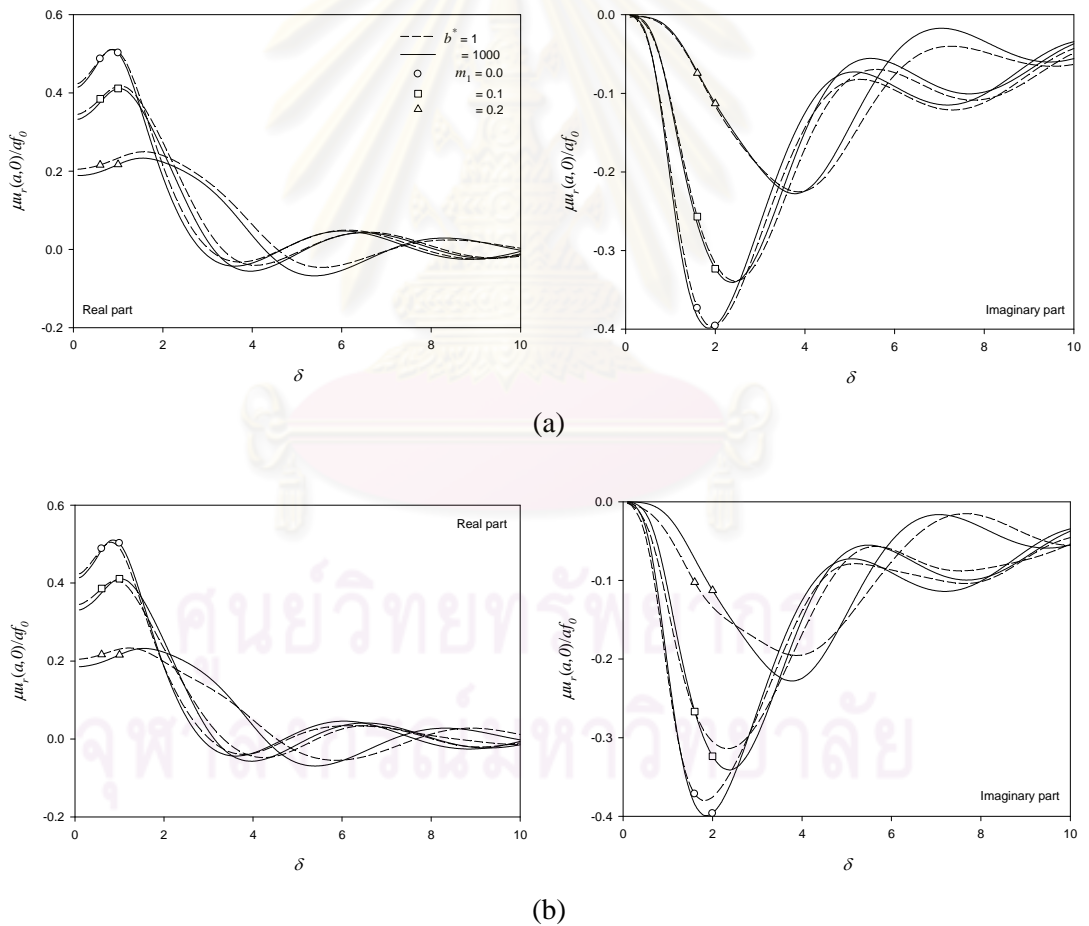
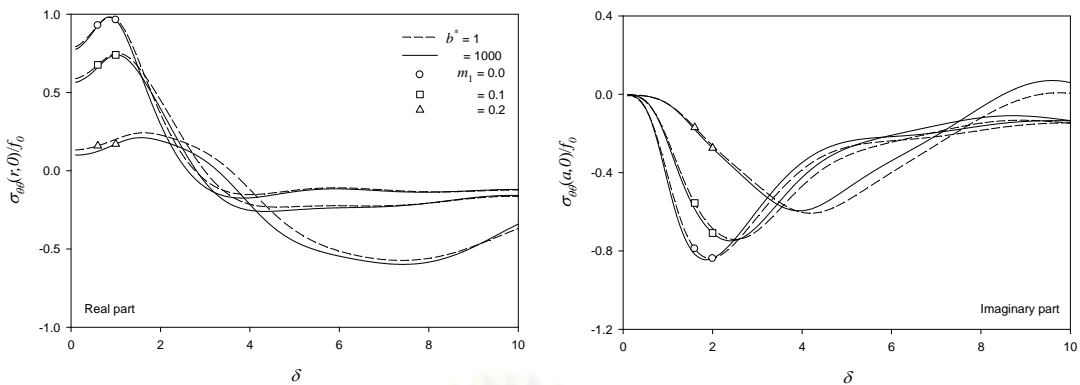
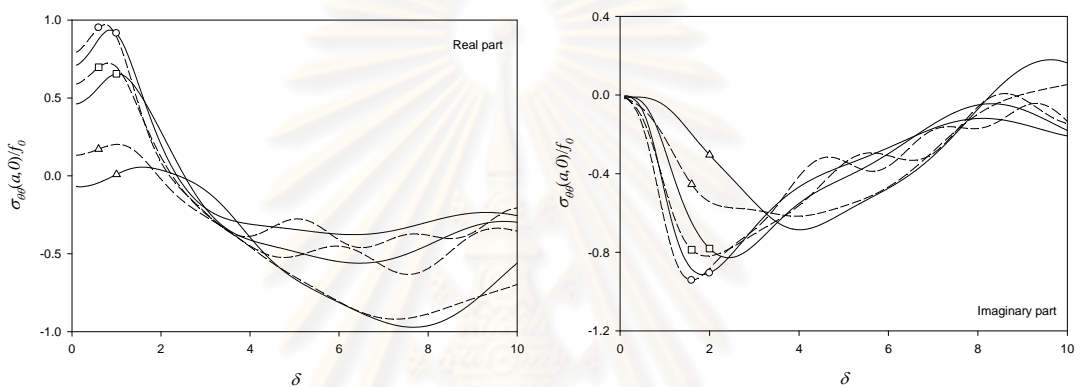


Figure 5.2 Radial displacement at the center of loading due to radial traction on (a) permeable wall and (b) impermeable wall.



(a)



(b)

Figure 5.3 Tangential stress at the center of loading due to radial traction on (a) permeable wall and (b) impermeable wall.

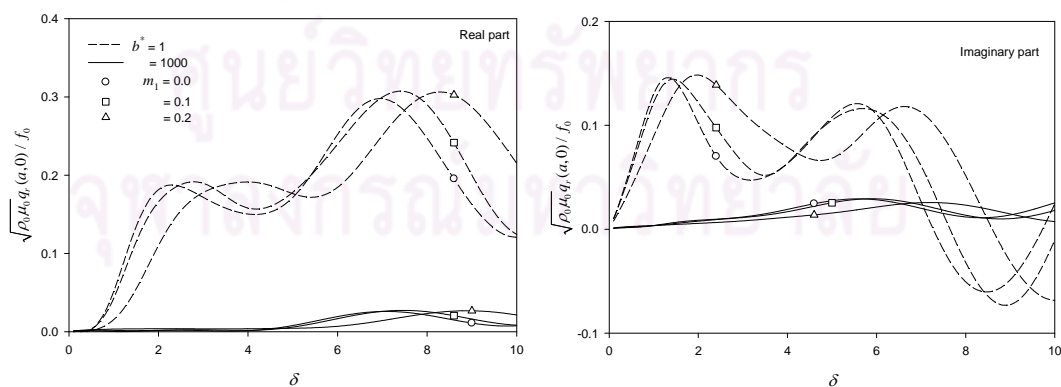


Figure 5.4 Radial discharge at the center of loading due to radial traction on permeable wall.

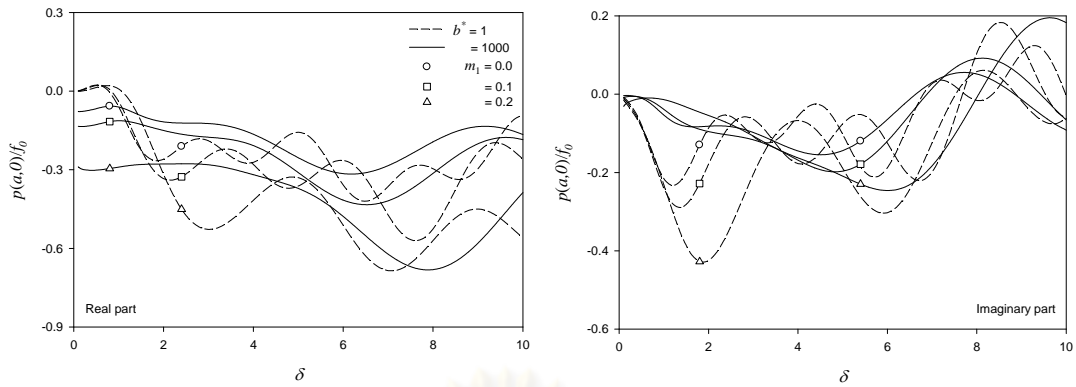
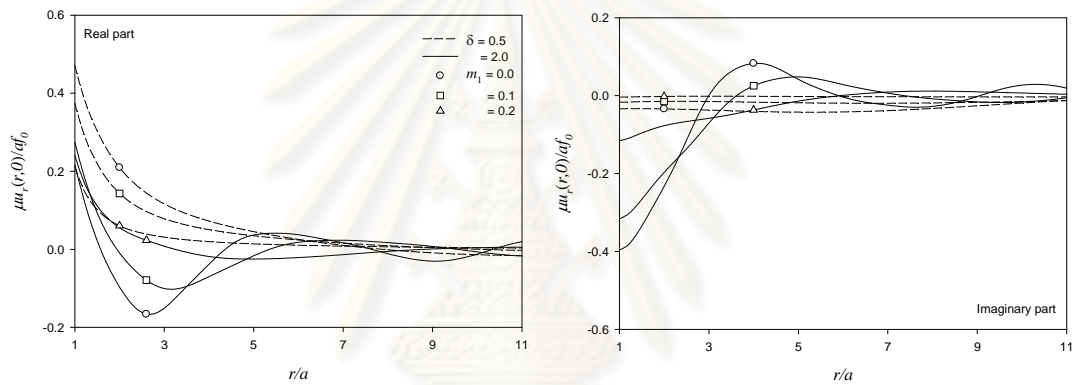
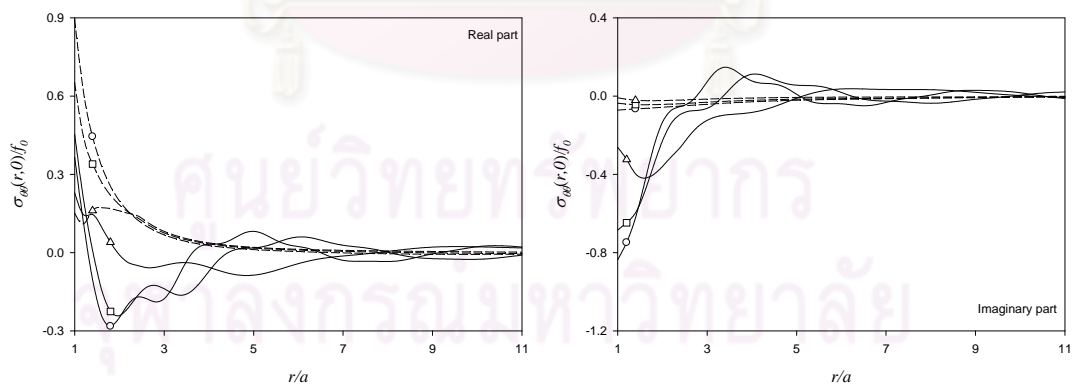


Figure 5.5 Excess pore pressure at the center of loading due to radial traction on impermeable wall.



(a)



(b)

Figure 5.6 Profiles of (a) radial displacement and (b) tangential stress along the r -axis due to radial traction on permeable wall.

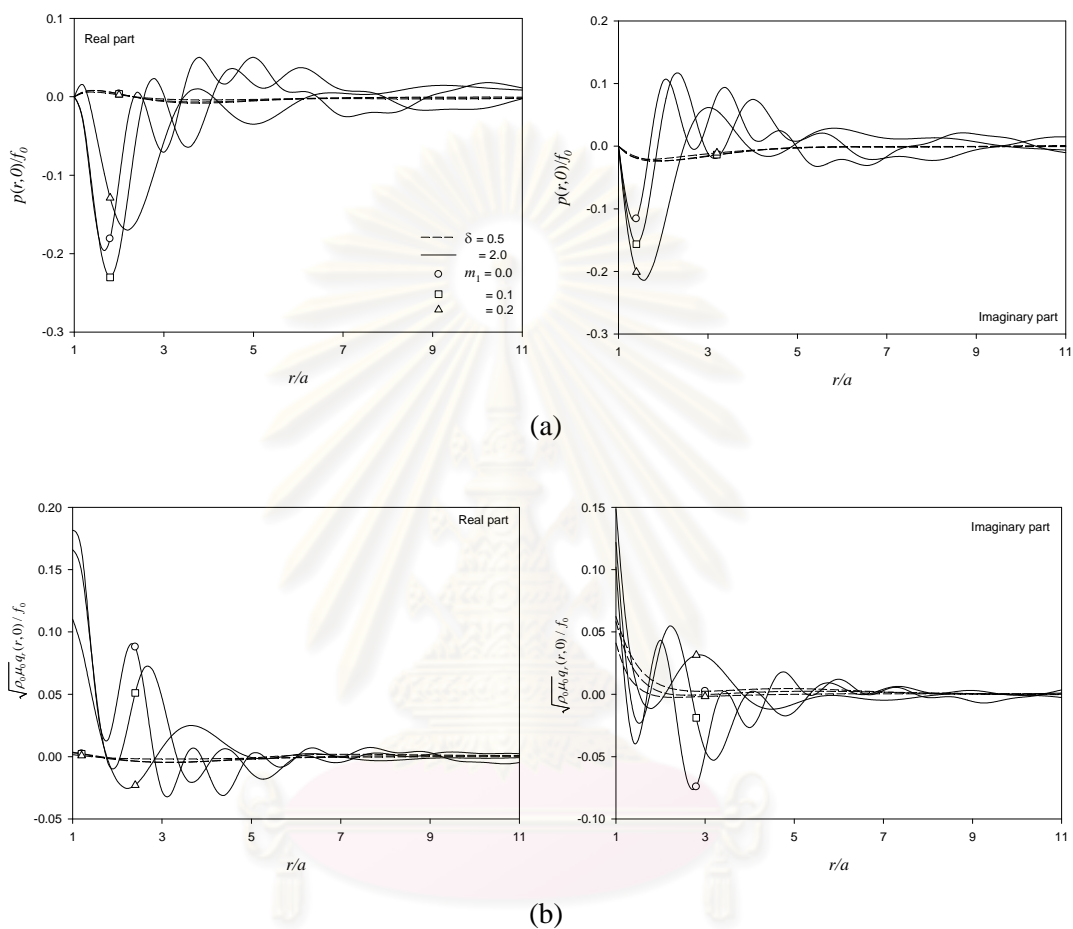


Figure 5.7 Profiles of (a) excess pore pressure and (b) radial discharge along the r -axis due to radial traction on permeable wall.

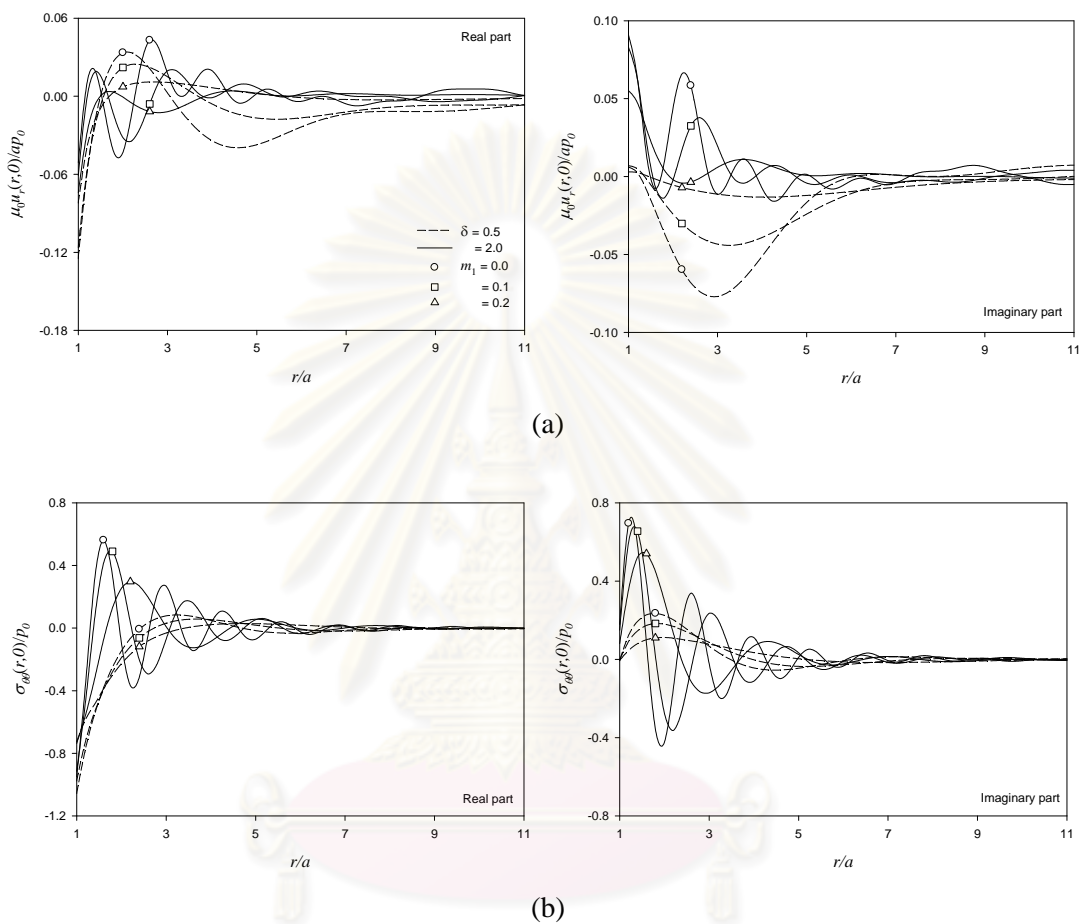


Figure 5.8 Profiles of (a) radial displacement and (b) tangential stress along the r -axis due to applied fluid pressure on permeable wall.

ศูนย์วิจัยทรัพยากรธรณี
จุฬาลงกรณ์มหาวิทยาลัย

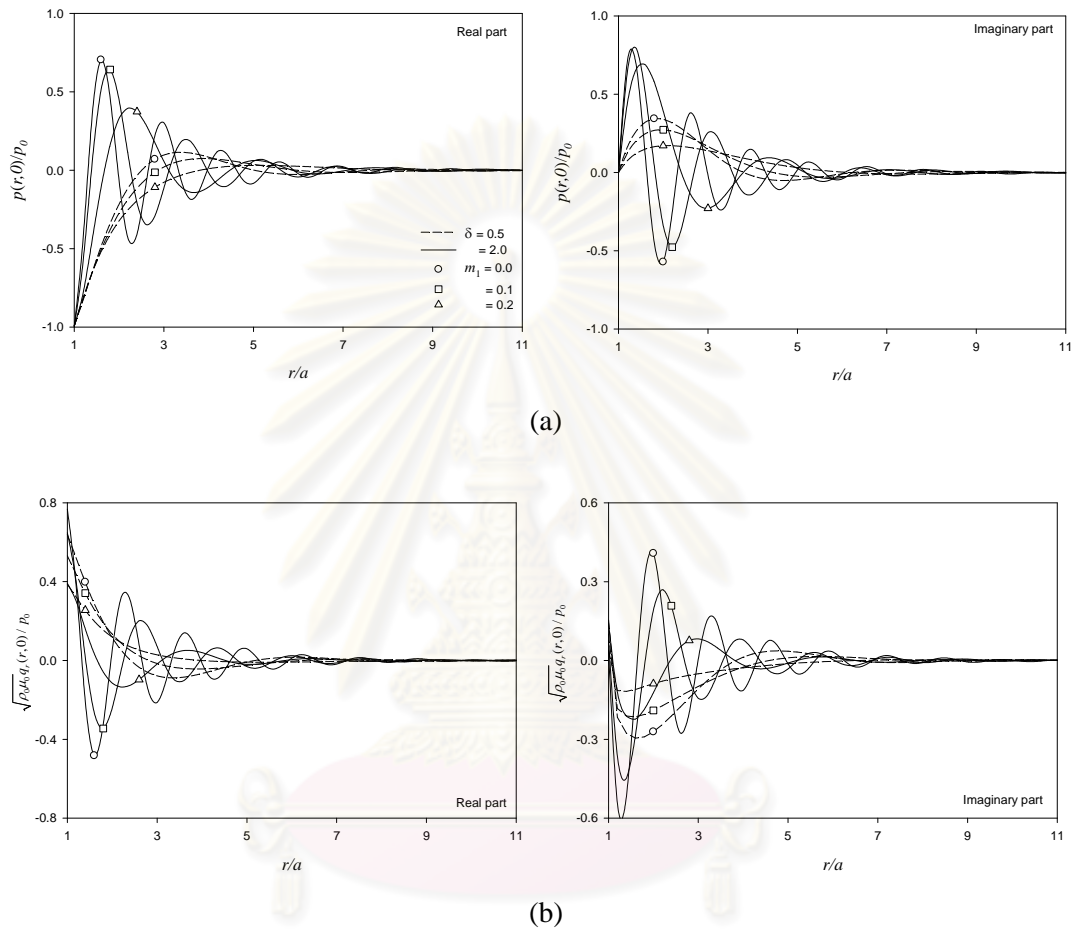


Figure 5.9 Profiles of (a) excess pore pressure and (b) radial discharge due to applied fluid pressure on permeable wall.

CHAPTER VI

CONCLUSIONS

This dissertation presents a theoretical study of poromechanical response of a finite cylinder and an infinite borehole under axisymmetric loading. Analytical solutions for a poroelastic cylinder, and a cylindrical borehole in a poroelastic medium with an excavation disturbed zone are presented. A set of general solutions is obtained from the governing equations based on Biot's theory of poroelasticity by applying appropriate integral transform techniques. There are three main problems presented in this study, i.e. quasi-static responses of a cylinder and a borehole, and dynamic response of a borehole. Separate conclusions are given at the end of Chapters III-V based on the results presented in those chapters. The major findings and conclusions of this study can be summarized as follows:

1. The analytical solutions are obtained in the appropriate transform spaces for each problem. The Laplace inversion is carried out by employing a numerical scheme presented by Stehfest (1970), whereas an adaptive numerical quadrature scheme using a 21-point Gauss-Kronrod rule is employed for the Fourier inversion. Accuracy of the present numerical schemes is confirmed by comparing with independent existing solutions for the limiting cases.
2. The present study considers the disturbed zone due to borehole drilling process that has never been taken into account in the past for stress analysis of borehole problems related to poroelastic materials. Shear modulus and permeability coefficient are assumed to be non-homogenous in the excavation disturbed zone in the present study. An exact stiffness matrix scheme has successfully been employed to solve the borehole problems.
3. Numerical results presented in this study indicate that poroelastic material properties and the hydraulic boundary conditions have a significant influence on poromechanical responses of cylinders and boreholes. It is also found that the solutions in the vicinity of borehole due to traction and fluid sources depend significantly on the reduced shear modulus in the disturbed zone. However, the increased permeability in the disturbed zone has a significant influence only on pore pressure and fluid discharge.

The analytical solutions presented in this study can be used to investigate a variety of problems in civil engineering applications involving cylinders and boreholes. Moreover, they can also be extended to study other practical problems, such as those related to hollow cylinders, load-diffusion from cylindrical piles, pressuremeter devices, hydraulic fracturing models, excavation and drilling, ground-water wells, and wave propagation problems etc.



ศูนย์วิทยทรัพยากร
จุฬาลงกรณ์มหาวิทยาลัย

REFERENCES

- Abousleiman, Y., and Chen S. (2010). Poromechanics response of an inclined borehole subject to in-situ stress and finite length fluid discharge, *J. Mech. Mater. Struct.*, 5(1), 47-66.
- Abousleiman, Y., Cheng, A.H.-D., Jiang, C., and Roegiers, J.-C. (1996). Poroviscoelastic analysis of borehole and cylinder problems, *Acta Mech.*, 119(1-4), 199-219.
- Abousleiman, Y., and Cui, L. (1998). Poroelastic solutions in transversely isotropic media for wellbore and cylinder, *Int. J. Solids Struct.*, 35(34-35), 4905-4929.
- Abousleiman, Y., et al. (1997). Applications of time-dependent pseudo-3D stress analysis in evaluation well bore stability, *Int. J. Rock Mech. Min.*, 34(3-4), paper no. 001.
- Bai, B., and Le T., (2009). Solutions for cylindrical cavity in saturated thermoporoelastic medium, *Acta Mech. Solida Sin.*, 22(1), 85-94.
- Biot, M.A. (1941). General theory of three-dimensional consolidation, *J. Appl. Phys.*, 12(2), 155-164.
- Biot, M.A. (1956). The theory of propagation of elastic waves in fluid-saturated porous solid. *J. Acous Aoc. Amer.*, 28(2), 168-191.
- Chau, K.T., and Wei, X.X. (2000). Finite solid circulars subjected to arbitrary surface load. Part I-Analytic solution, *Int. J. Solids Struct.*, 37(40), 5707-5732.
- Chau, K.T., and Wei, X.X., (2001). A new analytic solution for the diametral point load strength test on finite solid circular cylinders, *Int. J. Solids Struct.*, 38(9), 1459-1481.
- Cui, L., Cheng, A.H.-D., and Abousleiman, Y. (1997). Poroelastic solution for an inclined borehole, *J. Appl. Mech. ASME*, 64(1), 32-38.
- Cui, L., Ekbote, S., Abousleiman, Y., Zaman, M.M., and Roegier, J.-C. (1998). Borehole stability analyses in fluid saturated formations with impermeable walls, *Int. J. Rock Mech. Min.*, 35(4-5), 582-583.
- Cui L., and Abousleiman, Y. (2001). Time-dependent poromechanical responses of saturated cylinders, *J. Eng. Mech. ASCE*, 127(4), 391-398.
- Cui L., Abousleiman Y., Cheng A.H.-D., and Roegiers J.-C. (1999). Time-dependent failure analysis of inclined boreholes in fluid saturated formations, *J Energy Resour Technol.*, 121(1), 31-38.
- Detournay, E., and Cheng, A.H.-D. (1988). Poroelastic response of a borehole in non-hydrostatic stress field, *Int. J. Rock Mech. Min.*, 25(3), 171-182.
- Ekbote, S., Abousleiman, Y., Cui, L., and Zaman, M. (2004). Analysis of inclined boreholes in poroelastic media, *Int. J. Geomech ASCE*, 4(1), 178-190.

- Jourine, S., Valko, P.P., and Kronenberg, A.K. (2004). Modelling poroelastic hollow cylinder experiments with realistic boundary conditions, *Int. J. Numer. Anal. Mech. Geomech.*, 28(12), 1189-1205.
- Jordan, D.W. (1962). The stress wave from a finite cylindrical explosive source, *J. Math. Mech.*, 11(4), 503-551.
- Kanj, M., Abousleiman, Y., and Ghanem, R. (2003). Poromechanics of anisotropic hollow cylinders, *J. Eng. Mech. ASCE*, 129(12), 1277-1287.
- Kwon, S., Lee, C.S., Cho, S.J., Jeon, S.W., and Cho, W.J. (2009). An investigation of the excavation damaged zone at the KAERI underground research tunnel, *Tunn Undergr. Sp. Tech.* 24(1), 1-13.
- Lai, X., Cai, M., Ren, F., Xie, M., and Esaki, T. (2006). Assessment of rock mass characteristics and the excavation disturbed zone in the Lingxin Coal Mine beneath and Xitian river, China, *Int. J. Rock Mech. Min.* 43,572-581.
- Lu, J.F., and Jeng, D.S. (2006). Dynamic analysis of a finite cylindrical hole in a saturated poroelastic medium, *Arch Appl. Mech.*, 76(5), 263-276.
- Lekhnitskii, S. G. (1963). *Theory of elasticity of an anisotropic elastic body*, English translation by P. Fern, Holden-Day Inc., San Francisco.
- Malmgren, L., Saiang, D., Töyrä, J., and Bodare, A. (2007). The excavation disturbed zone (EDZ) at Kiirunavaara mine, *J. Appl. Geophys.*, 61(1), 1-15.
- Martino, J.B., and Chandler, N.A. (2004). Excavation-induced damage studies at the Underground Research Laboratory, *Int. J. Rock Mech. Min.* 41(8), 1413-1426.
- Parnes, R. (1982). Applied tractions on the surface of an infinite cylindrical bore, *Int. J. Solids Struct.*, 19(2), 165-177.
- Parnes, R. (1983). Elastic response to a time-harmonic torsion-force acting on a bore surface, *Int. J. Solids Struct.*, 19(10), 925-934.
- Parnes, R. (1986). Steady-state ring load pressure on a borehole surface, *Int. J. Solids Struct.*, 22(1), 73-86.
- Piessens, R. (1975). Bibliography on numerical inversion of the Laplace transform and applications. *J. Comp. Appl. Math.*, 1, 115-126.
- Rajapakse, R.K.N.D. (1993). Stress analysis of borehole in poroelastic medium, *J. Eng. Mech.*, ASCE, 119(6), 1205-1227.
- Rajapakse, R.K.N.D., and Gross, D. (1996). Traction and contact problems for an anisotropic medium with a cylindrical borehole, *Int. J. Solids Struct.*, 33(15), 2193-2211.
- Rajapakse R.K.N.D., and Senjuntichai, T. (1993). Fundamental solutions for a poroelastic half-space with compressive constituents. *J. App. Mech.*, ASME, 60(4), 847-856.

- Robison, N.I. (2002). An isotropic elastic medium containing a cylindrical borehole with a rigid plug, *Int. J. Solids Struct.*, 39(19), 4889-4904.
- Rice, J. R., and Cleary, M. P. (1976). Some basic stress-diffusion solutions for fluid saturated elastic porous media with compressible constituents, *Rev. Geophys. Space Phys.*, 14(2), 227-241.
- Sato, T., Kikuchi, T., and Sugihara, K. (2000). In-situ experiments on an excavation disturbed zone induced by mechanical excavation in Neogene sedimentary rock at Tono mine, central Japan, *Eng. Geol.*, 56, 97-108.
- Shao, H., Schuster, K., Sonnke, J., and Brauer, V. (2008). EDZ development in indurated clay formations-In situ borehole measurements and coupled HM modeling. *Phys. Chem. Earth*. 33(1), S388-S395.
- Senjuntichai, T., and Sapsathiarn, Y. (2006). Time-dependent response of circular plate in multi-layered poroelastic medium. *Comput. Geotech.*, 33(3), 155-166.
- Skempton, A. W. (1954). The pore pressure coefficients A and B. *Geotechnique*, 4, 143-147.
- Sneddon, I. N. (1951). *Fourier Transforms*. McGraw-Hill, New York.
- Stehfest, H. (1970). Numerical inversion of Laplace transforms, *Commun. Ass. Comput. Mach.*, 13(1), 47-49.
- Terzaghi K. (1923). Die berechnung der durchlassigkeitsziffer des tones aus dem verlauf der hydrodynamischen spannungserscheinunge, *Sitz. Acad. Wissen., Wien Math. Naturwiss. Kl., Abt. IIa*, 132(3-4), 105-124.
- Vendhan, C.P., and Archer, R.R. (1978). Axisymmetric stresses in transversely isotropic finite cylinder. *Int. J. Solids Struct.*, 14(4), 305-318.
- Watanabe, S. (1996). Elastic analysis of axi-symmetric finite cylinder constrained radial displacement on the loading end, *Struct. Engrg./Earthquake Engrg.*, 13(2), 175s-185s.
- Watson, G. N. (1962). *A treatise on the theory of Bessel functions*. 2nd Ed., Cambridge University Press, Cambridge, England.
- Wei, X. X., and Chau, K. T. (2002). Analytic solution for finite transversely isotropic circular cylinders under the axial point load test, *J. Eng. Mech. ASCE*, 128(2), 209-219.
- Wei, X. X., and Chau, K. T. (2000). "Finite solid circular cylinder subjected arbitrary surface load. Part II: Application to double-punch test." *Int. J. Solids Struct.*, 37(40), 5733-5744.
- Wei, X. X., Chau, K. T., and Wong, R. H. C., (1999). Exact analytic solution for axial point load strength test for solid circular cylinders, *J. Eng. Mech. ASCE*, 125(12), 1349-1357.



APPENDICES

ศูนย์วิทยทรัพยากร
จุฬาลงกรณ์มหาวิทยาลัย

Appendix A

The expression of $\bar{\sigma}_{ij0}$, $\bar{\sigma}_{ijm}$, $\bar{\sigma}_{ijn}$, \bar{p}_0 , \bar{p}_m , \bar{p}_n , \bar{q}_{i0} , \bar{q}_{im} and \bar{q}_{in} ($i, j = r, \theta, z$) in Eqs. (3.26)-(3.32) are given by

$$\bar{\sigma}_{r0}(r, z, s) = -\eta A_0 \cosh(\sqrt{s}z) - \eta s^{-1/2} r^{-1} B_0 I_1(\sqrt{s}r) + a_3 C_0 + a_1 D_0 \quad (\text{A.1})$$

$$\begin{aligned} \bar{\sigma}_{rm}^{(1)}(z, s) &= -\eta \gamma_m^2 s^{-1} A_m \cosh(\gamma_m z) + [a_2 \cosh(\lambda_m z) + a_1 \lambda_m z \sinh(\lambda_m z)] C_m \\ &\quad - \lambda_m E_m \cosh(\lambda_m z) \end{aligned} \quad (\text{A.2})$$

$$\begin{aligned} \bar{\sigma}_{rm}^{(2)}(z, s) &= \eta \lambda_m s^{-1} A_m \cosh(\gamma_m z) - [\lambda_m^{-1} \cosh(\lambda_m z) + a_1 z \sinh(\lambda_m z)] C_m \\ &\quad + E_m \cosh(\lambda_m z) \end{aligned} \quad (\text{A.3})$$

$$\begin{aligned} \bar{\sigma}_{rm}(r, s) &= \eta s^{-1} [\xi_n^2 I_0(\beta_n r) - \beta_n r^{-1} I_1(\beta_n r)] B_n - [\xi_n I_0(\xi_n r) - r^{-1} I_1(\xi_n r)] F_n \\ &\quad + \left\{ (a_1 + a_2) I_0(\xi_n r) - [a_1 \xi_n r + 2a_2 \xi_n^{-1} r^{-1}] I_1(\xi_n r) \right\} D_n \end{aligned} \quad (\text{A.4})$$

$$\bar{\sigma}_{z0}(r, z, s) = -\eta B_0 I_0(\sqrt{s}r) + a_2 C_0 + a_3 D_0 \quad (\text{A.5})$$

$$\begin{aligned} \bar{\sigma}_{zm}(z, s) &= \eta \lambda_m^2 s^{-1} A_m \cosh(\gamma_m z) + [a_3 \cosh(\lambda_m z) - a_1 \lambda_m z \sinh(\lambda_m z)] C_m \\ &\quad + \lambda_m E_m \cosh(\lambda_m z) \end{aligned} \quad (\text{A.6})$$

$$\bar{\sigma}_{zn}(r, s) = -\eta \beta_n^2 s^{-1} B_n I_0(\beta_n r) + [a_3 I_0(\xi_n r) + a_1 \xi_n r I_1(\xi_n r)] D_n + \xi_n G_n I_0(\xi_n r) \quad (\text{A.7})$$

$$\bar{\sigma}_{\theta\theta 0}(r, z, s) = -\eta A_0 \cosh(\sqrt{s}z) - \eta B_0 [I_0(\sqrt{s}r) + s^{-1/2} r^{-1} I_1(\sqrt{s}r)] + a_3 C_0 + a_1 D_0 \quad (\text{A.8})$$

$$\bar{\sigma}_{\theta\theta m}^{(1)}(z, s) = -\eta A_m \cosh(\gamma_m z) + a_3 C_m \cosh(\lambda_m z) \quad (\text{A.9})$$

$$\begin{aligned} \bar{\sigma}_{\theta\theta m}^{(2)}(z, s) &= -\eta \lambda_m s^{-1} A_m \cosh(\gamma_m z) + [\lambda_m^{-1} \cosh(\lambda_m z) + a_1 z \sinh(\lambda_m z)] C_m \\ &\quad - E_m \cosh(\lambda_m z) \end{aligned} \quad (\text{A.10})$$

$$\begin{aligned} \bar{\sigma}_{\theta\theta n}(r, s) &= -\eta [I_0(\beta_n r) - \beta_n s^{-1} r^{-1} I_1(\beta_n r)] B_n - [I_0(\xi_n r) / 2 - 2a_2 \xi_n^{-1} r^{-1} I_1(\xi_n r)] D_n \\ &\quad - r^{-1} F_n I_1(\xi_n r) \end{aligned} \quad (\text{A.11})$$

$$\begin{aligned}\bar{\sigma}_{rz}(z, s) &= -\eta\gamma_m\lambda_m s^{-1}A_m \sinh(\gamma_m z) + [\sinh(\lambda_m z) / 2 + a_1\lambda_m z \cosh(\lambda_m z)]C_m \\ &\quad - \lambda_m E_m \sinh(\lambda_m z)\end{aligned}\quad (\text{A.12})$$

$$\bar{\sigma}_{rz}(r, s) = -\eta\xi_n\beta_n s^{-1}B_n I_1(\beta_n r) + [a_1\xi_n r I_0(\xi_n r) - a_2 I_1(\xi_n r)]D_n + \xi_n G_n I_1(\xi_n r) \quad (\text{A.13})$$

$$\bar{p}_0(r, z, s) = a_4\eta[A_0 \cosh(\sqrt{s}z) + B_0 I_0(\sqrt{s}r) +] - a_2\eta[C_0 + D_0] \quad (\text{A.14})$$

$$\bar{p}_m(z, s) = \eta[a_4 A_m \cosh(\gamma_m z) - a_2 C_m \cosh(\lambda_m z)] \quad (\text{A.15})$$

$$\bar{p}_n(r, s) = a_4\eta B_n I_0(\beta_n r) - a_2\eta D_n I_0(\xi_n r) \quad (\text{A.16})$$

$$\bar{q}_{r0}(r, z, s) = -\kappa a_4\eta\sqrt{s}B_0 I_1(\sqrt{s}r) \quad (\text{A.17})$$

$$\bar{q}_{rm}(z, s) = \kappa\eta[a_4 A_m \cosh(\gamma_m z) - a_2 C_m \cosh(\lambda_m z)] \quad (\text{A.18})$$

$$\bar{q}_{rn}(r, s) = -\kappa[a_4\eta\beta_n B_n I_1(\beta_n r) - a_2\eta\xi_n D_n I_1(\xi_n r)] \quad (\text{A.19})$$

$$\bar{q}_{z0}(r, z, s) = -\kappa a_4\eta\sqrt{s}A_0 \sinh(\sqrt{s}z) \quad (\text{A.20})$$

$$\bar{q}_{zm}(z, s) = -\kappa\eta[a_4\gamma_m A_m \sinh(\gamma_m z) - a_2\lambda_m C_m \sinh(\lambda_m z)] \quad (\text{A.21})$$

$$\bar{q}_{zn}(r, s) = \kappa\xi_n[a_4\eta B_n I_0(\beta_n r) - a_2\eta D_n I_0(\xi_n r)] \quad (\text{A.22})$$

where

$$a_3 = \frac{\nu_u}{(1 - 2\nu_u)} \quad (\text{A.23})$$

$$a_4 = \frac{B(1-\nu)(1+\nu_u)}{3(\nu_u - \nu)} \quad (\text{A.24})$$

Appendix B

The elements of $\mathbf{R}(r, \xi, s)$ and $\mathbf{S}(r, \xi, s)$ matrices as shown in Eqs. (4.13) and (4.14) respectively are given by

$$\mathbf{R} = \begin{bmatrix} R_{11} & R_{12} & R_{13} & R_{14} & R_{15} & R_{16} \\ R_{21} & R_{22} & R_{23} & R_{24} & R_{25} & R_{26} \\ R_{31} & R_{32} & R_{33} & R_{34} & R_{35} & R_{36} \end{bmatrix} \quad (\text{B.1})$$

$$\mathbf{S} = \begin{bmatrix} S_{11} & S_{12} & S_{13} & S_{14} & S_{15} & S_{16} \\ S_{21} & S_{22} & S_{23} & S_{24} & S_{25} & S_{26} \\ S_{31} & S_{32} & S_{33} & S_{34} & S_{35} & S_{36} \end{bmatrix} \quad (\text{B.2})$$

where

$$\begin{aligned} R_{11} &= \eta\beta s^{-1} I_1(\beta r) & R_{12} &= -\eta\beta s^{-1} K_1(\eta r) \\ R_{13} &= 2(1-2\nu_u) I_1(|\xi| r) - |\xi| r I_2(|\xi| r) & R_{14} &= -2(1-2\nu_u) K_1(|\xi| r) - |\xi| r K_2(|\xi| r) \\ R_{15} &= -i\xi I_1(|\xi| r) & R_{16} &= i\xi K_1(|\xi| r) \\ R_{21} &= i\xi \eta s^{-1} I_0(\beta r) & R_{22} &= i\xi \eta s^{-1} K_0(\beta r) \\ R_{23} &= -i\xi r I_1(|\xi| r) & R_{24} &= i\xi r K_1(|\xi| r) \\ R_{25} &= |\xi| I_0(|\xi| r) & R_{26} &= |\xi| K_0(|\xi| r) \\ R_{31} &= \frac{B^2(1+\nu_u)^2(1-\nu)}{9(1-\nu_u)(\nu_u-\nu)} I_0(\beta r) & R_{32} &= \frac{B^2(1+\nu_u)^2(1-\nu)}{9(1-\nu_u)(\nu_u-\nu)} K_0(\beta r) \\ R_{33} &= -\frac{2B|\xi|(1+\nu_u)}{3} I_0(|\xi| r) & R_{34} &= -\frac{2B|\xi|(1+\nu_u)}{3} K_0(|\xi| r) \\ R_{35} &= 0 & R_{36} &= 0 \\ S_{11} &= \eta s^{-1} [\xi^2 I_0(\beta r) - \beta r^{-1} I_1(\beta r)] & S_{12} &= \eta s^{-1} [\xi^2 K_0(\beta r) + \beta r^{-1} K_1(\beta r)] \\ S_{13} &= 2(1-\nu_u) |\xi| I_0(|\xi| r) - 2(1-2\nu_u) r^{-1} I_1(|\xi| r) + |\xi| I_2(|\xi| r) - \xi^2 r I_1(|\xi| r) \end{aligned}$$

$$\begin{aligned}
S_{14} &= 2(1-\nu_u)|\xi|K_0(|\xi|r) + 2(1-2\nu_u)r^{-1}K_1(|\xi|r) + |\xi|K_2(|\xi|r) + \xi^2 r K_1(|\xi|r) \\
S_{15} &= -i\xi \left[|\xi|I_0(|\xi|r) - r^{-1}I_1(|\xi|r) \right] & S_{16} &= -i\xi \left[|\xi|K_0(|\xi|r) + r^{-1}K_1(|\xi|r) \right] \\
S_{21} &= i\xi\eta\beta s^{-1}I_1(\beta r) & S_{22} &= -i\xi\eta\beta s^{-1}K_1(\beta r) \\
S_{23} &= -i\xi \left[2\nu_u I_1(|\xi|r) + |\xi|rI_2(|\xi|r) \right] & S_{24} &= i\xi \left[2\nu_u K_1(|\xi|r) - |\xi|rK_2(|\xi|r) \right] \\
S_{25} &= \xi^2 I_1(|\xi|r) & S_{26} &= -\xi^2 K_1(|\xi|r) \\
S_{31} &= \frac{B^2 s \beta (1+\nu_u)^2 (1-\nu)}{9(1-\nu_u)(\nu_u-\nu)} I_1(\beta r) & S_{32} &= -\frac{B^2 s \beta (1+\nu_u)^2 (1-\nu)}{9(1-\nu_u)(\nu_u-\nu)} K_1(\beta r) \\
S_{33} &= -\frac{2Bs\xi^2(1+\nu_u)}{3} I_1(|\xi|r) & S_{34} &= \frac{2Bs\xi^2(1+\nu_u)}{3} K_1(|\xi|r) \\
S_{35} &= 0 & S_{36} &= 0
\end{aligned}$$

In addition, the elements of $\mathbf{R}^{(N+1)}(r, \xi, s)$ and $\mathbf{S}^{(N+1)}(r, \xi, s)$ matrices as shown in Eq. (4.23) for latest layer given by

$$\mathbf{R}^{(N+1)} = \begin{bmatrix} R_{12} & R_{14} & R_{16} \\ R_{22} & R_{24} & R_{26} \\ R_{32} & R_{34} & R_{36} \end{bmatrix} \quad (\text{B.3})$$

$$\mathbf{S}^{(N+1)} = \begin{bmatrix} S_{12} & S_{14} & S_{16} \\ S_{22} & S_{24} & S_{26} \\ S_{32} & S_{34} & S_{36} \end{bmatrix} \quad (\text{B.4})$$

Appendix C

The matrices **R** and **S** in Eqs. (4.13) and (4.14) corresponding to dynamic response of a borehole problem in Chapter V are given by

$$\mathbf{R} = \begin{bmatrix} \gamma_1 I_1(\gamma_1 r) & -\gamma_1 K_1(\gamma_1 r) & \gamma_2 I_1(\gamma_2 r) & -\gamma_2 K_1(\gamma_2 r) & i\xi \gamma_3 I_1(\gamma_3 r) & -i\xi \gamma_3 K_1(\gamma_3 r) \\ i\xi I_0(\gamma_1 r) & i\xi K_0(\gamma_1 r) & i\xi I_0(\gamma_2 r) & i\xi K_0(\gamma_2 r) & -\gamma_3^2 I_0(\gamma_3 r) & -\gamma_3^2 K_0(\gamma_3 r) \\ \eta_1 I_0(\gamma_1 r) & \eta_1 K_0(\gamma_1 r) & \eta_2 I_0(\gamma_2 r) & \eta_2 K_0(\gamma_2 r) & 0 & 0 \end{bmatrix} \quad (\text{C.1})$$

$$\mathbf{S} = \begin{bmatrix} \beta_1 I_0(\gamma_1 r) - 2\mu\gamma_1 r^{-1} I_1(\gamma_1 r) & \beta_1 K_0(\gamma_1 r) - 2\mu\gamma_1 r^{-1} K_1(\gamma_1 r) & \beta_2 I_0(\gamma_2 r) - 2\mu\gamma_2 r^{-1} I_1(\gamma_2 r) & \\ 2\mu i \xi \gamma_1 I_1(\gamma_1 r) & -2\mu i \xi \gamma_1 K_1(\gamma_1 r) & 2\mu i \xi \gamma_2 I_1(\gamma_2 r) & \\ \gamma_1 \chi_1 I_1(\gamma_1 r) & -\gamma_1 \chi_1 K_1(\gamma_1 r) & \gamma_2 \chi_2 I_1(\gamma_2 r) & \\ \beta_2 K_0(\gamma_2 r) - 2\mu\gamma_2 r^{-1} K_1(\gamma_2 r) & i\xi \gamma_3 [\gamma_3 I_0(\gamma_3 r) - r^{-1} I_1(\gamma_3 r)] & i\xi \gamma_3 [\gamma_3 K_0(\gamma_3 r) - r^{-1} K_1(\gamma_3 r)] & \\ -2\mu i \xi \gamma_2 K_1(\gamma_1 r) & -\mu\gamma_3 (\xi^2 + \gamma_3^2) I_1(\gamma_3 r) & \mu\gamma_3 (\xi^2 + \gamma_3^2) K_1(\gamma_3 r) & \\ -\gamma_2 \chi_2 K_1(\gamma_2 r) & i\xi \gamma_3 \chi_3 I_1(\gamma_3 r) & -i\xi \gamma_3 \chi_3 K_1(\gamma_3 r) & \end{bmatrix} \quad (\text{C.2})$$

where

$$\begin{aligned} \eta_i &= (\alpha + \chi_i) M L_i^2, \quad i=1, 2; & \beta_i &= 2\mu\gamma_i^2 - \lambda L_i^2 - \alpha\eta_i, \quad i=1, 2; \\ \chi_i &= \frac{(\lambda + \alpha^2 M + 2\mu)L_i^2 - \rho\omega^2}{\rho_f \omega^2 - \alpha M L_i^2}, \quad i=1, 2; & \chi_3 &= \frac{\rho_f \omega^2}{ib\omega - m\omega^2} \\ \gamma_i &= \sqrt{\xi^2 - L_i^2}, \quad i=1, 2 & \gamma_3 &= \sqrt{\xi^2 - S^2} \\ L_1^2 &= \frac{\varpi_1 + \sqrt{\varpi_1^2 - 4\varpi_2}}{2} & L_2^2 &= \frac{\varpi_1 - \sqrt{\varpi_1^2 - 4\varpi_2}}{2} \\ S^2 &= \frac{(\rho_f \chi_3 + \rho)\omega^2}{\mu} \\ \varpi_1 &= \frac{(m\omega^2 - ib\omega)(\lambda + \alpha^2 M + 2\mu) + \rho\omega^2 M - 2\alpha\rho_f \omega^2 M}{(\lambda + 2\mu)M} \\ \varpi_2 &= \frac{(m\omega^2 - ib\omega)\rho\omega^2 - \rho_f^2 \omega^4}{M(\lambda + 2\mu)} \end{aligned}$$

In addition, the elements of $\mathbf{R}^{(N+1)}(r, \xi, s)$ and $\mathbf{S}^{(N+1)}(r, \xi, s)$ matrices for latest layer are given by

$$\mathbf{R}^{(N+1)} = \begin{bmatrix} R_{12} & R_{14} & R_{16} \\ R_{22} & R_{24} & R_{26} \\ R_{32} & R_{34} & R_{36} \end{bmatrix} \quad (\text{C.3})$$

$$\mathbf{S}^{(N+1)} = \begin{bmatrix} S_{12} & S_{14} & S_{16} \\ S_{22} & S_{24} & S_{26} \\ S_{32} & S_{34} & S_{36} \end{bmatrix} \quad (\text{C.4})$$



ศูนย์วิทยทรัพยากร
จุฬาลงกรณ์มหาวิทยาลัย

BIOGRAPHY

The author, Wichairat Kaewjuea, was born in Krabi, Thailand, on November 22, 1978. He received his Bachelor of Engineering degree in Civil Engineering from Prince of Songkla University on April 4, 2000. He continued his Master degree study at Chulalongkorn University in the same year under the supervision of Professor Dr. Teerapong Senjuntichai and successfully fulfilled the requirements for the M.Eng. degree on June 3, 2004. He was employed as a design engineer at Italian-Thai Development Public Company Limited until April of 2005 and then enrolled in Chulalongkorn University to pursue a Doctor of Philosophy degree in Civil Engineering, again with Professor Dr. Teerapong Senjuntichai, in May 2005 under the CHE and AUN/SEED-Net Fund. He visited the University of British Columbia, Vancouver, Canada, to conduct a research work with Professor Dr. Nimal Rajapakse in April 2008 – July 2009.



ศูนย์วิทยทรัพยากร
จุฬาลงกรณ์มหาวิทยาลัย